Master of Science Thesis

Streak control within a turbulent boundary layer using streamwise arrays of plasma actuators

Marcel Hennevelt

July 2, 2012

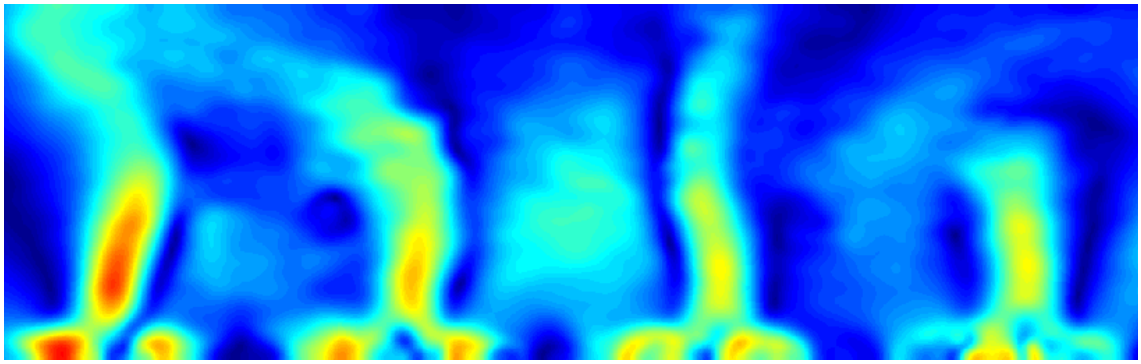

Aerodynamics

TU Delft

Faculty of Aerospace Engineering

Delft University of Technology

Streak control within a turbulent boundary layer using streamwise arrays of plasma actuators

Master of Science Thesis

For obtaining the degree of Master of Science in Aerospace Engineering
at Delft University of Technology

Marcel Hennevelt

July 2, 2012

Faculty of Aerospace Engineering · Delft University of Technology

Delft University of Technology

DELFT UNIVERSITY OF TECHNOLOGY
DEPARTMENT OF AERODYNAMICS

The undersigned hereby certify that they have read and recommend to the Faculty of Aerospace engineering for acceptance the thesis entitled **"Streak control within a turbulent boundary layer using streamwise arrays of plasma actuators"** by **Marcel Hennevelt** in fulfillment of the requirements for the degree of Master of Science.

Dated: July 2, 2012

Supervisors:

Prof. dr. F. Scarano

Dr.ir. G.E. Elsinga

M. Kotsonis, PhD

S. Ghaemi, MSc

Acknowledgements

I would like to thank Prof. Scarano for giving me the opportunity to perform the current thesis work and for his insightful ideas regarding the problems with the experiments. Furthermore, I am indebted to my daily supervisors Sina Ghaemi and Marios Kotsonis for their assistance and guidance during this study. In particular Sina, for spending numerous hours in the wind tunnel with me and always showing incredible interest in my work.

Many thanks to the technical staff at the aerodynamics department, Nico van Beek, Stefan Bernardy, Frits Donker Duyvis, Peter Duyndam and Eric de Keizer, for their assistance when I encountered any technical problems.

In addition, I'd like to thank the fellow MSc students in the 'basement' for allows being ready to help and the interesting off-topic discussions.

Last but not least I would like to thank my family for their encouragement and support during my entire study in Delft.

Abstract

The coherent structures within the turbulent boundary layers have been investigated extensively over the past five decades. In particular, the long alternating low- and high speed streaks in the near-wall region. Along these streaks ejection and sweep events occur which play a major role in the production of Reynolds shear stress. Hence, studies on turbulent boundary layer control were focused on manipulating the low-speed streaks, to either reduce wall skin-friction by attenuating the streaks or by intensifying the streaks for separation control.

The current research focuses on the experimental investigation and optimization of streamwise-oriented plasma actuators that produce wall-normal jets in order to arrange the low- and high speed streaks in a fully developed turbulent boundary layer at low-Reynolds numbers. The rearrangement the meandering streaks into an organized pattern allows future control of turbulent boundary layers without requiring a complicated array of sensors and actuators. A parametric study of the array of dielectric barrier discharge (DBD) actuators is performed to optimize the induced wall-normal jet velocities, which is an appealing method for streak control application, as it is robust, features low power consumption, high actuation frequency and is easy to manufacture. Its ability to control the low-speed streaks was experimentally investigated with particle image velocimetry (PIV).

With the applied actuator configuration the low- and high speed streaks in the near-wall region were effectively arranged into an organized alternating pattern up to free-stream velocities of 13 m/s. At the upstream end of the actuator approximately 5 mm is required to induce the streaks and at the downstream end the organized streaks persist behind the actuator for about 20 mm. Some small spatial meandering of the streaks was observed, nevertheless, these artificially produced streaks exhibited correlation of the streaks for peak-to-peak voltages above 6 kV. In addition, the plasma actuation yielded a significant increase in the magnitude of the ejection events at the locations of the wall-normal jets. These jets also caused the gradient of the streamwise velocity close to the wall to increase, up to a height of approximately 1 mm (or $y^+ \approx 23$). Furthermore, the mixing in the boundary layer is enhanced, showing it can be applied as a mechanism for separation control.

Table of contents

Nomenclature

Greek symbols

Δt	Laser pulse time separation
ψ	Normalized orthonormal basis function
δ^*	Displacement thickness
δ_{99}	Boundary layer thickness
ε	Dielectric coefficient or uncertainty
ε_0	Faraday constant
λ	Eigenvalues or illumination wavelength
μ	Coefficient of dynamic viscosity
ν	Dynamic viscosity
φ	Eigen mode or spatial mode
ρ_f	Fluid density
ρ_p	Particle density
ρ_{zz}	Normalized auto-correlation coefficient
τ_f	Flow characteristic time scale
τ_p	Particle characteristic response time

Latin symbols

a	Orthonormal amplitude coefficients
C	Correlation matrix
D	Aperture diameter
d_{diff}	Diffracted particle size
d_i	Image distance
d_o	Object distance
d_p	Tracer particle diameter
E_b	Breakdown electric field
E_0	Electric field
E_k	Energy content of a POD mode relative to the total energy
F_{el}	Electrostatic force
f	Focal length
$f_\#$	Aperture number
f_{ac}	Actuation frequency of the plasma
g	Gap width
H	Shape factor
L	Length
N	Signal length
M	Magnification factor
p	Pressure
q_n	Net charge level

Re	Reynolds number
Re_δ	Displacement thickness Reynolds number ($U_\infty\delta/\nu$)
Re_θ	Momentum thickness Reynolds number ($U_\infty\theta/\nu$)
Re_τ	Friction velocity Reynolds number ($u_\tau\delta/\nu$)
S_k	Particle Stokes number
t_{exp}	Exposed electrode thickness
T	Temperature
t	Time
$\mathbf{u}$	Velocity vector
$\boldsymbol{U}_s$	Slipping velocity vector
$\boldsymbol{U}_p$	Particle velocity vector
$\boldsymbol{U}_f$	Fluid velocity vector
u	Streamwise velocity or instantaneous streamwise velocity
u'	Fluctuation of the streamwise velocity
$\overline{u}$	Mean of streamwise velocity
u_τ	Friction velocity
V_{ac}	Voltage
V_k	Eigenvector
V_{pp}	Peak-to-peak voltage
v	Wall-normal velocity
w	Spanwise velocity
w_{cov}	Width of covered electrode
w_{exp}	Width of exposed electrode
x	Streamwise coordinate
y	Wall-normal coordinate
z	Spanwise coordinate

Subscripts and Superscripts

+	Indicates viscous scaling, also referred to as inner scaling
‘	Root mean quare value
<u>	Ensemble-averaged quantity
$\overline{u}$	Time-averaged quantity

Acronyms

AC	Alternating current
CCD	Charge couple device
CMOS	Complementary metal oxide semiconductor
DBD	Dielectric barrier discharge
DC	Direct current
DNS	Direct numerical simulation
FOV	Field of view
Laser	Light amplification by stimulated emission of radiation
LSM	Large scale motion
Nd:YLF	Neodymium-doped yttrium lithium fluoride
PIV	Particle image velocimetry
POD	Proper orthogonal decomposition
PSD	Power spectral density
RMS	Root mean squared
SVD	Singular value decomposition
TBL	Turbulent boundary layer
TR-PIV	Time-resolved particle image velocimetry
VLSM	Very large scale motion

1 Introduction

1.1 Background and relevance

Turbulent coherent structures have been studied extensively over the past 50 years. In particular the presence of low-speed streaks in the near-wall region, which were first visualized by Kline et al. (1967). These alternating streaks of low- and high streamwise momentum were observed to have a streamwise spacing of approximately 100 wall units and extend up to lengths of about 1000 wall units (Blackwelder & Eckelmann 1978). In addition, ejection and sweep events have been observed aside the low-speed streaks. A significant part of the turbulent kinetic energy is produced by the ejections (Robinson 1991a). The sweep events are held responsible for increasing wall skin-friction, due to the production of Reynolds shear stress. Therefore, the research on boundary layer control has been focused on controlling the low-speed streaks and related events. The objective of such studies was to reduce the skin-friction by attenuating the streaks (Kerho 2000) or separation control by amplifying the ejection events thereby energizing the low-speed streaks.

In laminar boundary layers various studies were aimed at controlling the low-speed streaks in order to avoid transition, as low-and high speed streaks are involved in the creation of turbulent spots, which eventually evolve into a turbulent boundary layer. To delay transition, the control strategies were often directed towards the attenuation of the streaks. Breuer et al. (1989) used an array of membrane actuators to cancel disturbances introduced at an upstream location by membrane actuation. Myose & Blackwelder (1995) considered suction below the low momentum regions to decrease the growth or even breakdown of the streaky structures. Jacobson & Reynolds (1998) constructed an actuator consisting of a piezoelectric driven beam above a cavity in the wall to damp the streaks generated by a vertical cylinder and an array of suction holes. Lundell & Alfredsson (2003) produced low- and high-speed streaks through suction and amplified the streaks with speakers, thereby forcing instability of the streaks and substantially delay transition. In the more complex experiment of Lundell (2007), upstream located wall-wire signals triggered intermittent suction through holes, in order to damp the streaks induced by free-stream turbulence. Hanson et al. (2010) applied a reactive control system consisting an array of streamwise arranged plasma actuators to cancel disturbance introduced by a roughness array. The above mentioned studies succeeded in manipulating the low- and high speed streaks. However in all studies, except for Lundell (2007), the streaks were forced into the laminar boundary layer in a controlled manner. This is a significant simplification with respect to the situation in a turbulent boundary layer, where the location, amplitude and phase of the disturbances are unpredictable.

Unlike in a laminar boundary layer, streaks in a turbulent boundary layer can have a considerably longer streamwise length and meander in spatial direction, hence often requiring control systems with a higher level of complexity. Hence a feedback control system could be considered for turbulent boundary layers. However, the spanwise spacing of the streaks is approximately 100 wall units, imposing a significant restriction on the size of the actuators. In addition, the meandering of the streaks requires the application of a two-dimensional array of actuators. As a result, the application of reactive control systems in turbulent boundary layers is rarely encountered in literature. An example of such a study is that of Kerho et al. (2000). They used suction holes triggered by upstream sensors to completely remove the low-speed streaks in a turbulent boundary layer to reduce the skin-friction. Rathnasingham & Breuer (2003) induced synthetic jets from a resonance cavity with the aim of reducing turbulent energy, pressure fluctuations and wall shear stress. For their closed-loop control system they applied an identification scheme, which determined when and with what amplitude to actuate.

For the current work, the investigation on rearranging the streaks is conducted with streamwise pairs of dielectric barrier discharge (DBD) actuators. The rearrangement allows the streaks to be manipulated without requiring active control mechanisms. Also the wall-normal jets produced by the plasma actuator configuration can have future applications for suppression of vortex shedding, separation control, drag reduction and laminar-to-turbulent transition control.

DBD plasma actuators represent an appealing method for flow control applications, as they feature no moving parts, low mass, compactness, robustness, low power consumption, high actuation frequency and is easy to manufacture. Furthermore these actuators have already been successfully applied for a wide variety of flow control applications, such as transition delay (Hanson et al. 2010), lift enhancement on airfoils (Corke et al. 2006), turbulent skin-friction drag reduction (Jukes et al. 2006), near-wake flow control (Artana et al. 2003), landing gear noise reduction (Thomas et al. 2005) and have also proven to be effective in boundary layer separation control in low and moderate high Reynolds number flows (Goksel et al. 2006, Sosa & Artana 2006 and Benard & Moreau 2011). The streamwise configuration of plasma actuators was first introduced by Roth et al. (2000), which used them to produce arrays of artificial streamwise oriented vortices. Hanson et al. (2010) also created streamwise vortices with this configuration for the purpose of transition delay.

1.2 Approach

In the current thesis work the objective is

> *to experimentally investigate and optimize streamwise-oriented plasma actuators that produce wall-normal jets in order to arrange the low- and high-speed streaks of a fully developed turbulent boundary layer in an organized alternating pattern without spatial meandering.*

Since the focus will be on the ability of streamwise actuators in controlling the spanwise location of the low- and high speed streaks, the considered flow field should be kept simple. Therefore, the research will be performed on a flat plate, which has a negligible adverse pressure gradient, at low Reynolds numbers.

In order to achieve the described objective the following elements have to be considered:

- Understanding of low- and high-speed streak generation and those of related coherent structures.
- Comprehending of the principles of plasma actuators.
- Determining suitable measurement configurations for the plasma actuators, based on preliminary experiments and by combining the principles of the plasma actuator and streak generation.
- Measuring, visualizing, interpreting and quantifying the velocity fields and induced jet velocities, due to the plasma actuation. The induced velocities are required to determine the ability of streamwise oriented plasma actuators in controlling the spatial locations of the streaks and to optimize the control of these streaks. To get a better understanding of the near-wall turbulent structures the velocity fields close to the wall have to be evaluated. For the measurements particle image velocimetry (PIV) will be the applied experimental diagnostic technique.
- Defining the current limitations of plasma actuation in controlling the low- and high-speed streaks, describing the behavior of the observed turbulent structures and providing recommendations for further investigation.

- Determining the extend by which the artificial streaks persist downstream of the actuator.

1.3 Outline of the Thesis

A literature survey on the turbulent boundary layer is presented in chapter 2, in which statistics of a flat plate turbulent boundary layer and the coherent structures within the boundary layer are discussed. The survey continues in chapter 3, where the principle of the plasma actuator and in specific the dielectric barrier discharge (DBD) actuator is described. Chapter 4 outlines the applied experimental investigation techniques. A description of the experimental setup used in the investigation is given in chapter 5. The results of the experimental investigations without a free-stream flow are presented in chapter 6 and those in the turbulent boundary layer in chapter 7. Finally chapter 8 yields the conclusions and recommendations for future work.

2 Turbulent boundary layers

The current chapter will start off with some flow concepts and comments concerning the investigated flow. In the second section the statistical description of the flat plate turbulent boundary is discussed based on the mean streamwise velocity and Reynolds stress as reported in literature. Furthermore, an explanation on the application of inner and outer scaling, and the division of the boundary layer will be given. Although a turbulent boundary layer seems to have a random nature, there are coherent structures and motions providing (partial) explanation for the events happening with the flow. In section three these structures are described, based on observations from experiments and numerical computations. The discussion will begin with the earliest observed structures and motions, namely the low-speed streaks and the bursting process, followed by a short review of the structures in the outer region of the boundary layer. Afterwards, the so called models of hairpin vortices and hairpin vortex packets are depicted, which provide a possible explanation for various events.

2.1 Boundary layer flow concepts

In the case of fluid motions past a streamlined body, as for example past an airfoil, the influence of viscosity is often confined to a thin layer at the surface. In that thin layer the fluid velocity increases from zero at the wall, due to the no-slip condition, to its (frictionless) free-stream value. An example of such an induced velocity profile on a flat plate is displayed in Figure 2.1. As can be seen the velocity in the region close to the wall is considerably smaller than at a larger distance from it.

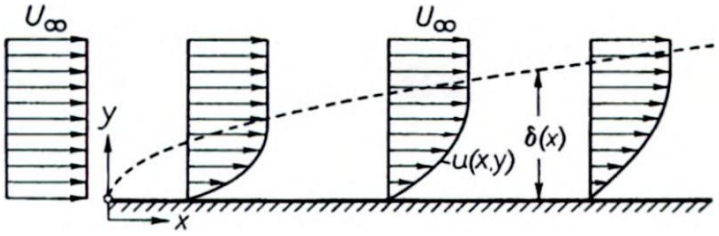

Figure 2.1: Schematic of a boundary layer on a flat plate at zero incidence from Schlichting (1979).

On the wing of an aircraft the boundary layer normally begins as laminar and grows in thickness along the profile until the transition point is reached, after which the boundary layer develops into a turbulent boundary layer.

For boundary layer flows it is customary to denote the coordinate tangential to the wall by x, the wall-normal coordinate by y and the spanwise coordinate by z (see Figure 2.1). The corresponding velocity components are denoted by u, v and w.

The considered turbulent boundary layer (TBL) is established by a uniform-velocity flow over a smooth flat plate. With the coordinate-system as described above, the mean flow is predominantly in the x-direction, the free-stream velocity is denoted by U_∞. The statistics of the flow vary mainly in the y-direction. Nevertheless, the boundary layer continually develops along the x-direction, hence the variations in the statistics are dependent upon both x and y.

Assuming a steady incompressible flow, the Euler equation reduces to

$$\frac{dp_\infty}{dx} \approx -\rho U_\infty \frac{dU_\infty}{dx}, \tag{2.1}$$

where p_∞ is the free-stream pressure and ρ the density, can be applied to describe the pressure changes in streamwise direction (White 2006).

For an accelerating flow ($dU_\infty/dx > 0$) the pressure gradient is negative or favorable and a decelerating flow ($dU_\infty/dx < 0$) gives a positive or adverse pressure gradient. It is called adverse, because it can result in boundary layer separation. In the case of a flat plate boundary layer with constant free-stream velocity, the pressure gradient is approximately zero.

The boundary layer thickness $\delta(x)$ is commonly defined as the height, at which the mean velocity equals 99% of the free-stream velocity U_∞ and is therefore often denoted as $\delta_{99}(x)$. In experiments, the fluctuations in the velocities are significant, making it difficult to accurately determine 99% location. More reliable quantities are integral measures, such as the displacement thickness

$$\delta^* = \int_0^{y\to\infty} \left(1-\frac{u}{U_\infty}\right) dy\,, \tag{2.2}$$

and momentum thickness θ

$$\theta = \int_0^{y\to\infty} \frac{u}{U_\infty}\left(1-\frac{u}{U_\infty}\right) dy\,, \tag{2.3}$$

which are derived from the conservation of mass and momentum (White 2006). Based on these thicknesses the shape factor is defined as

$$H = \frac{\delta^*}{\theta}\,. \tag{2.4}$$

Furthermore, the above parameters allow various expressions of the Reynolds number to be determined, based on either a streamwise or wall-normal length scale:

$$\mathrm{Re}_x = \frac{U_\infty x}{\nu} \quad \text{or} \quad \mathrm{Re}_{\delta_{99}} = \frac{U_\infty \delta_{99}}{\nu}\,, \tag{2.5}$$

where ν is the kinematic viscosity ($= \mu/\rho$, μ is the dynamic viscosity).

In a zero-pressure gradient boundary layer, the flow begins as laminar from the leading edge, until the flow reaches the critical Reynolds number $Re_{x,\mathrm{crit}}$, from where the transition will start. The value of $Re_{x,\mathrm{crit}}$ varies, but is approximately 10^6. After the transition the boundary layer is fully turbulent. To promote an early transition from laminar to turbulent, a trip wire or carborundum is sometimes employed in experiments.

2.2 Statistical description of a flat plate turbulent boundary layer

A detailed statistical review of the flat plate turbulent boundary layer would be futile, since it had been studied extensively since Prandtl (1904). Furthermore, the field can be narrowed because only statistics of low Reynolds number flows are relevant for comparison with the current work.

The current section presents the relevant flow statistic subjects as mentioned in literature, such as the mean streamwise velocity, normal stress in streamwise and wall-normal direction and the Reynolds shear stress.

2.2.1 Mean streamwise velocity

In order to simplify the problem of turbulence, the two-dimensional zero-pressure gradient flat plate turbulent boundary layer has been investigated thoroughly. This particular boundary layer flow is often referred to as “canonical” and has been shown to be fairly self-similar (Clauser 1956) for the mean streamwise velocity component.

With intention of finding self-similar pr0ofiles, the boundary layer must be divided into an inner and outer layer (Townsend 1956). In the outer layer the mean velocity profile is dependent upon δ and U_∞, while in the inner layer the profile is determined by viscous scales. Hence, the variables of the outer scaling are u/U_∞ and y/δ. The appropriate viscous velocity and length scale are defined as, respectively, the friction velocity $u_\tau = \sqrt{\tau_w/\rho}$ and the viscous length scale $\delta_\nu = \nu/u_\tau$, where τ_w is the wall shear stress, ρ the density and ν the kinematic viscosity. The variables of inner scaling y^+ and u^+ are expressed in wall units as displayed in equation(2.6).

$$y^+ = \frac{y u_\tau}{\nu} = \frac{y}{\delta_\nu}$$
$$u^+ = \frac{u}{u_\tau} \tag{2.6}$$

Inside the inner layer in the region close to the wall viscosity effects dominate the flow. This region is known as the laminar viscous sublayer ($y^+ < 5$), where the mean velocity profile can, consequently, be described by

$$u^+ \approx y^+ \qquad \text{for } y^+ < 5. \tag{2.7}$$

Near-wall profiles from DNS data of Wu (2009) and Spalart (1988) in Figure 2.3 verify that the deviations from the linear relation $u^+ = y^+$ are negligible for $y^+ < 5$.

The inner layer is usually defined as $y/\delta < 0.1$. At the outer part of the inner layer ($y/\delta \approx 0.1$) viscosity has a little affect, hence turbulence dominates the flow. At that location of the boundary layer the profile has a logarithmic region, which is referred to as the log-law region ($y^+ > 30$, $y/\delta < 0.3$). An example showing the presence of a logarithmic region for a set of low-Reynolds number measurements is displayed in Figure 2.2. Within this region the logarithmic law of the wall (Von Kármán 1930) or log-law is valid, which is given by

$$u^+ \approx \frac{1}{\kappa}\ln y^+ + B \qquad \text{for } y^+ > 30,\ y/\delta < 0.3, \tag{2.8}$$

where Von Karman constant $\kappa \approx 0.41$ and the constant $B \approx 5.0$, because a smooth wall is assumed. Note that the log-law is only valid in a region where direct viscous effects are negligible and the shear stress is approximately constant. The semi-log plot illustrates the collapse of data to a single curve for $y^+ > 30$, which is in agreement with logarithmic law of the wall, until the point where the log-law is no longer valid.

Note, the no-slip condition at the wall allows the wall shear stress, which is defined as

$$\tau_w = \mu\left(\partial u/\partial y\right)_{y=0}, \tag{2.9}$$

to be determined by a curve fittings of measurement data. Note the determination with “law of the wall” in the viscous sublayer has a higher accuracy, due to its validity in the near-wall region.

Between the viscous sublayer ($y^+ < 5$) and the log-law region ($y^+ > 30$) there is a region, called the buffer layer, where transition from the viscosity-dominated to turbulence-dominated flow occurs. A summary of various regions and layers in the boundary layer by Pope (2009), is presented in Table 2.1.

Figure 2.3 displays mean velocity profiles of u^+ as a function of y^+ plotted in semi-logarithmic form for three flows: a boundary layer direct numerical simulation (DNS) of Wu (2009) at Re_θ = 900, the experimental data of Murlis et al. (1982) at Re_θ = 791 and another boundary layer DNS by Spalart (1988) at Re_θ = 670. The meticulous matching of the profiles illustrates the universality of the law of the wall in the log-law region but also in buffer layer and viscous sublayer. For lower Reynolds number DNS data readers are referred to Komminaho & Skote (2002) and for higher Reynolds numbers to Simens et al. (2009) and Schlatter & Örlü (2010).

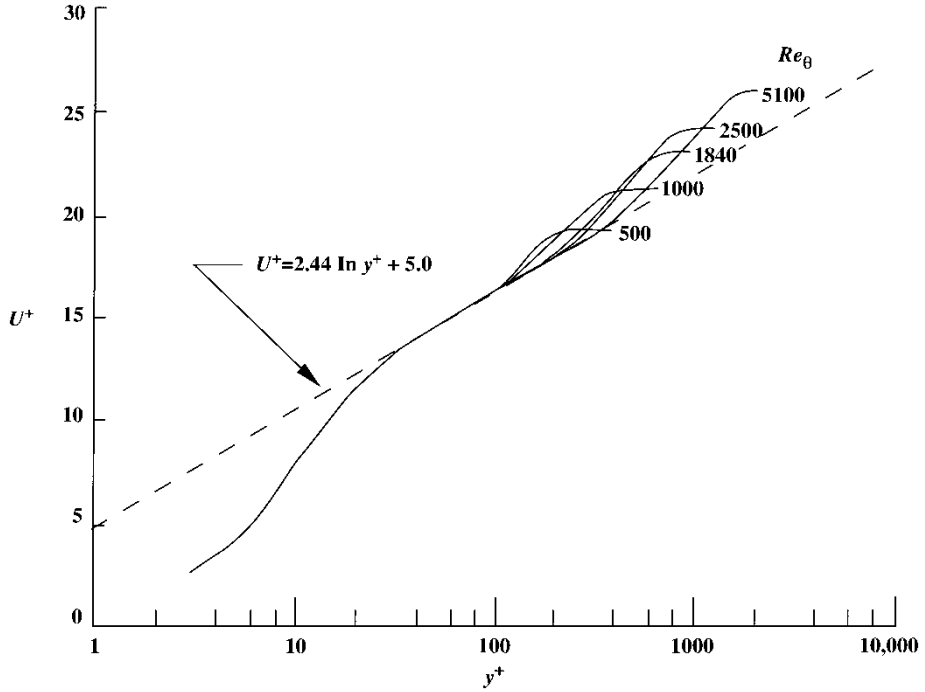

Figure 2.2: Mean velocity profiles of set of low-Reynolds number measurements by Purtell, et al. (1981).

Table 2.1: Regions and layers of the boundary layer by Pope (2009)

Inner layer	$y/\delta < 0.1$	Scaling with u_τ and y^+
Viscous wall region	$y^+ < 50$	Viscous contribution to the shear stress is important
Viscous sublayer	$y^+ < 5$	Reynolds stress negligible compares to viscous stress
Buffer layer	$5 < y^+ < 30$	Overlap between viscous sublayer and log-law region
Outer layer	$y^+ > 50$	Direct effects of viscosity are negligible
Overlap region	$y^+ > 50$, $y/\delta < 0.1$	Overlap between inner and outer layers
Log-law region	$y^+ > 30$, $y/\delta < 0.3$	The log-law holds

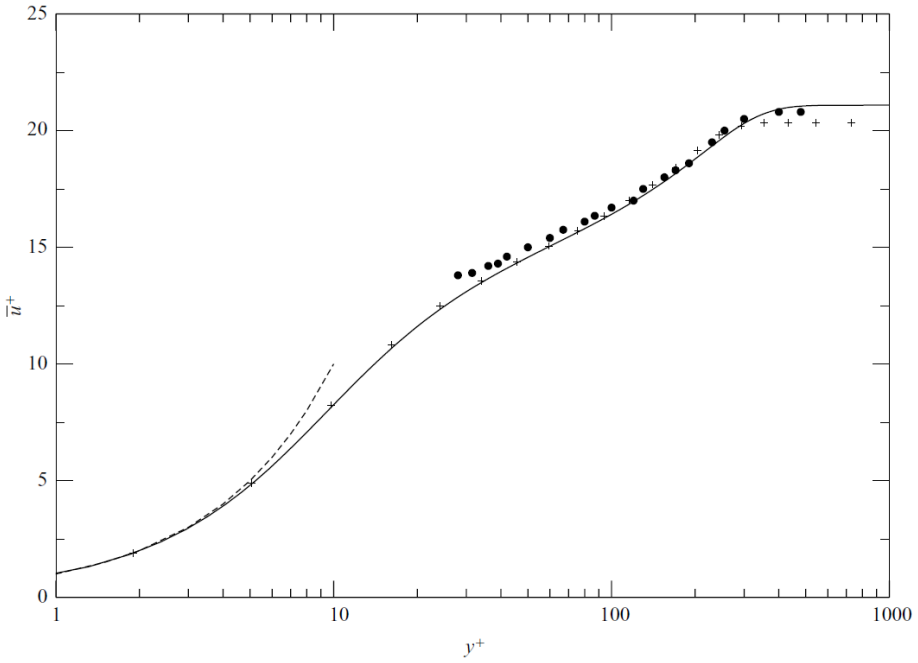

Figure 2.3: Mean velocity profile u^+ as a function of y^+. Dashed line, $u^+ = y^+$; solid line, Wu (2009) at Re_θ = 900; Murlis et al. (1982) at Re_θ = 791; plus, Spalart (1988) at Re_θ = 670. Figure from Wu (2009).

2.2.2 Reynolds stresses

Before considering the Reynolds stresses some data analysis tools need to be discussed for clarity on the definitions.

When examining a velocity field, it can be decomposed into a mean and fluctuating component as

$$u(\mathbf{x},t) = \bar{u}(\mathbf{x}) + u'(\mathbf{x},t), \tag{2.10}$$

where $u(\mathbf{x},t)$ is the instantaneous, $\bar{u}(\mathbf{x})$ the mean and $u'(\mathbf{x},t)$ the fluctuating part of the streamwise velocity field. To indicate the fluctuations around the mean, commonly the root-mean-square (RMS) is considered for quantifying the temporal fluctuations around the time-averaged, which is given by

$$u_{rms} = \sqrt{\frac{1}{N}\sum_{n=1}^{N}\left(u(\mathbf{x},t_n) - \bar{u}(\mathbf{x})\right)^2} = \sqrt{\frac{1}{N}\sum_{n=1}^{N}\left(u'(\mathbf{x},t_n)\right)^2}, \tag{2.11}$$

where N is the number of samples. The covariance of two signals, here for example u' and v', is defined by

$$\overline{u'v'} = \frac{1}{N}\sum_{n=1}^{N} u'_n v'_n . \tag{2.12}$$

The covariance of a signal with itself is the variance and is given by

$$\overline{u'^2} = u_{rms}^2 . \tag{2.13}$$

By examining the (co)variance, a statistical description of the Reynolds stresses in an incompressible flow can be determined. For a two-dimensional flow the normal stresses are described by the covariance's $\overline{u'^2}$ and $\overline{v'^2}$, and the Reynolds shear stress by the variance is $\overline{u'v'}$. The covariance's in non-dimensional form are defined as $\overline{u'^2}^+$ and $\overline{v'^2}^+$. Similarly the two-dimensional variance is denoted by $\overline{u'v'}^+$. Instead of the (co)variance's, often the non-

dimensional root-mean-square values u'^{+}_{rms} and v'^{+}_{rms} are presented, to express the intensity of turbulence fluctuations.

Honkan & Andreopoulos (1997) examined the RMS values of axial, normal and spanwise velocity components and profiles of the Reynolds stress from 11 groups. Although their data shows significant differences in the streamwise and wall-normal intensities in a Reynolds number range of 2600 < Re_θ < 2790, the experimental data of the turbulence intensities lying outside this range display only relatively small deviations. Furthermore, their study showed that Reynolds shear stresses experimentally obtained from the near-wall region of a turbulent boundary layer, exhibits no consistent trend and does not agree with the DNS data of Spalart (1988). In fact, the compared experimental data displayed considerable scatter regardless of the applied scaling parameter. They attributed most of the discrepancies in the measurements of the Reynolds stresses and turbulence intensities to spatial resolution effects of the probes, differences in the applied measurement techniques and the errors involved in controlling the experimental conditions. In addition, they explained that the peaks in the turbulence intensities in the classical data from Klebanoff (1954) for y/δ < 0.4 are due to non-equilibrium effects, caused by the upstream tripping of the boundary layer with a long roughness strip.

Figure 2.4 shows the turbulence intensities in the form of normalized RMS values plotted for outer wall units. The lines are DNS data of Wu (2009) at Re_θ = 900. Furthermore, the experimental data of Erm & Joubert (1991) at Re_θ = 697 and the streamwise turbulence intensity u'^{+}_{rms} of Purtell, et al. (1981) at Re_θ = 1340 are presented. In agreement with the above discussed, the data for each turbulence intensity displays there is a fairly consistent trend for low Reynolds numbers.

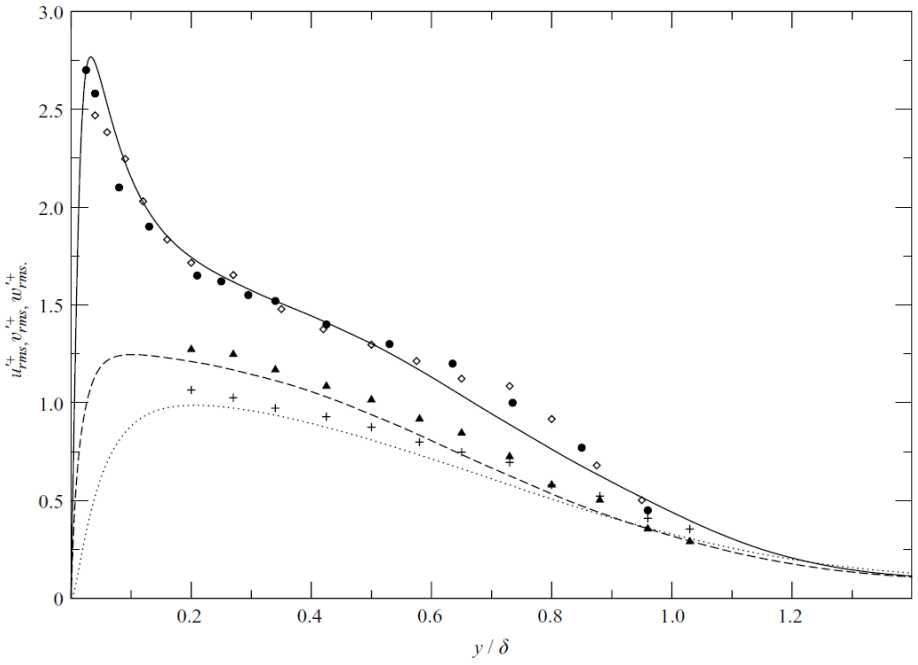

Figure 2.4: Turbulence intensities as a function of y/δ. Lines are from the DNS of Wu (2009) at Re_θ = 900. Solid line, u'^{+}_{rms}; dotted line, v'^{+}_{rms}; dashed line, w'^{+}_{rms}; solid circle, Purtell et al. (1981) at Re_θ = 1340; all other symbols, Erm and Joubert (1991) at Re_θ = 697. Figure from Wu (2009).

The non-dimensional Reynolds shear stress $-\overline{u'v'}^{+}$ is plotted in Figure 2.5 as a function of y/δ. The dashed line is from the DNS data of Wu (2009) at Re_θ = 900. Also the data of measurements of DeGraaff & Eaton (2000) at Re_θ = 1430, Honkan & Andreopoulos (1997) at Re_θ = 2790 and Spalart (1988) at Re_θ = 670 are shown. The DNS results lie close together,

while the values measured by Honkan & Andreopoulos (1997) are significantly higher and those of DeGraaff & Eaton (2000) considerably smaller. Thereby, showing there is no consistent trend for experimentally obtained Reynolds shear stresses.

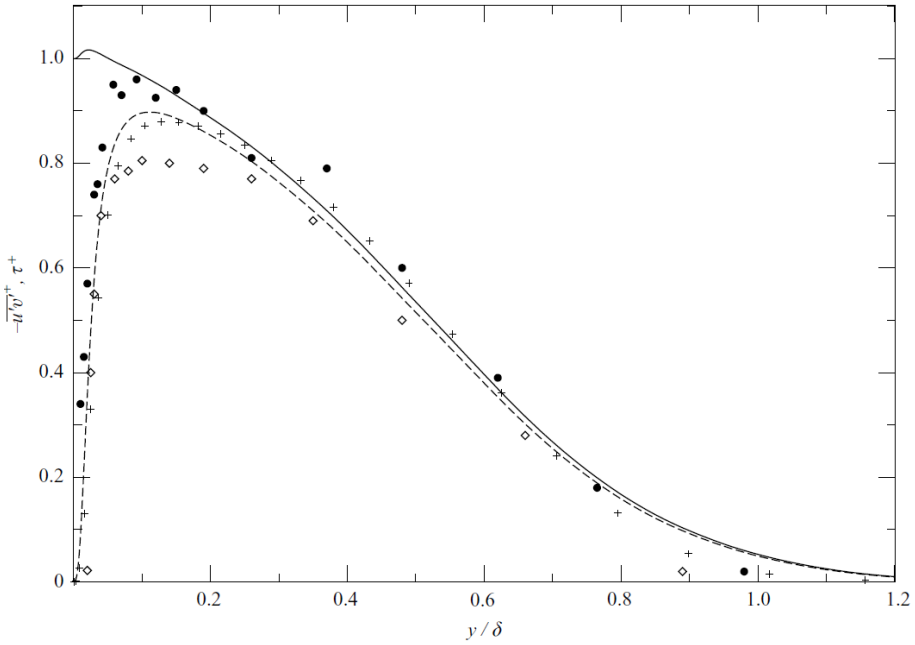

Figure 2.5: Reynolds and total shear stress as a function of y/δ. Solid line, total shear stress τ^+ from Wu (2009) at Re_θ = 900; dashed line, $-\overline{u'v'}^+$ from Wu (2009) at Re_θ = 900; solid circle, Honkan and Andreopoulos (1997) at Re_θ = 2790; diamond, DeGraaff & Eaton (2000) at Re_θ = 1430; plus, Spalart (1988) at Re_θ = 670. Figure from Wu (2009).

2.3 Unsteady organization

In beginning of turbulent boundary layer research, the turbulence within the boundary layer was viewed as a random fluctuating velocity field around a well-defined mean, where the only approach was to adopt a statistical view (see for example Schlichting 1979 and Murlis et al. 1982). More recently the investigation moved to understanding the "random motions" in the boundary layer, which appeared to have coherence in both space and time. These so called "coherent structures" have been extensively studied for many decades, but still no generally accepted definition has emerged. According to a rather general description by Robinson (1991a) a coherent structure can be defined as a,

> "*three-dimensional region of the flow over which at least one fundamental flow variable (velocity component, density, temperature, etc.) exhibits significant correlation with itself or with another variable over a range of space and/or time that is significantly larger than the smallest local scales of the flow.*"

The understanding of the coherent structures in a turbulent boundary layer is of great importance for the manipulation of the low- and high speed streaks, since multiple coherent structures are involved in the creation of these streaks.

The below discussion of the structures and organization of the turbulent boundary layer will be mainly focused on low Reynolds number flows. Cantwell (1981), Robinson (1991a), Panton (2001) and Adrian (2007) provided extensive reviews on the subject. For higher

Reynolds number turbulent flows the readers are referred to the reviews of Marusic et al. (2010) and Smits et al. (2011).

2.3.1 Low-speed streaks and the bursting process

Early on in the investigation of coherent structures predominantly flow visualization techniques were applied for investigation, which were also mainly focused on the viscous sublayer. Among such groups were Kline et al. (1967), which showed long streamwise streaks, corresponding to an accumulation of hydrogen bubbles, in close proximity to the wall. An example displaying the low-speed streaks within a turbulent boundary layer at a height of $y^+ \approx 7$ is presented in Figure 2.6. Near the wall ($y^+ < 7$) the spanwise spacing between the streaks was found to be approximately 100 δ_v, up to Reynolds numbers of at least $Re_\theta \approx 6000$. These elongated streamwise streaks were shown to be regions of low streamwise velocity and the regions between the streaks that of high streamwise velocity. Later Smith and Metzler (1983) found the spacing between the streaks increases with the distance from the wall. For the streamwise length of the streaks distances of 2000-3000δ_v have been reported (Adrian 2007).

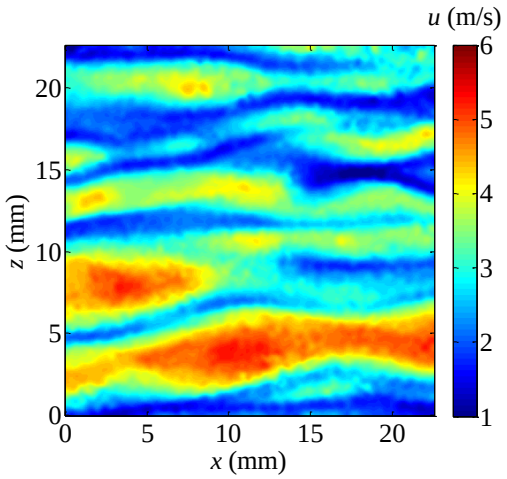

Figure 2.6: Contour plot of an instantaneous streamwise velocity field at a height of $y^+ \approx 7$, which depicts the low- and high speed streaks within a turbulent boundary layer.

The streaks extend from the viscous sublayer into the buffer region, where a characteristic behavior, known as bursting, was observed. During the process of bursting, a streak of low-speed fluid migrates slowly away from the wall while slowly drifting downstream (gradual outflow), when the streak reaches y^+ = 8-12, it starts to exhibit a rapid oscillation which increases in amplitude and terminates with an abrupt breakup between y^+ = 10-30. After the breakup the streak lifts away from the wall by a vigorous and chaotic motion. This process 'ejects' low-speed fluid into a region of the boundary layer with a faster streamwise velocity. During the rapid lifting or 'ejection' low speed fluid is carried away from the wall, causing an inflectional zone in the velocity profile, as illustrated in Figure 2.7. Moreover, Kline et al. (1967) observed that a favorable pressure gradient ($dp/dx < 0$) reduces the bursting rate, while an adverse pressure gradient ($dp/dx > 0$) leads to an increase of the bursting intensity.

Since the kinetic energy of turbulent structures is continually dissipated to heat by viscous dissipation, a continuous supply of new turbulent motions has to be generated to maintain a quasi-steady state within the flow. Klebanoff (1954) had stated the majority of the turbulent kinetic energy production occurs in the near-wall region, just outside the viscous sublayer. With the observation of the bursting phenomena, the corresponding 'ejection' event appeared to play a significant role in the transfer of momentum and energy between the inner

and outer layer. In fact, later Kim et al. (1971) would observe that the bursting process produces essentially all of the turbulence in the region $0 < y^+ < 100$.

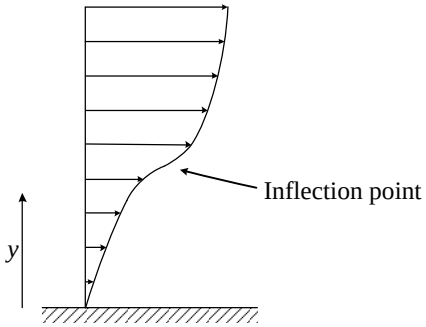

Figure 2.7: Example of a velocity profile with inflexion point.

In contrast to Kline et al. (1967), Corino and Brodkey (1969) noticed that ejections originate from a region between $5 < y^+ < 15$. Hence, concluding that the viscous sublayer ($y^+ < 5$) is passive. Moreover, they observed each ejection event ended with a sweeping motion, carrying a packet of high momentum fluid from the outer layer close to the wall, called a sweep. Hence, bringing forth the question of possible inner-outer layer interaction. Furthermore, they found the ejections increased in frequency and intensity for increasing Reynolds number. Offen and Kline (1975) observed that an ejection, which pushes low-momentum fluid away from the wall, is followed by a downward flow of high-momentum fluid splashing against the wall to replace the low-momentum fluid. Suggesting the sweep event is only a remainder of an ejection.

Then nearly two decades after the bursts were first observed, Bogard and Tiederman (1986) revealed that bursts do not comprise of a single ejection, but rather of series of increasingly stronger ejection events.

The bursting concept excited researchers to seek mechanisms to explain the origin of the explosive upward events. They started using quadrant analysis on time series data in order to identify the events happening before and after the bursts. Quadrant analysis applies the quadrant splitting scheme, introduced by Wallace et al. (1972) and Willmart and Lu (1972), to divide the turbulent motions into four classes (see Figure 2.8). This *uv* splitting scheme was chosen above others, because of the strong association with the Reynolds shear stress, $-\rho\overline{uv}$. According to the scheme the ejections and sweeps are defined as Q_2 and Q_4 motions, since events in the second quadrant correspond to negative streamwise fluctuations being lifted away from the wall by positive wall-normal fluctuations ($u < 0$, $v > 0$) and events in the fourth quadrant to positive streamwise fluctuations being moved toward the wall ($u > 0$, $v < 0$). Since the ejection events push low-streamwise momentum fluid away from the wall, they reduce the streamwise velocity gradient in the near-wall region, thereby locally decreasing the Reynolds shear stress and thus the skin-friction at the wall. Sweep events have the opposite effect, yielding an increase in Reynolds shear stress close to the wall. The other two quadrants, outward interaction Q_1 and wallward interaction Q_3, have a negative contribution to the Reynolds shear stress.

By applying quadrant analysis, Wallace et al. (1972) showed that at $y^+ \approx 15$ the contributions of the ejections and sweeps to the Reynolds stress are almost equal and significantly larger than the outward and wallward interactions. Ejections dominate the Reynolds stress in the region beyond $y^+ \approx 15$, while sweeps are the major contributor in the region closer to the wall ($y^+ < 15$), as the probability density function is showing in Figure 2.8. In addition, Willmart and Lu (1972) performed a quadrant analysis with only the strong *uv*-events. They found that the largest contribution was from the Q_2 events (ejections) and the second largest from the Q_4 events (sweeps). The duration and frequency of these events was found to be equal.

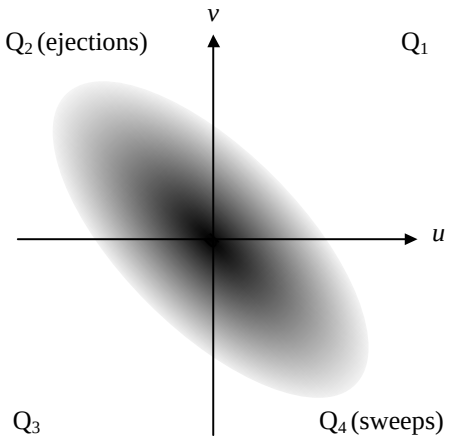

Figure 2.8: Quadrant splitting scheme showing the probability density function in the *u-v* plane.

Blackwelder and Eckelmann (1979) showed the near-wall region is well populated with counter-rotating quasi-streamwise vortices, which have been found to be responsible for both the ejection and sweep events of the bursting process and also redistribute the streamwise velocity into alternating high- and low-speed streaks (see Figure 2.9). They found the streamwise vortices attaining lengths of approximately $1000\delta_v$. These structures have been related to hairpin vortices, which will be discussed later in this chapter. The relation between these coherent structures has been verified by various direct numerical simulation (DNS) studies (Kim et al. 1987, Jiménez and Moin 1991 and Schoppa and Hussain 2000). Furthermore, since the ejection and sweep events are the major contributor to the Reynolds stress in the wall region, the quasi-streamwise vortices have the dominant role in turbulence production and drag generation (Robinson 1991a). In fact, Choi et al. (1993) proved that streamwise vortices above the wall are associated to local regions of high skin-friction. The regions are created by the sweeping motions, which are induced by the streamwise vortices.

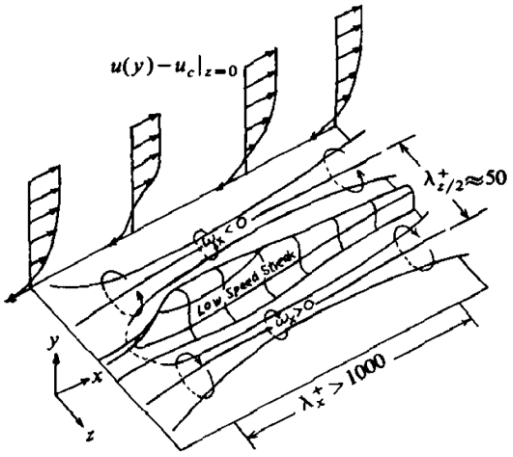

Figure 2.9: A pair of counter-rotating streamwise vortices with the resulting low-speed streak (Blackwelder 1978).

To summarize, the low- and high speed streaks are believed to originate in the viscous sublayer ($y^+ < 5$) and extend up into the buffer layer ($5 < y^+ < 30$). The width of the low-speed streaks depends on the distance from the wall, however the spanwise spacing has been observed to have a relatively constant spacing of $100 \pm 20\delta_v$. The streamwise extension of these streaks exceed their spanwise coherence by far with reported lengths of $2000\text{-}3000\delta_v$.

Along the low-speed streaks ejection and sweep events are observed, which dominate the Reynolds stress production in, respectively, the regions above and below $y^+ \approx 15$. Additionally, the majority of the turbulent kinetic energy in the boundary layer is produced in the buffer layer by these events.

2.3.2 Outer layer structures

The outer layer of a turbulent boundary is usually defined by $y^+ > 50$ (see Table 2.1), where the direct effects of viscosity have become negligible. Within this region there exists a sharp interface separating the turbulent interior from the non-turbulent exterior (Figure 2.10), where three-dimensional large-scale motions or bulges of the scale of the boundary layer thickness are formed. Corrsin (1943) showed with experiments that the outer edges of the interior are only intermittently turbulent. This behavior of turbulence was verified by Corrsin and Kistler (1954) and Klebanoff (1954). Kovasznay *et a1*. (1970) observed that inside the turbulent region the fluid is moved around by a slow convective motion induced by large eddies. At the outer edge of the interior, deep irrotational valleys are present through which free-stream velocity is entrained into the turbulent interior. Also shear layers of δ-scale are formed, due to relatively high-velocity fluid impacting on the upstream side of the bulges, even at high Reynolds numbers.

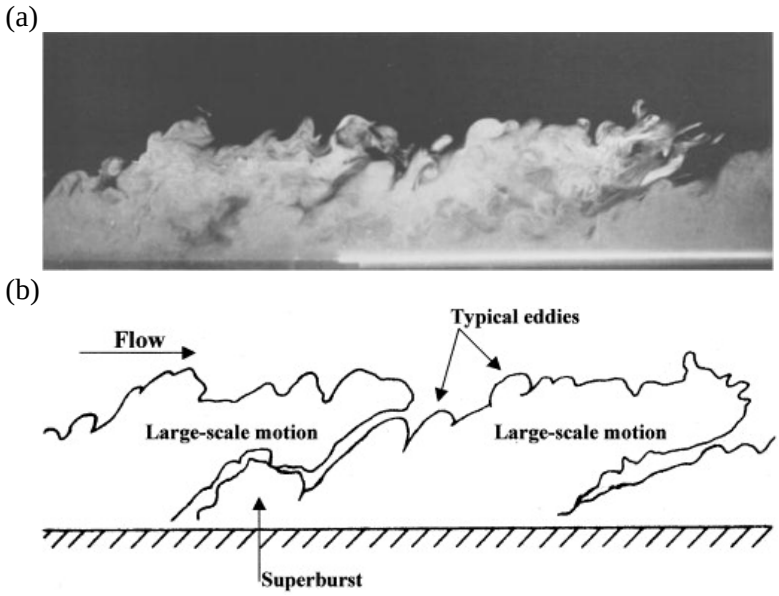

Figure 2.10: (a) Smoke visualization of a turbulent boundary layer by Falco (1977) and **(b)** Schematic visualization by Falco (1977) indicating the presence of bulges (LSMs) and typical eddies.

Additionally, Kovasznay *et a1*. (1970) determined that individual bulges are correlated over 3δ in streamwise and δ in spanwise direction. Furthermore, they suggested only the creation of new large-scale motions could maintain the Reynolds stress in the outer region. Moreover, they proposed the bursts observed by Kline et al. (1967) in the near-wall region to be responsible for the large-scale motions in the outer layer.

As an extension to their earlier work Blackwelder and Kovasznay (1972) performed measurements close to the wall. They observed violent motions, which remained correlated up to a height of $y/\delta \approx 0.5$, thereby confirming their proposition that the perturbations related to bursts extend across the entire boundary layer.

In combined visual (oil droplets) and hot-wire experiments Falco (1977) found a repetitive family of highly coherent motions, called ‘typical eddies’, ‘Falco eddies’ or ‘pockets’ (see Figure 2.10). These small-scale eddies appeared at the trailing interface of a

bulge, which he associated with Reynolds-stress producing motions. The length scales of 'typical eddies' are on the order of 100 to 200δ_v.

Head and Bandyopadhyay (1978) employed smoke visualizations and hot-wire measurements, where they observed structures being formed that are small in streamwise direction but highly elongated at an inclination of approximately 40° to the surface. They concluded these structures represent hairpin vortices, which will be discussed in the next section. Furthermore, they suggested the Falco eddies at the edges of the turbulent interior are in fact tips of the hairpin vortices.

More recently measurements of spectra from Kim and Adrian (1999) revealed the presence of a previously unknown coherent structure in the outer layer, called very large-scale motion (VLSM). These VLSMs appear to have a significant contribution to the total energy content at all locations above the wall and have a characteristic length scale of the order of 10δ. According to Kim and Adrian (1999) VLSMs are related to a peak in the pre-multiplied streamwise spectrum at low wave numbers. Unfortunately their source has not yet been determined (for more details see Marusic et al. 2010). Marusic (2001) observed that VLSMs can have a contribution up to half of the total energy.

An example of smoke visualization by Falco (1977) is presented in Figure 2.10, which illustrates several coherent structures in the outer layer. The manner in which the inner region and outer layer interact is still open for debate. However, evidence suggests there is momentum transfer between the layers due to ejection events. Also the growth of vortical structures from the wall region to the outer layer leads to interactions. Furthermore, it is unclear how the turbulent outer layer influences the turbulence production in the near-wall region.

2.3.3 Single hairpin vortex

Theodorsen (1952, 1955) proposed a horseshoe vortex model for boundary layer turbulence production and dissipation (Figure 2.11). The model described the loop-like vortical structures originating at the wall and growing outward with the top inclined 45° downstream. Furthermore, he proposed these structures to be the primary elements of wall-bounded turbulence. The possible presence and significance of such hairpin vortices in turbulence production has long been debated (see for example Cantwell 1981 or Robinson 1991a).

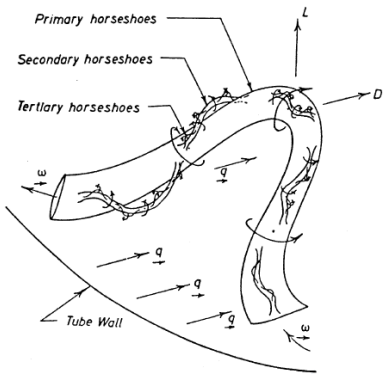

Figure 2.11: Horseshoe vortex model of Theodorsen (1952).

It was not until smoke visualizations of boundary layers of Head and Bandyopadhyay (1981) provided experimental evidence of such hairpin-shaped structures dominating the turbulent boundary layer over a range of Reynolds numbers. They observed large scale structures which were composed of a collection of hairpin vortices. These hairpin loops were straight over a considerable portion of their length and inclined at an angle of about 45°. At higher Reynolds numbers, the hairpin vortices were elongated, while at low Reynolds numbers, the vortices showed less elongation and were more horseshoe shaped (Figure 2.12). For both low and high Reynolds numbers the hairpins extended from the wall to the edge of

the boundary layer and constant spanwise width of about $100\delta_v$. The corresponding large scale structures consisted of just one or two vortices.

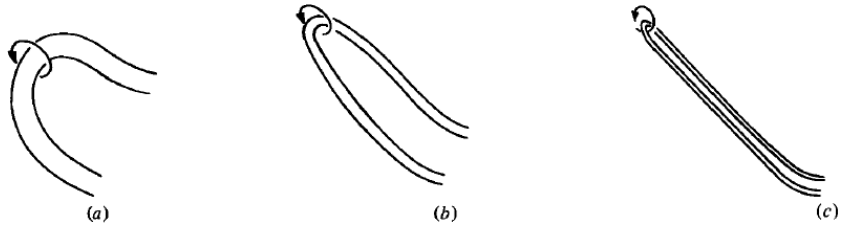

Figure 2.12: The effects of the Reynolds number on the shape of hairpins. **(a)** Very low *Re* (loops); **(b)** low-moderate *Re* (elongated loops); **(c)** moderate-high *Re* (elongated hairpins). From Head and Bandyopadhyay (1981).

Robinson (1991a, 1991b) added a significant amount of knowledge by examining DNS data. For reviewing the DNS results of Spalart (1988) it was necessary to divide the hairpin structures into three parts: legs, neck and head, as is shown in Figure 2.13. He also concluded that these structures are not necessarily symmetric, in fact they are more often asymmetric and are commonly shaped like arches or canes. Furthermore, Robinson suggested that as hairpins are convected by a shear flow, the legs become elongated and eventually become counter-rotating quasi-streamwise vortices. However, his proposition on how streamwise vortices are created is still topic of debate.

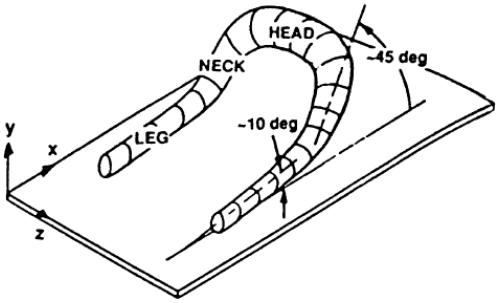

Figure 2.13: The parts of a hairpin vortex, as defined by Robinson (1991b).

From the particle image velocimetry (PIV) experiments Adrian et al. (2000) were able to provide a characteristic signature of a single hairpin vortex (Figure 2.14): a small region of vorticity in the head, a Q_2 event (ejection) located beneath the head and perpendicular to the plane containing the head and neck, the stagnation point marking the location of the shear layer resulting from the Q_2 (ejection) and Q_4 (sweep) interaction and finally the presence of a low-speed streak close to the wall. In Figure 2.14(b) it is observed that the Q_2 events occur at inclination of approximately 45 degrees to the wall. The curvature of the head and neck is important for concentrating the induction in the inboard region, which is consistent with the Q_2 events being stronger than the Q_4 events.

More recently, a DNS study of Wu and Moin (2009) corroborated the observations of the densely populated presence of hairpins in turbulent boundary layers made by Head and Bandyopadhyay (1981), thereby settling almost three decades of discussions about the existence of hairpins in turbulent shear flows.

To recapitulate, there is significant evidence for the existence of the hairpin vortex. The single hairpin gives an explanation for many observations mentioned in literature. More importantly, it produces an explanation for creating low-speed streaks, Reynolds shear stress and for transporting energy from the near-wall region to the outer layer.

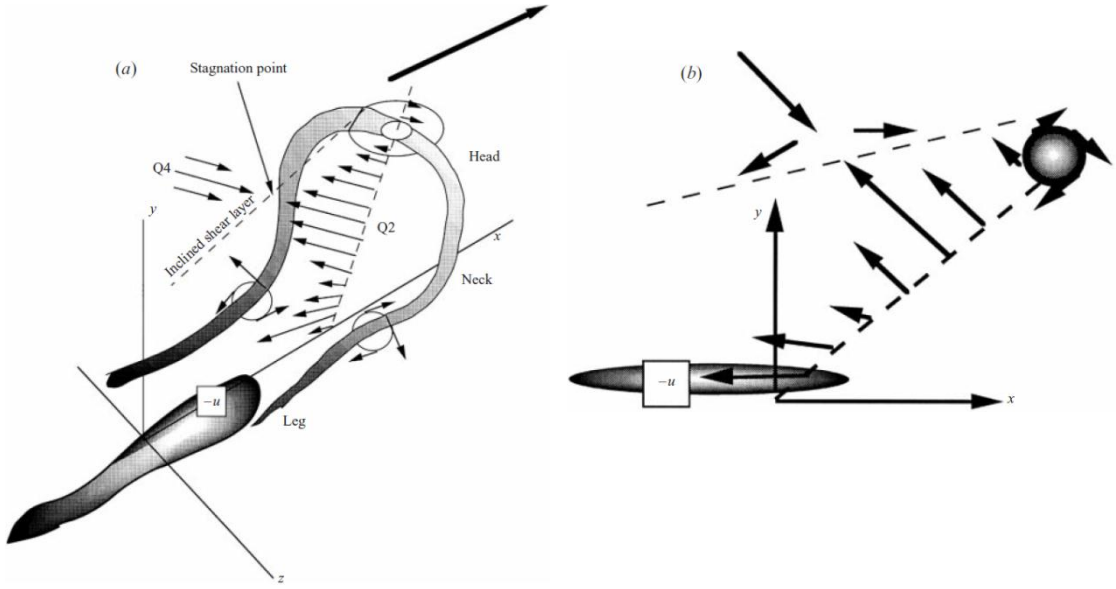

Figure 2.14: (a) Schematic of a hairpin vortex showing the characteristic hairpin vortex signature. **(b)** Hairpin signature in the *x*-*y* plane. From Adrian et al. (2000).

2.3.4 Hairpin vortex packets

As already mentioned, Head and Bandyopadhyay (1981) provided the first experimental prove for the existence hairpins vortices in turbulent wall flows. In addition, they discovered that hairpins frequently occur in packets of increasingly taller hairpins. Smith et al. (1984) also accomplished to visualize hairpins vortices displaying the same formation of successive in-line hairpins.

Although Liu et al. (1991) presented visualizations of PIV recordings, showing the vorticity patterns consistent with hairpin vortices close to the wall. It was not until Adrian et al. (2000) that the first evidence of hairpins occurring in streamwise succession was obtained with PIV. From this PIV study it was concluded that hairpins commonly occur as 'packets', which are called so because of their small dispersion in the propagation velocity. Actually, Adrian et al. (2000) noticed that in 85% of all PIV images there was at least one hairpin vortex packet present. They also reported dispersions of approximately 7% of the free-stream velocity, such that the relative distance between hairpins in a packet remains coherent for long times. These packets can contain more than 10 hairpins, and extend up to height of 0.8δ and due to the small velocity dispersion may be as long as 2δ. The number of heads within a packet increases with the Reynolds number. Moreover, it was observed many hairpin packets, each with their own propagation velocity, occur within another packet, at various stages of growth. The younger packets are smaller and lie close to the wall, while they are contained within a larger and older packet with weaker backward induced flow, as is depicted in Figure 2.15.

The most common configuration of the envelope of a packet, is shaped as a linearly growing ramp and is observed more in high Reynolds number flows (Meinhart et al. 1995). Due to the nesting of one packet within another, several zones of nearly uniform momentum are present within the larger and older ramp-shaped structures. The creation of these structures can be ascribed to the coherent vortex induction inboard of the hairpin vortex packets. Coherent vortex induction is the effect resulting from the addition of induced fields of multiple hairpins.

The hairpin packet concept provides an explanation for the sequence of events occurring in bursts. The passage of each hairpin would cause up and down flow, due to the ejection and sweep events, thereby creating the oscillation. The amplitude of the oscillation increases as the smaller end of the packet approaches, since the induction (ejection events) increase in strength as the scale of the hairpin vortex decreases. When the end of the packet is

reached, the back-induced flow will no longer be influenced by the downwash of an upstream hairpin, hence a very strong ejection event can be observed. Furthermore, the backflow induced on the inboard region of a hairpin packet, caused by the Q_2 events, is considerably longer than that of a single hairpin vortex, hence explaining the remarkably long correlation lengths of 2000-3000δ_v (Adrian 2007) of low-speed streaks. As the hairpins within these packets may not be perfectly aligned, it also provides an explanation for the meandering of the streaks.

As for single hairpin vortices, also many conceptual models exist on how hairpin packets are created. However, there is no definitive determination for which processes trigger the creation of new packets. It is only known that something is triggering the formation of packets and in large quantities.

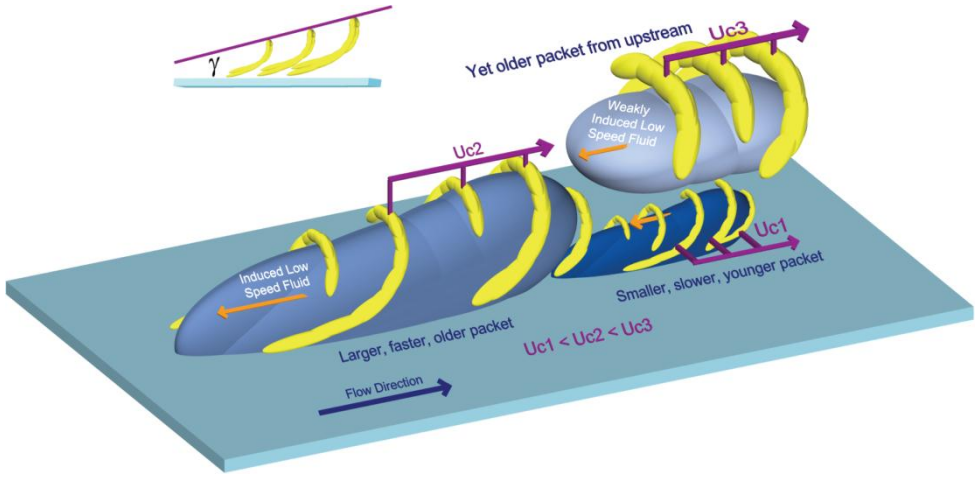

Figure 2.15: Conceptual scenario of nested hairpin packets close to the wall. The packets are aligned in streamwise direction and together form large zones of nearly uniform streamwise momentum. From Adrian et al. (2000).

3 Plasma and plasma actuators

Plasma is specified as the fourth state of matter. It is created by providing sufficient energy to a molecule, so that the gas becomes ionized. Hence resulting in a gas in which electrons, ions, and depending of the degree of ionization even neutral particles, can move freely. The energy for the ionization can come from a thermal or an electrical source. Based on the degree ionization a plasma can be referred to as either *hot*, if it is almost entirely ionized, or *cold*, if only weakly ionized.

After plasma is produced, it can be manipulated with electric and magnetic fields. In the presence of a produced electric field, the ionized air induces a body force vector field acting on the surrounding non-ionized gas. This body force makes plasma actuators promising for flow control applications. Furthermore, plasma actuators present an appealing method of active flow control, since they feature no moving parts, low mass, compactness, robustness, low power consumption, high actuation frequency and is easy to manufacture. They have already showed hopeful results for various applications, such as transition delay (Grundmann & Tropea 2007, Hanson et al. 2010), lift enhancement on airfoils (Corke et al. 2006), virtual flaps and slats for airfoil flow control (Corke et al. 2004), turbulent skin-friction drag reduction in a flat plate boundary layer (Roth et al. 1998,Sherman 1998 and Jukes et al. 2006), near-wake flow control (Artana et al. 2003), circular cylinder wake vortex control (McLaughlin et al. 2004), attenuation of flow-induced cavity noise (Huang & Zhang 2008), landing gear noise reduction (Thomas et al. 2005) and have also proven to be effective for boundary layer separation control. This has been shown at low *Re* on a flat plate by Goksel et al. (2006) and Sosa & Artana (2006), at moderate *Re* by Benard & Moreau (2011). They found that the plasma actuation accelerates the flow in the boundary layer and hence makes it more resilient to separation. Post & Corke (2003, 2004a, 2004b, 2004c) showed successful separation control on airfoils during dynamic stall at subsonic velocities by applying spanwise actuators at the leading edge. Furthermore, separation control has been effective on low pressure turbine blades (List et al. 2003, Hultgren & Ashpis 2003, Huang et al. 2006 and Ramakumar 2006, Suzen et al. 2007, Rizzetta & Visbal 2007 and Rivir 2007).

In the current work, plasma actuators are applied to control the low- and high speed streaks in a flat plate turbulent boundary layer, hence an overview of the plasma actuator and its working principle is provided in this section. These wall-normal jet producing plasma actuators can also be considered in future applications for suppression of vortex shedding, drag reduction and laminar-to-turbulent transition control.

3.1 DBD actuator

Over the years several types of plasma actuators have been developed, of which the atmospheric pressure corona discharges and dielectric barrier discharges (DBDs) are commonly applied for airflow control. These actuators consist of at least two electrodes mounted at the surface, between which a high voltage is applied, hence producing a cold plasma sheet. The alternating current (AC) DBD actuator has a significant advantage when compared to the direct current (DC) corona discharge actuator, in that the dielectric layer separating the electrodes results in a more stable discharge and a faster electric wind. Therefore the DBD actuator is selected for the current work.

The typical configuration of a single DBD actuator is presented in Figure 3.1. It is composed of two electrodes, one exposed to the flow and the other covered by a dielectric layer, which separates the electrodes. The exposed electrode is connected to a high AC voltage and the embedded electrode to the ground of a power supply. Typically, AC voltages of 5-20 kV are applied to the electrodes at frequencies of 1-30kHz. Although the voltage is very high, the system has a relatively low power consumption, due to the dielectric material

letting only a limited amount current through. The generated plasma region above the covered electrode is contained within an electric field, which induces a body force field, thereby adding momentum in the near-wall region of a boundary layer.

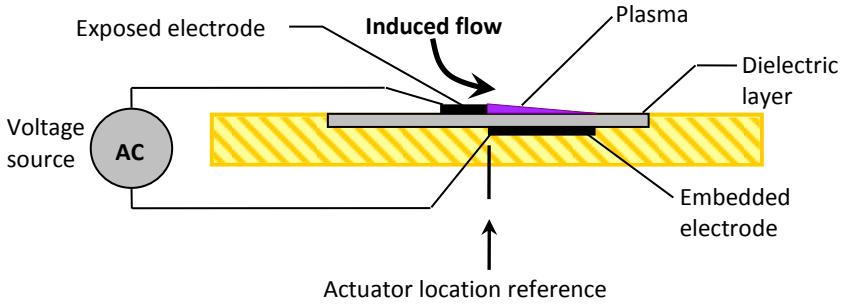

Figure 3.1: Schematic of a single DBD actuator, after Corke et al. (2010).

3.2 Plasma actuator physics

The description of the plasma actuator physics incorporates the discharge phenomena, plasma actuator cycle and induced electric wind, which are presented below.

3.2.1 Discharge phenomenon

The high voltage applied to the exposed electrode results in the production of an intense electric field. When the voltage is increased above the breakdown electric field, E_b, which is the value required to sustain electron-ion pairs in the gas in the absence of a space-charge field (Corke et al. 2009), the air around the bare electrode becomes ionized and plasma is created. Under influence of the electric field these electrons, which originate at the cathode, accelerate towards the anode and ionize the air by collisions with neutral gas molecules. The chemical reaction of the ionization is described by:

$$A + e^- \rightarrow A^+ + 2e^- \tag{3.1}$$

where A is a neutral particle and A^+ a positive ion. The multiplication of electrons will proceed along their path from the cathode to the anode, hence resulting in an avalanche and the creation of a discharge current (Moreau 2007). As the result of a series of discharges plasma is created, which appears as purple light, as is shown in Figure 3.2.

Figure 3.2: Actuated plasma actuator, displaying the purple light (Corke et al. 2010).

3.2.2 Plasma actuator cycle

The voltage applied to the exposed electrode is AC, hence the plasma generation can be divided in a negative and positive half-cycle. In the negative half-cycle the electrons are given up at bare electrode and drift towards the dielectric layer, where they accumulate locally. The build-up of charges at the dielectric surface opposes the applied voltage, hence reducing the local electric field strength, and thereby terminating the microdischarge at the dielectric unless the magnitude of the applied voltage is increased (Falkenstein and Coogan 1997). This self-limiting effect of the DBD prevents the occurrence of arc discharges to some degree. Such arc discharges could have a detrimental effect of the electronic equipment and more

specifically it could cause severe damage and possibly destroy the dielectric layer. During the positive half-cycle, the voltage is reversed and the electrons deposited on the dielectric surface return to the bare electrode. In Figure 3.3 a schematic of Enloe et al. (2004a) displays behavior of the electrons during both half-cycles.

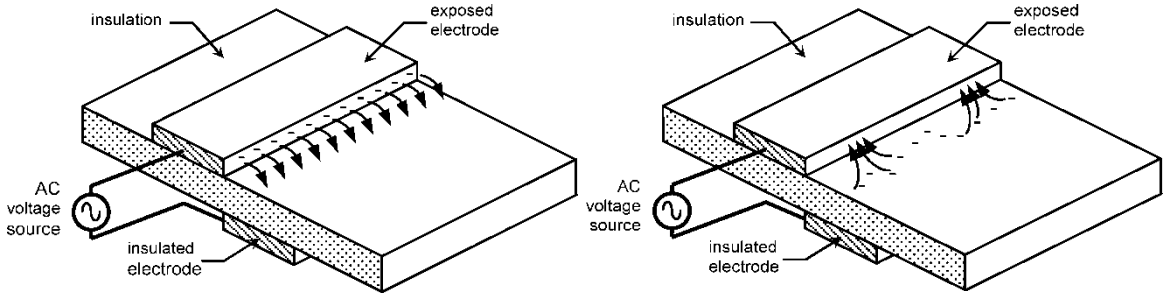

Figure 3.3: Schematic of the half-cycles. In the negative half-cycle the electrons emitted from the exposed electrode accumulate on the dielectric surface (on the left) and in the positive half-cycle return to the bare electrode (on the right).(Enloe et al. 2004a)

The structure of the plasma changes in both space and time. During the negative half-cycle uniform plasma can be observed with the unaided eye, which are actually series of individual filaments or microdischarges occurring in rapid sequence, with a relatively low charge transferred per event. Whereas during the positive half-cycle, the electrons do not come off as easily, thereby creating relatively few, but more intense microdischarges (Enloe et al. 2004b), as is shown is Figure 3.4. Increasing the peak-to-peak voltage or actuation frequency will allow the build-up of higher charges at the dielectric layer, hence producing more unstable discharges, creating more filaments and eventually arcs, which can destroy the dielectric layer.

(a)

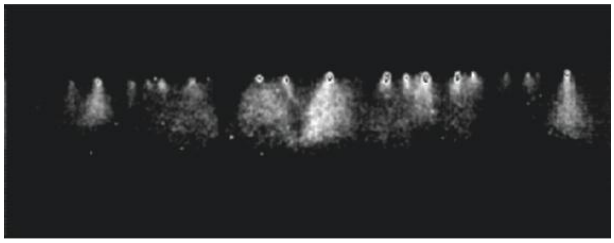

(b)

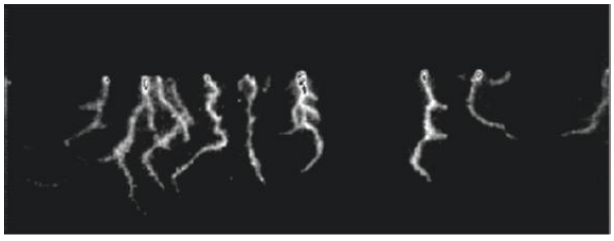

Figure 3.4: High-speed photographs showing individual microdischarges in **(a)** the negative and **(b)** positive half-cycle (Enloe et al. 2008). Note the exposed electrode is located at the top of the photographs.

Experiments on the temporal evolution of the net force production, indicates two interpretations for the half-cycles: the PUSH-push and PUSH-pull scenario, where the capitals indicate the relative magnitude of the force. Although there is still ongoing debate about these scenarios, more recent experiments (Enloe et al. 2009, Porter et al. 2007) indicate a PUSH-push, meaning that both half-cycles of the discharge add momentum to the flow in the same direction. Moreover, Boucinha et al. (2008) suggest the cycle can be separated into four parts.

In the first part of the negative half-cycle they observed a PUSH accelerating the flow, followed by a pull causing a mild deceleration in the second part. During both parts of the positive half-cycle a pull is exerted, thereby keeping the induced flow velocity constant.

3.2.3 Electric wind

As the electrons are accelerated to the anode, positive ions created in the ionization area, are repulsed towards the cathode by Coulombian forces. On their drift, the electrons and ions collide with neutral gas particles transferring momentum into the flow. However, since the ions are much heavier than the electrons, the momentum flux due to the electrons can be neglected. Hence, the overall momentum flux will be in the direction of the ion movement. These collisions are called Lorentzian collisions (Jayaraman et al. 2008), which create small body forces and thereby induce flow velocities above the surface of the electrodes. This induced movement of the gas, created by repulsion of the ions and the Lorentzian collisions, is called the electric wind (Robinson 1961). For boundary layer control purposes the maximum induced velocity and the induced velocity profiles are of importance. The velocity induced by the electric wind depends on the actuation and geometry design parameters, such as the actuation frequency (f_{ac}), peak-to-peak voltage (V_{pp}), waveform, exposed electrode thickness (t_{exp}), covered electrode width (w_{cov}), electrode gap (g), dielectric thickness (t) and dielectric properties.

3.3 Effects of parameters

The effects of voltage and actuation frequency on the velocity induced by the electric wind and the extent of the plasma, has been investigated by Orlov (2006). He observed the maximum extent increased linearly for increasing peak-to-peak voltage (V_{pp}), and that it was independent of the actuation frequency (f_{ac}). This effect is shown in Figure 3.5. Furthermore, the maximum velocity of the electric wind increased with the applied voltage, but also with the AC frequency, although the effect for increasing frequency is not nearly as strong. Boucinha et al. (2008) reported that for higher peak-to-peak voltages the plasma appears more uniform. They also explained further extension of the plasma enhances the induced ionic wind, thereby accelerating the flow at higher distances from the wall, leading to higher induced velocities.

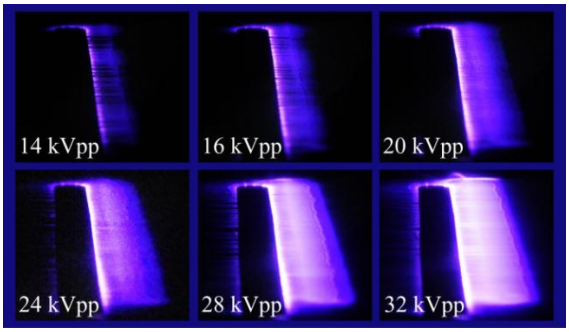

Figure 3.5: Photographs of Boucinha et al. (2008) displaying the effect of the peak-to-peak voltage on the plasma extent.

Enloe et al. (2004a), Roth and Dai (2006) and Forte et al. (2007) found the behavior of the velocity profiles at various voltages and frequencies are entirely different. An example illustrating the behavior of induced velocity profiles with voltage is presented in Figure 3.6. As can be seen, the peak of the maximum velocity drops from around a height of 1 mm at 12 kV to approximately 0.5 mm at 20 kV. For voltages up to 20 kV and at low frequencies of 300 to 700 Hz Pons et al. (2005) and Forte et al. (2007) indicate the peak of the maximum

induced velocity is located at approximately 0.5 mm from the wall. The last group optimized the performance of the single DBD actuator and reached induced velocities up to 8 m/s.

Measurements of Enloe et al. (2004a) at relatively low voltages indicated the thrust force produced by the actuator is proportional to $V_{ac}^{7/2}$. Post (2004) found the maximum induced velocity is also proportional to $V_{ac}^{7/2}$. They described that for increasing V_{pp} the maximum induced velocity was limited by the spanwise extent of the covered electrode. Hence, the area required to store the charge can be too small to gain the maximum effect of the applied voltage. Then the discharges are becoming unstable and filamentary, resulting in discharges losing a part of their mechanical effect. This behavior is illustrated in Figure 3.7, where the maximum induced velocity no longer increases as $V_{ac}^{7/2}$, and starts to asymptote.

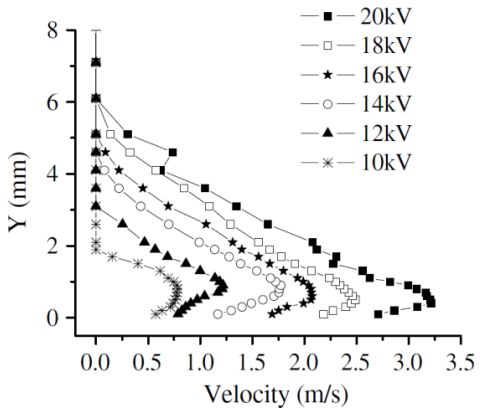

Figure 3.6: Induced velocity profiles for different applied voltages by Moreau (2007) in quiescent condition.

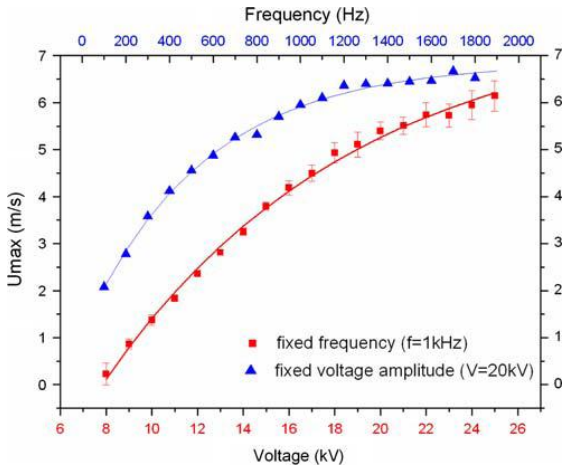

Figure 3.7: Evolution of the maximum induced velocity with voltage and frequency by Forte et al. (2007), where the induced velocities are reaching an asymptote.

The simulations of Orlov (2006) and Orlov et al. (2006) have indicated that for a specific actuator geometry there is an optimum AC frequency that depends on the actuator capacitance, at which the induced thrust is largest. However, the power consumption continues to increase monotonically with AC frequency. Implying the selection of the driving frequency is of importance for an optimum performance of the actuator. If the frequency is chosen too high (past the optimum), a lot of the power will be dissipated by heating of the air.

The optimum f_{ac} depends on the capacitance of the actuator, which is determined by the properties of the dielectric material. The capacitance is proportional ε/t, where ε is dielectric

coefficient and t the dielectric thickness. The power loss through the dielectric is proportional to $f_{ac}\varepsilon/t$, hence lowering the capacitance also reduces the power loss. A reduction of the capacitance would also allow the maximum body force to be produced at higher frequencies, and thereby increasing the maximum induced velocity. Hence, the general objective is to lower the capacitance (Corke et al. 2009).

Aside of the capacitance and the dielectric coefficient, the dielectric material has another significant property namely the breakdown voltage per thickness. This is an important property, since the minimum thickness of the dielectric needs to be enough to avoid break down at the applied voltage. Depending on the material this could be achieved within a fraction of a millimeter (0.05 mm is typical for Kapton)(Corke et al. 2010).

Besides the voltage and AC frequency also the AC waveform has a significant effect of the performance of the actuator. It can reduce the power consumption or enhance the induced electric wind. In Figure 3.8 several waveforms are illustrate, of these the square is the least efficient, but produces the largest induced velocity. The triangular is the most efficient, however it creates the weakest electric wind. The most common waveform is the sine wave, which has average power consumption and induced propagation velocity.

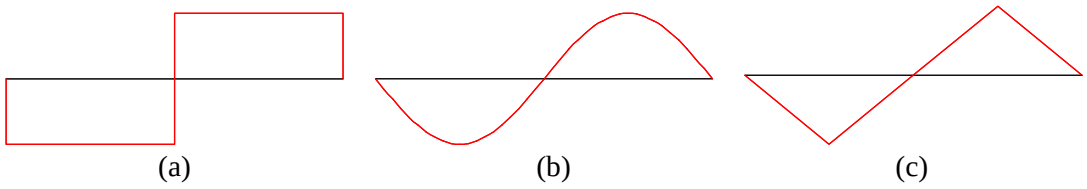

Figure 3.8: Several AC waveforms for plasma actuation. **(a)** Square wave, **(b)** sine wave and **(c)** triangular wave.

More recently experiments have been performed with repetitive nanosecond pulses, which can be used with both sinusoidal waveforms and DC components. The pulsed operation can produce significantly improved wall jets relative to those generated by a conventional sinusoidal waveform (Opaits et al. 2009).

As mentioned earlier, the area of the covered electrode, and thus its width, w_{cov} (see Figure 3.9), is an important factor for the maximum induced body force and velocity. However, the width of exposed electrode, w_{exp}, is not. It actually has a negligible effect on the performance. On the other hand, the thickness of the bare electrode, t_{exp}, considerably affects the induced flow, as has been shown by Enloe et al. (2004a). They compared flat copper electrodes of different thicknesses and concluded the thrust production is larger for thinner electrodes. They explained that a sharper edge concentrates the electric field lines, thereby locally increasing the electric field and hence the body force production.

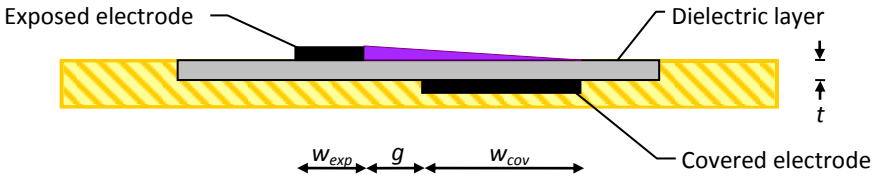

Figure 3.9: Schematic of a single DBD actuator indicating the electrode gap and widths.

The effect of the covered electrode width, w_{cov}, and gap spacing, g, on the maximum induced velocity for a single DBD actuator has been investigated by Forte et al. (2007). They observed the induced velocity increases with the covered electrode width until a plateau is reached, as displayed in Figure 3.10(a). The wider w_{cov} the further the plasma can extend. However, when the distance between the edges of the electrodes has become too large a

plateau is reached. Only increasing the voltage could yield further extension of the plasma in that situation.

The gap spacing is specified as positive when there is no overlap between electrodes. The covered electrode width is a significant factor for the gap spacing, thus the gap is to be normalized with w_{cov} for non-dimensionality. Figure 3.10(b) displays the maximum induced velocity against gap spacing for a covered electrode width of 5 mm. From the figure Forte et al. (2007) concluded that for $0 \leqslant g/w_{cov} \leqslant 2$ there is little effect on the maximum velocity, while for $g/w_{cov} \geqslant 2$ and $g/w_{cov} \leqslant 0$ the induced velocity drops off rapidly.

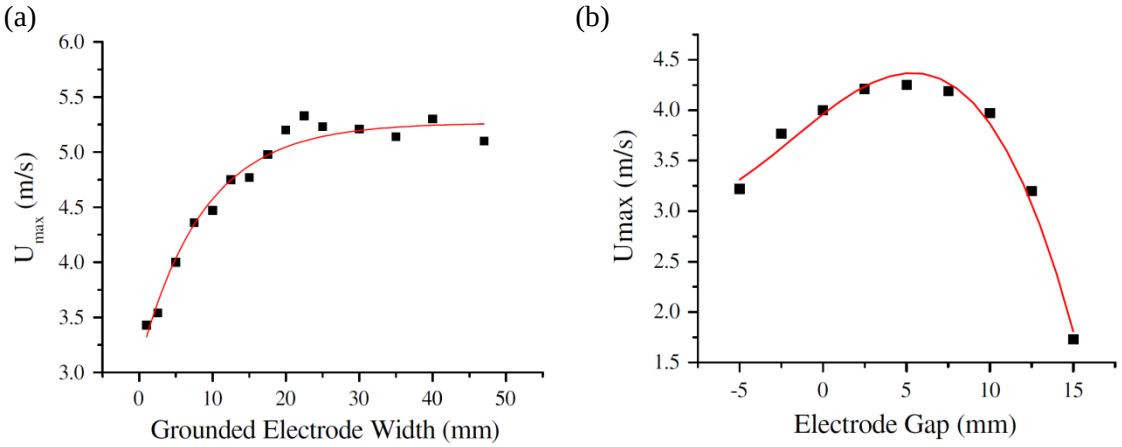

Figure 3.10: (a) Maximum induced velocity versus covered electrode width and **(b)** the maximum induced velocity versus gap spacing for a covered electrode width of 5 mm by Forte et al. (2007).

3.4 Example application: wall-normal jets by plasma actuators

A plasma actuator inducing a vertical jet is a geometrical variant of the plasma actuator, which produces a symmetric wall-normal jet and was first investigated by Santhanakrishnan et al. (2007a). They investigated a three-dimensional jet by using a dielectric barrier discharge actuator consisting of annular electrodes, as is shown in Figure 3.11. Later, Santhanakrishnan et al. (2009) studied a two-dimensional jet by using rectangular electrodes, one embedded electrode located between two exposed electrodes. A schematic of a linear plasma actuator producing wall-normal jets is presented in Figure 3.12. The bare electrodes are connected to a high voltage power supply and the embedded electrode to the ground. When actuated the plasma induces two opposing spanwise flows. Both flows meet at the middle of the covered electrode creating a stagnation point, from where the flows will be trusted upwards producing a wall-normal jet.

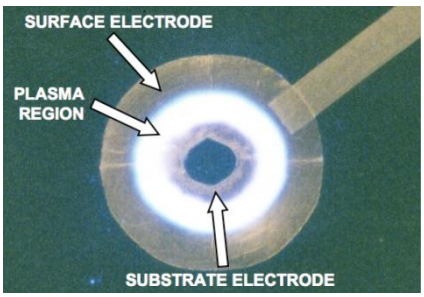

Figure 3.11: Photograph of annular plasma synthetic jet actuator by Santhanakrishnan et al. (2007b).

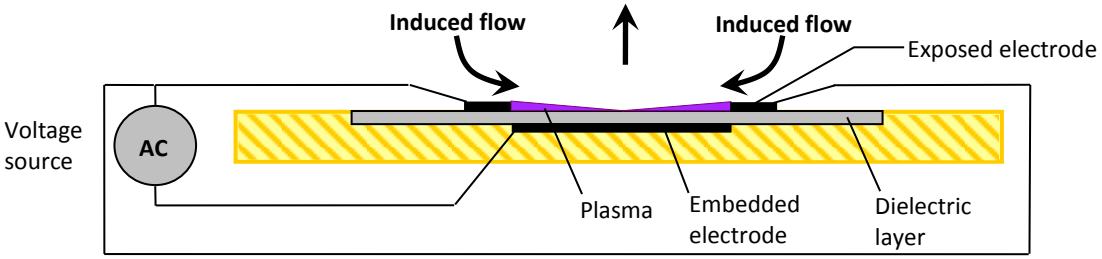

Figure 3.12: Schematic of a synthetic jet by DBD plasma actuators.

Benard et al. (2007) applied a slightly different configuration consisting of two embedded electrodes in between two exposed electrodes and two power supplies, in order to adjust the direction of the jet. A schematic of their configuration is shown in Figure 3.13. By changing the applied voltage to each exposed electrode separately, they were able to vector the jet. Furthermore, they optimized the actuator performance by investigating the effects of varying voltage. Moreover, they concluded the jet can be inclined up to around 20° without any loss in power.

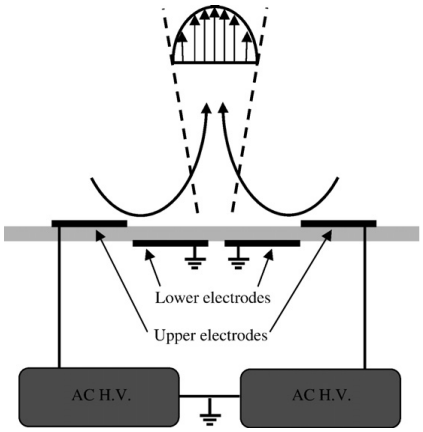

Figure 3.13: Schematic of the configuration used for creating an adjustable directional jet.

The streamwise arrangement of these wall-normal jet producing plasma actuators for the production of artificial streamwise vortices was first considered and tested by Roth et al. (2000). They successfully created arrays of streamwise vortices in a flat plate boundary layer.

Hanson et al. (2010) applied a feedback control system with an array of wall-normal jet inducing plasma actuators in a Blasius boundary layer that produced streamwise vorticity, which were to resemble disturbances caused by a roughness array. Their objective was attenuate streamwise vortices by creating relatively low amplitude disturbances, thereby reducing the transient growth instabilities and ultimately delay transition. They achieved up to 70% reduction of the disturbance energy within the boundary layer with this method.

Another aim for this actuator configuration is skin-friction reduction. For this purpose, Choi et al. (2011) performed experiments with DBD actuators in a turbulent boundary layer. By modifying the actuation of the electrodes they were able to induce spanwise oscillation and travelling waves. Their results showed different modifications to the near-wall structures for the different control techniques.

4 Experimental techniques

In order to determine the effectiveness of the plasma actuator in controlling the low- and high-speed streaks particle image velocimetry (PIV) has been applied. Furthermore, some diagnostic tools have been used on the PIV data, namely proper orthogonal decomposition (POD), the auto-correlation function and the power spectral density (PSD). These are applied to, respectively, examine the efficiency of the plasma actuation in achieving its purpose, determine the spanwise spacing between the coherent structures and establishing which frequencies within the flow contain have the highest intensity.

The first section of this chapter sets out the basics of PIV as used for the investigations in this thesis. For more details on the workings of PIV and its implementations readers are referred to Raffel et al. (2007). In the second section the data processing techniques: proper orthogonal decomposition, the power spectral density and auto-correlation function are described.

4.1 Particle Image Velocimetry

Particle image velocimetry (PIV) is successful measurement technique that over the past decades, due to advances in cameras, lasers and computer processing power, has developed from a qualitative to quantitative flow measurement technique. It is employed to acquire instantaneous measurements of the velocity and related properties of fluids in a two-dimensional plane with two-component PIV (2C-PIV (Willert et al. 1991)) or in three-dimensional space with tomographic PIV (Elsinga et al. 2006).

PIV measurement technique is based on the tracking of tracer particles within a fluid flow. A schematic overview of a 2C-PIV setup is depicted in Figure 4.1. A typical 2C-PIV system consists of a seeding system (not displayed) that intersperses small tracer particles into the flow, a laser system with laser optics to produce a laser-light sheet, and a digital imaging and recording system consisting of at least one camera with imaging optics.

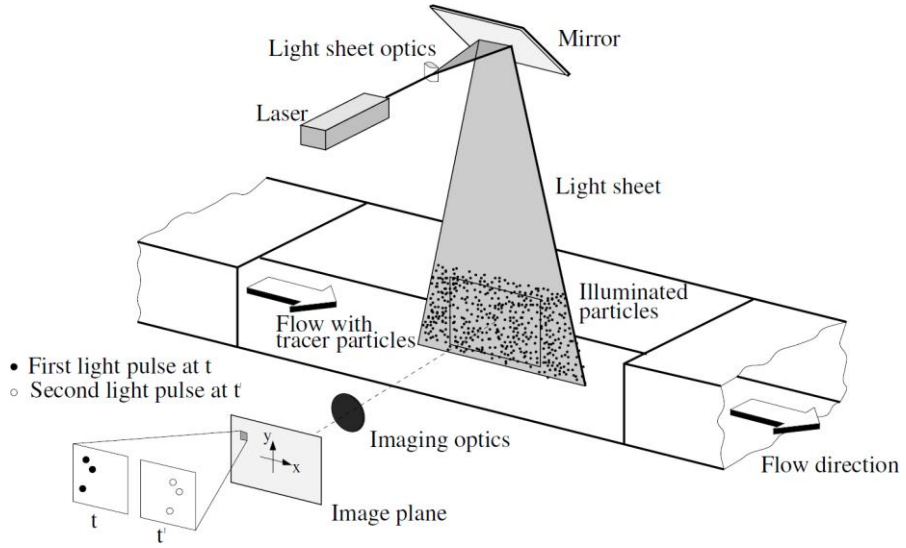

Figure 4.1: Schematic overview of a 2C-PIV setup by Raffel et al. (2007).

Tracer particles, which are often referred to as 'seeding', are introduced into the flow. These particles have to be sufficiently small, in order to follow the fluid flow accurately and

not alter the characteristics of the fluid. When moving through the region of interest, a pulsed light source will twice generate a thin light sheet, at a time-step Δt apart, thereby illuminating the tracer particles. Simultaneously with the laser pulses, a camera, placed perpendicular to the measurement plane, will record the light scattered by the particles in two subsequent image frames. The two image frames, $I(x,y,t)$ and $I'(x,y,t + \Delta t)$, will contain the specific particle positions.

For evaluation, the image plane is commonly divided into small sub-domains, called 'interrogation windows', as shown in Figure 4.2. Then cross-correlation of the interrogation windows of two subsequent recordings yields the average particle displacement in pixels within such a window, as is indicated in Figure 4.2. Evaluating the particle displacement with cross-correlation has the advantage that no explicit particle detection is required. By taking into account the magnification factor the displacement vector can be expressed in meters. Furthermore, by considering the time separation between the subsequent images, Δt, the velocity vector can be determined, and hence the velocity field can be reconstructed.

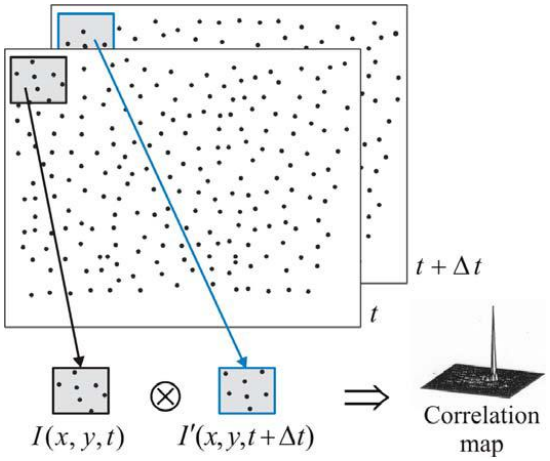

Figure 4.2: Image windowing and discrete cross-correlation map. Figure from Scarano (2007).

PIV can be considered non-intrusive as long as the tracer particles have no influence on the flow, follow the flow accurately and do not interact with each other (Westerweel 1997). Also the optical equipment can be placed outside of the flow field, although the laser and camera do require optical access to area of interest. Furthermore, PIV measures instantaneous velocity fields with a high spatial resolution, while most other velocity measurement techniques can only measure the instantaneous velocity at a single point, as for example hot wire anemometry (HWA) and laser doppler velocimetry (LDV). Even though the temporal resolution of PIV is increasing, it is still limited by the acquisition frequency and laser repetition rate. Additionally, the storage of the camera puts restrictions on the recording time.

4.1.1 Tracer particles

The tracer particles inserted into a fluid flow act as a tracking device and are typically employed with PIV or LDV. As described above, the particles are required to follow the flow accurately without altering the fluid flow characteristics. Consequently, the tracer particles characteristic response time has to be smaller than the smallest characteristic time scale of the fluid flow. Moreover, for the illuminated particles to be detectable by cameras, they should scatter enough light towards the camera.

Mechanical properties

For accurate PIV measurements, the tracer particles need to faithfully follow the motions of the flow. This can be achieved, by ensuring the velocity difference between the particles and the fluid is very small. The velocity difference or slipping velocity, illustrated in Figure 4.3, is $\mathbf{U_s} = \mathbf{U_p} - \mathbf{U_f}$, where $\mathbf{U_p}$ is the particle velocity vector and $\mathbf{U_f}$ is the fluid velocity vector.

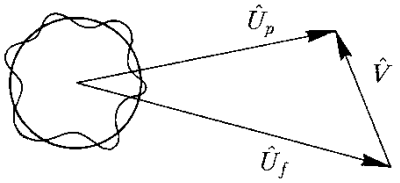

Figure 4.3: Relative particle motion. Figure from Melling (1997).

The entire motion of a small spherical particle immersed in a turbulent fluid flow is rather complex, but fortunately an acceptable approximation for the equation of motion is available from Hinze (1959). For very small tracer particles, as applied in PIV, the approximation of the equation of motion can be reduced to:

$$\frac{\pi}{6} d_p^3 \rho_p \frac{d\mathbf{U}_p}{dt} = \overbrace{-3\pi\mu d_p \mathbf{U}_s}^{\text{quasi steady viscous force}}, \tag{4.1}$$

where d_p is the particle diameter, ρ_p the particle density and μ the fluid dynamic viscosity (Scarano 2007). The term on the left and right hand side represent, respectively, the force required to accelerate a particular particle in the flow field and the quasi steady viscous force in the form of Stokes' drag.

Electrostatic effects

In equation (4.1) spherical particles are assumed, which is a valid assumption for small droplets and disperse solid particles of uniform size. There is also assumed that the external body forces on a particular particle are negligible. However, the ionization of fluid particles during the plasma actuation results in tracer particles getting charged by ion impact, at which point the electrostatic forces can affect the trajectory of the tracer particles. Hence, an electrostatic force needs to be added to the right hand side of equation (4.1). This force is determined by the maximum net charge level q_n that is obtained after a certain exposure time to the electric field and the electric field strength E_0.

$$F_{el} = q_n E_0 \tag{4.2}$$

Artana et al. (2002) found the maximum attainable net charge level q_n for droplets of hydrocarbon to be

$$q_n \approx 1.5\pi d_p^2 \varepsilon_0 E_0 \tag{4.3}$$

with ε_0 the Faraday constant. This equation shows the influence of electric forces becomes less when the seeding particle diameter is very small. Hence, these electrostatic forces will only be important if the slipping velocity is very low.

To approximate the electric field, a numerical calculation was performed by the use of an in-house model, which solves the electric potential Poisson equation. Details on modeling plasma actuators with the electric potential Poisson equation and the applied boundary conditions can be found in the paper by Suzen & Huang (2006). For the computation a dielectric coefficient of 3.4, peak-to-peak voltage of 14 kV and the plasma actuator configuration as applied during most of the experiments, with 1 mm width exposed electrodes and a 5 mm width covered electrode, was considered. More information about this configuration can be found in section 5.2. The resulting potential and electric field are

presented in Figure 4.4. Note that these are the maximum and not the average values occurring during an actuation cycle.

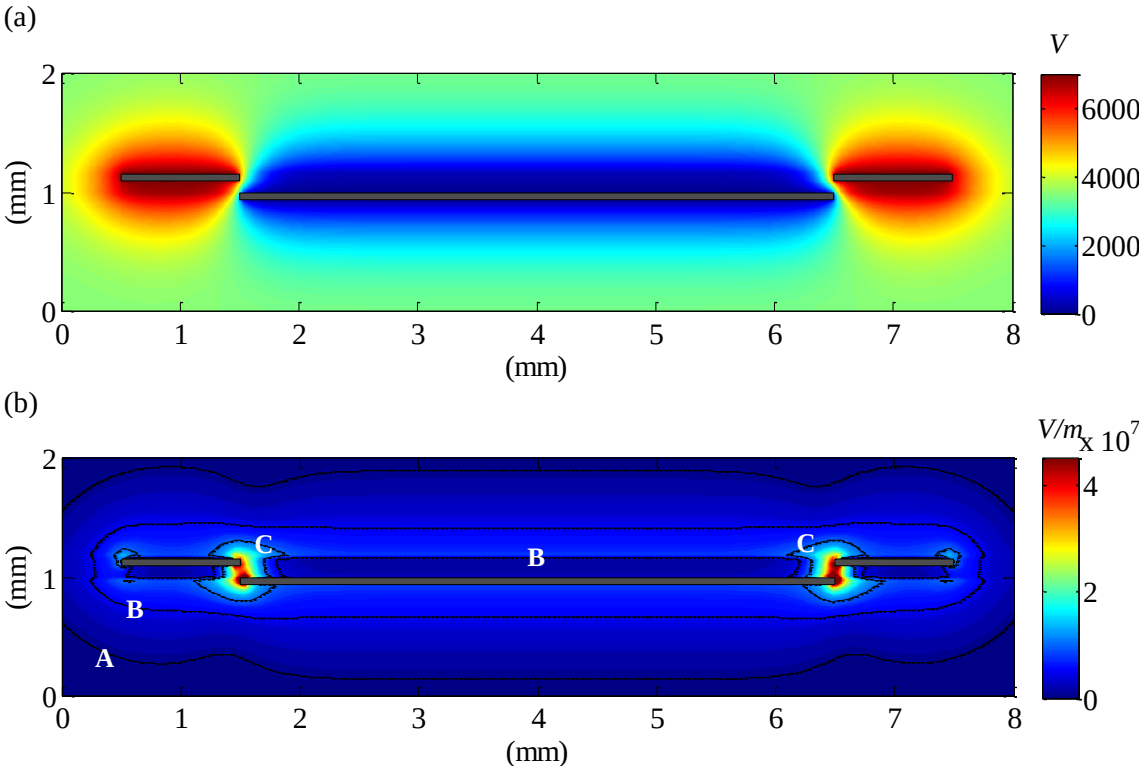

Figure 4.4: (a) Potential field and **(b)** electrical field resulting from the actuator configuration of the investigations, where 1 mm width exposed electrodes and 5 mm width covered electrodes were used. The plasma was actuated with a V_{pp} of 14 kV. The contour lines A, B and C indicates, respectively, $1 \cdot 10^6$, $5 \cdot 10^6$ and $1 \cdot 10^7$ V/m.

Artana et al. (2002) found that for a small particle of 1 μm the electrostatic force dominates the particle motion if the electric field is larger than 10^6 V/m. As can be observed in Figure 4.4(b) the electric field is considerably larger for up to 1 mm above the surface. However, more recently Stephen et al. (2011) studied the effect of seeding particles having a diameter of approximately 1 μm. They concluded that up to a peak-to-peak voltage of 20 kV the PIV velocity vector fields will not be significantly affected by electrostatic forces on the seeding.

Since the electrostatic forces can be neglected, the quasi steady viscous force (Stokes drag) dominates the right hand side of equation (4.1). Thus the equation of motion for the tracer particles can be reduced to

$$\frac{d\mathbf{U}_p}{dt} = \frac{\mathbf{U}_f - \mathbf{U}_p}{\tau_p}, \tag{4.4}$$

where τ_p is the characteristic particle response time or relaxation time which can be calculated from

$$\tau_p = d_p^2 \frac{\rho_p}{18\mu}. \tag{4.5}$$

The closely related particle Stokes number S_k,

$$S_k = \frac{\tau_p}{\tau_f}, \tag{4.6}$$

where τ_f is the characteristic flow time scale, indicates the accuracy with which the tracer particles can follow the fluid flow. It can be stated $S_k < 0.1$ is a practical limit, since the flow tracking errors are than below 1%. In the case of a turbulent boundary layer the characteristic flow time scale can be estimated by $\tau_f \approx \delta / U_\infty$, with δ the boundary layer thickness and U_∞ the free-stream velocity.

Scattering properties

Besides mechanical requirements the tracer particles also have to scatter enough light towards the camera to allow for particle tracking. The light scattering depends on several factors, such as the ratio of the refractive index of the particles to that of the surrounding medium, their size, shape and orientation. There is however little control over the last two factors, but the average size of the particles can be adapted, since that depends on the type of tracer particles. The larger the particle diameter the more light is scattered, in fact the average intensity increases with the square of the particle diameter. Moreover, the relative angle between the illuminating light and the camera axis plays a significant role. For spherical particles with diameters d_p larger than de wavelength λ of the laser light, Mie's scattering theory can be applied to determine the light scattering on a particle. Figure 4.5 displays the scattered light intensity distribution for an oil particle of 1 μm in air with laser light having a wavelength λ of 532 nm according to Mie's theory.

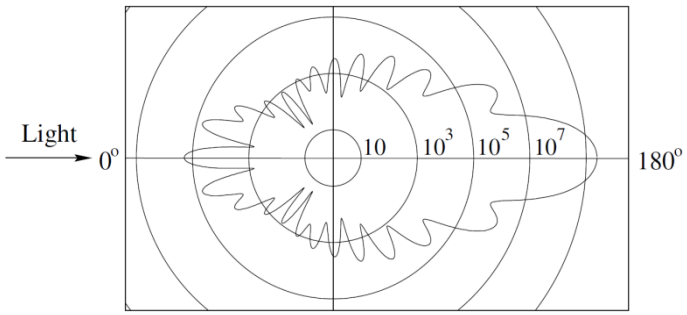

Figure 4.5: Distribution of the light intensity scattered by a 1 μm oil droplet particle in air by Raffel et al. (2007).

As can be observed, the intensity of the light scattered towards the camera can be improved by placing the camera in the so-called forward or backward scattering positions, as the intensity reaches a minimum near the 90°-angles.

From the above it can be concluded a trade-off has to be made for the chosen particle diameter, since it needs to small enough to follow the flow accurately, but at the same time the intensity of the light scattering towards the camera should be sufficient.

4.1.2 Illumination

For illumination of the tracer particles lasers are commonly used in PIV. This is because they emit monochromatic light with a high energy density, which can be easily bundled into thin light sheets. During the measurement the tracer particles are illuminated twice by a laser sheet produced by two laser pulses. These pulses need to have a very short duration to avoid the appearance of particle streaks on the camera. As a laser pulse leaves the laser head, it passes through a set of lenses and is deflected by mirrors before a thin light sheet is eventually obtained at the measurement location. The light intensity of this sheet needs to be sufficient for the tracer particles to be detected by the camera.

The typical arrangement of the lenses is a cylindrical lens, which expands the laser beam, followed by one or more spherical lenses that converge the laser beam, such that a thin laser sheet results.

4.1.3 Particle imaging

The image of the tracer particles in the light sheet is focused on an image sensor of the camera, the imaging plane, by using a photographic lens. The imaging system, which is usually a Charge Couple Device (CCD) or a Complementary Metal Oxide Semiconductor (CMOS) camera, is characterized by its focal length *f*, aperture number $f_\#$ and the image magnification *M*. The aperture number $f_\#$ is defined as *f*/*D*, where *D* is the aperture diameter. The image magnification is defined as

$$M = \frac{d_i}{d_o}, \tag{4.7}$$

where d_i is the image distance and d_o the object distance. The magnification factor can also be expressed as the ratio between the sensor size and the field of view (FOV). The focal length, image and object distance are related through the lens equation.

$$\frac{1}{f} = \frac{1}{d_i} + \frac{1}{d_o} \tag{4.8}$$

The applied aperture lenses are finite and therefore diffraction limited, which means that point sources will appear as Airy disks and rings on the image sensor. The size of such a disk d_{diff} can be approximated by

$$d_{diff} = 2.44 f_\# \lambda (M+1). \tag{4.9}$$

Then the minimal image particle diameter, as observed on the image sensor, is determined by

$$d_\tau = \sqrt{(M d_p)^2 + (d_{diff})^2}, \tag{4.10}$$

For small particles of $d_p \leq 1\mu m$ this minimal image particle diameter is typically dominated by the diffraction limit d_{diff}, although d_{diff} can be controlled to some extend with the aperture number $f_\#$.
Finally, the depth of the field δ_z can be approximated by

$$\delta_z = 2 f_\# d_{diff} (M+1)/M^2. \tag{4.11}$$

A significantly large aperture diameter is required to achieve sufficient light from all of the particles, and also to decrease the size of the diffraction pattern. However, a big aperture diameter decreases the depth of field, which is needed to have all the illuminated particles within the laser sheet in focus.

To accurately determine the velocity vectors from PIV measurements a proper choice of the seeding density and pulse separation is required. In order to achieve an error in the particle displacement of 1-2%, the pulse separation time has to be chosen, such that the particle displacement is approximately 10 pixels. Obtaining this pixel shift will result in a high number of particle pairs, meaning the majority of the images particles are located in the same window during both exposures. Thereby the particle displacement can be determined accurately from the correlation peak. Considerably smaller displacements may be too small to correctly establish the velocity vectors and with larger displacements too many particles will have moved out of the window.

As far as the seeding is concerned, the distribution should be uniform. Furthermore, according to Scarano (2007) there should be at least 10 tracer particles in an interrogation window. Lower seeding density would result in individual particle tracking, which would probably not be representative for the considered flow field. On the other hand a very high seeding density would make it difficult to distinguish the individual particles.

4.1.4 Image analysis

The image analysis yields particle displacement by applying cross-correlation between two subsequent images. However, the particle velocities are not uniform over the entire interrogation region. Hence the region is divided into smaller sub domains, called interrogation windows. The corresponding interrogation windows, at the first time instant t and second instant $t + \Delta t$, are then cross-correlated. After the cross-correlation procedure a cross-correlation map is obtained, where the correlation peak indicates the average particle displacement. This procedure is shown in Figure 4.2.

For a distinct peak the signal-to-noise ratio should be high. Too large particle diameter images will increase the noise level, due to mutually overlap of the particle diameter images, thereby decreasing the image contrast, as is presented in Figure 4.6(b). In the case the particle diameter image is smaller than one pixel, the particles will be pixel-locked and hence the determined displacement will be biased towards integer values (see Figure 4.6(a)). According to Raffel et al. (2007) the optimal particle image size is around 2 to 2.5 pixels.

Furthermore, large interrogation windows are desired because of the large number of image pairs in each window. However large windows result in poor spatial resolution. To solve this problem, while maintaining a high signal-to-noise ratio, a multi-pass iteration procedure can be applied, which repeats the correlation process for different window sizes. First the local average displacement is determined with a large window size, thereby providing an initial guess of the displacement vector, which can be used as an offset for the correlation windows in the second step. In this next iteration step smaller windows sizes can then be applied without losing the correlation peak.

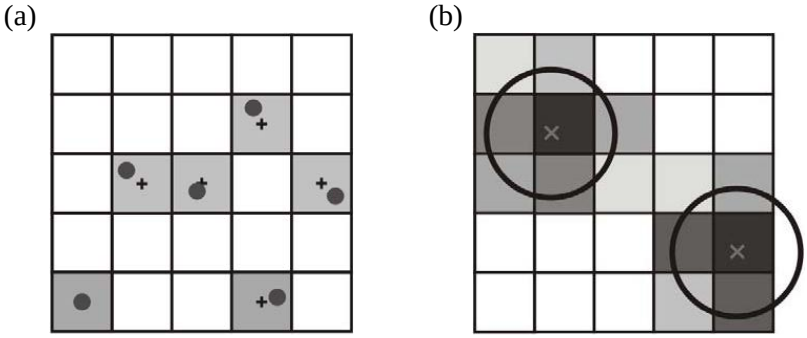

Figure 4.6: Effect of particle image diameter for windowing. **(a)** Pixel locking and **(b)** too large particle diameter images. Figure from Scarano (2007).

The quality of the cross-correlation can be further improved by enhancing the image quality. This can be accomplished by applying pre-processing procedures to raw images. A commonly used pre-processing operation is subtraction of the minimum of each pixel to remove spurious light, due to for example reflections. Moreover operations, such as multiplying by a constant and division by the average, are applied for normalization.

Also many post-processing procedures can be applied to further enhance the vector field. For an overview of these operations the interested reader is referred to Raffel et al. (2007).

4.2 Data reduction techniques

The velocity vector fields obtained from the PIV measurements can be processed with various techniques to retrieve additional information about the analyzed flow fields, such as proper orthogonal decomposition (POD), power spectral density (PSD) functions and auto-correlation functions.

4.2.1 Proper Orthogonal Decomposition

Proper orthogonal decomposition (POD) is technique that is commonly applied to extract the dominant flow structures, their dynamics and length scales. In the current work it is applied to depict the effectiveness in controlling the low- and high-speed streaks.

POD can be performed with two different approaches: the 'classical' method or 'snapshot' method. The 'snapshot' method has major advantage, since it reduces the computational resources required relative to the 'classical' method for the POD procedure (Sirovich 1987). Therefore the 'snapshot' method is applied in the current study and is described below. For detailed information on the 'direct' method the interested reader is referred to Cordier et al. (2011).

The basic principle of POD is to decompose, in this case the fluctuating velocity vector field data from PIV measurements, into a set of orthogonal spatial modes and the corresponding amplitudes. These modes represent the average spatial description of the structures of the structures containing most of the energy (Kostas et al. 2005). Although they do not necessarily have to correspond to structures, they can also be highly energetic events in the flow. Furthermore, POD reveals the energy contribution of the modes relative to the overall flow.

For the current work, the principle of 'snapshot' POD is to decompose the instantaneous fluctuations of the velocity vector fields into a limited number of orthonormal modes and the corresponding time-dependent amplitude coefficients. The fluctuating velocity fields $u'(\mathbf{x},t)$ are obtained by subtracting the mean $\bar{u}(\mathbf{x},t)$ from the instantaneous velocity fields $u(\mathbf{x},t)$, where $\mathbf{x}=(x,y)$. The objective of the POD analysis is to approximate the instantaneous velocity field by a finite sum of amplitude coefficients $a_j(t)$ and eigenmodes $\varphi_j(\mathbf{x})$.

$$u(\mathbf{x},t)=\bar{u}(\mathbf{x},t)+\sum_{j=1}^{J}a_j(t)\varphi_j(\mathbf{x}) \tag{4.12}$$

Here *J* is the number of modes used to reconstruct the velocity field.

The correlation matrix of instantaneous fluctuating velocity vector fields is given by

$$C_{i,j}=\frac{1}{N}\left(u'_i(\mathbf{x}),u'_j(\mathbf{x})\right), \tag{4.13}$$

where $(\cdot,\cdot)$ denotes the inner product and *N* is the number of instantaneous images. The correlation matrix is then diagonalized by applying singular value decomposition (SVD) yielding a diagonal matrix containing the eigenvalues λ_k and a matrix with the corresponding eigenvectors $\mathbf{V}_k$. Due to applying the SVD, the eigenvalues in the eigenvalue matrix are arranged in decreasing order: $\lambda_1\geq\lambda_2\geq\ldots\geq\lambda_N\geq 0$. These eigenvalues also indicate the energy contribution of the corresponding modes. The spatial modes $\varphi_j(\mathbf{x})$ are a linear combination of the eigenvectors and the fluctuations of the velocity vector fields, which can be defined as

$$\varphi_j(\mathbf{x})=\sum_{k=1}^{N}\mathbf{V}_k^j u'(\mathbf{x},t_k). \tag{4.14}$$

Normalizing these modes produces the normalized orthonormal basis functions

$$\psi^j(\mathbf{x})=\frac{\varphi^j(\mathbf{x})}{\left(\varphi^j(\mathbf{x}),\varphi^j(\mathbf{x})\right)^{\frac{1}{2}}}. \tag{4.15}$$

The amplitude coefficients $a_j(t)$ corresponding to the normalized modes are obtained with

$$a_j=\left(u'(\mathbf{x},t),\psi^j(\mathbf{x})\right). \tag{4.16}$$

Finally, the velocity field an instantaneous image or snapshot can be reconstructed with the selected number of modes by applying equation (4.12).

As mentioned above, the eigenvalues λ_k indicate the energy of each mode. Hence, the energy content of each mode relative to the total energy is determined by

$$E_k = \frac{\lambda_k}{\sum_{n=1}^{N} \lambda_n}. \tag{4.17}$$

4.2.2 Power spectral density

Applying PSD for the current time-resolved data requires the use of a discrete interpretation, which is usually performed with a Fast Fourier Transform (FFT). Similarly as for the POD analysis, the mean velocity field is first subtracted from the instantaneous velocity fields, hence obtaining the fluctuations of the instantaneous velocity fields. A line of these fluctuation fields is then selected as input for the PSD.

For calculating the power spectral density, the input signal is commonly divided into a number of segments that can be chosen to overlap and thereby improve the frequency resolution. Since rectangular windows can result in sharp peaks in one or several frequency bins, a windowing function is applied to avoid such peaks. For the current work a Hanning window is used, for details on the Hanning window and other windowing functions, interested readers are referred to Heinzel et al. (2002). Next the periodogram for each of the segments is determined with

$$P_k = \frac{1}{M} \sum_{m=0}^{M-1} \left| FFT_k(u'_m) \right|^2, \tag{4.18}$$

where n the instantaneous image number, N the signal length and k the segment number. Finally, the periodograms are averaged to obtain an approximation for the PSD of the signal.

4.2.3 Auto-correlation

The auto-correlation function is used to determine the spanwise spacing between the coherent structures (low- and high speed streaks). It is applied here to determine the similarity in the velocities along spanwise direction over time. For easy comparison the normalized form of the auto-correlation with zero shift, the correlation coefficient ρ_{zz}, is considered. This coefficient is limited to the range $-1 \leq \rho_{zz} \leq 1$.

To retrieve the desired auto-correlation functions the mean value of the mean velocity field was subtracted from the instantaneous images. Then spanwise lines from the resulting velocity fields were auto-correlated. Finally the average of the auto-correlation coefficients over time was determined, from which plots were produced, indicating the spanwise correlation of the streamwise velocity.

5 Experimental setup

An experimental investigation has been conducted to study the ability of the plasma actuators in controlling the low and high speed streaks within a turbulent boundary layer. The design and setup of these experiments are described in this chapter. In the first section the flow facility, flat plate model and flow conditions, are discussed. The plasma actuator apparatus and the investigated configurations are described in the subsequent section. In the third section the arrangement of the 2C-PIV experiments is depicted.

5.1 Flow setup

To investigate the possibility of the plasma actuators in controlling low- and high speed streaks, a test model is to be designed. A flat plate model is applied to develop a zero pressure gradient turbulent boundary layer. The specific details of the flat plate model, the flow facility used and the resulting flow conditions are discussed in this section.

5.1.1 Model characteristic parameters

The test model used to develop a turbulent boundary layer, as presented in Figure 5.1, is a 1.2 m long Plexiglas flat plate. The flat plate model has an elliptical leading edge, to prevent leading edge separation and a sharp symmetric trailing-edge to reduce pressure fluctuations, due to vortex shedding. The flat plate spans the entire width of the test section (400 mm) and was installed at zero angle-of-attack in the vertical center of the nozzle exit, to obtain a zero pressure gradient boundary layer. In order to have a uniform flow field at the measurement location, the leading edge is located 531 mm inside of the nozzle exit. A 15 mm strip with sparsely and evenly distributed carborundum particles of grain size 0.8 mm is placed 90 mm from the leading-edge to force a spanwise uniform boundary layer transition from laminar-to-turbulent. Furthermore, a cutout (398×198 mm^2) has been made, where interchangeable (glass or Plexiglas) plates can be inserted to simplify the changing of actuator configurations.

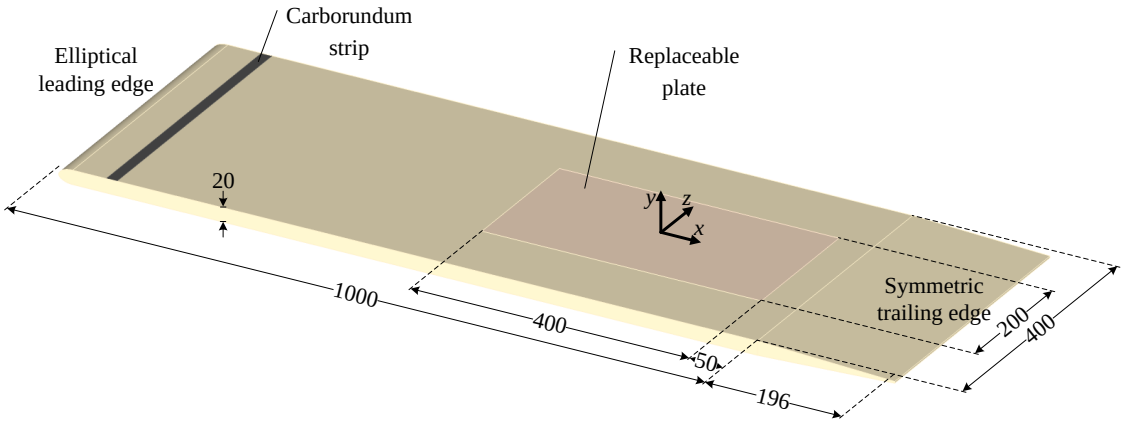

Figure 5.1: A schematic of the flat-plat used in the experiment, showing the cutout with the replaceable plate.

5.1.2 Flow facility

The experiments were conducted at the W-tunnel located at the High Speed Laboratory of Delft University of Technology. The W-tunnel is a low speed open-loop wind tunnel with an open test section (see Figure 5.2).

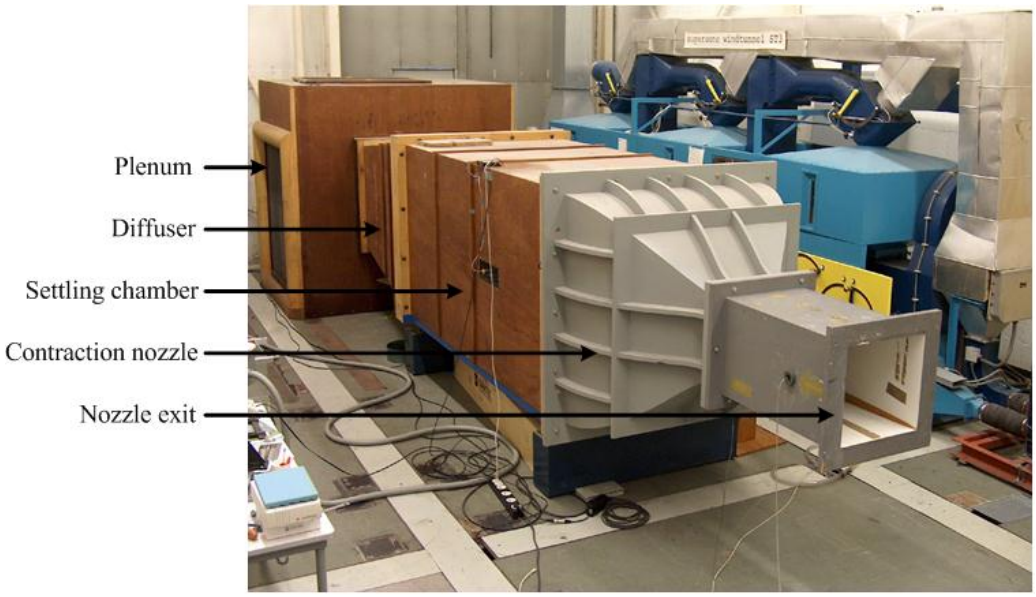

Figure 5.2: Low speed open-loop open-test section windtunnel (W-tunnel).

The air flows from the inlet of the tunnel, a plenum with dimensions 2.0×1.5×2.0 m^3, through a decelerating diffuser into the settling chamber. In the settling chamber, two grids reduce the turbulence intensity to $u'_{rms}/U_\infty < 0.2\%$. After the settling chamber, the flow is accelerated in the contraction nozzle and enters the test-section through the nozzle exit (0.4×0.4 m^2). From the flow flowing through the nozzle exit cross-section, only the central part (0.32×0.32 m^2) can be treated as uniform. The flow is driven by a pressure difference, created by a centrifugal fan, which is powered by a 16.5 kW DC electrical motor. For the measurements, the free-stream velocity at test section was determined with a pitot tube located within the central part.

5.1.3 Flow conditions

Most of experiments were conducted 750 mm downstream of the leading edge, the boundary layer parameters at this location are displayed in Table 5.1. The parameters have been obtained from 2C-PIV measurements, which were processed by averaging the cross-correlation maps of the recordings (Meinhart et al. 2000). Details of this PIV processing algorithm are discussed in section 5.3 on 2C-PIV. At a free-stream velocity of 7 m/s the boundary layer thickness δ_{99} is 16.1 mm. The displacement thickness δ^*, momentum thickness θ and shape factor H are 2.7 mm, 1.9 mm and 1.46. This shape factor shows the boundary layer is indeed turbulent, as for turbulent flat plate flows the value is typically around 1.3 and for laminar flows approximately 2.6 (Pope 2000). The friction velocity u_τ is 0.335 m/s and the viscous length δ_v is 44 μm. These parameters are defined in section 2.2.1. The corresponding viscous time scale $\tau_v = v/u_\tau^2$ is 131 μs. The Reynolds numbers at the measurement location were $Re_{\delta 99}$ = 76878, Re_θ = 894 and $Re_\tau = u_\tau\, \delta_{99}/v$ = 368. Besides the 7 m/s also free-stream velocities of 9, 11 and 13 m/s have been applied.

The evolution of the pressure coefficient $c_p = (p - p_{amb})/(\frac{1}{2}\rho_\infty U_\infty^2)$ at the free-stream in streamwise direction is presented in Figure 5.3, where p and p_{amb} are the static and ambient pressure, ρ_∞ the density and U_∞ the free-stream velocity. The pressure coefficient is calculated from the pressure measurements taken 51 mm above the plate outside the boundary layer.

From Figure 5.4 it can be seen the differences in static pressure relative the ambient pressure are considerably smaller than 1% in the measurement region. Hence the assumption of a zero pressure gradient flat plate boundary layer is valid.

Table 5.1: Boundary layer parameters

Parameter	units	
U_∞	m/s	7.0
δ_{99}	mm	16.1
δ^*	mm	2.7
θ	mm	1.9
H		1.46
u_τ	m/s	0.335
δ_v	µm	44
τ_v	µs	131
$Re_{\delta 99}$		76878
Re_θ		894
Re_τ		368

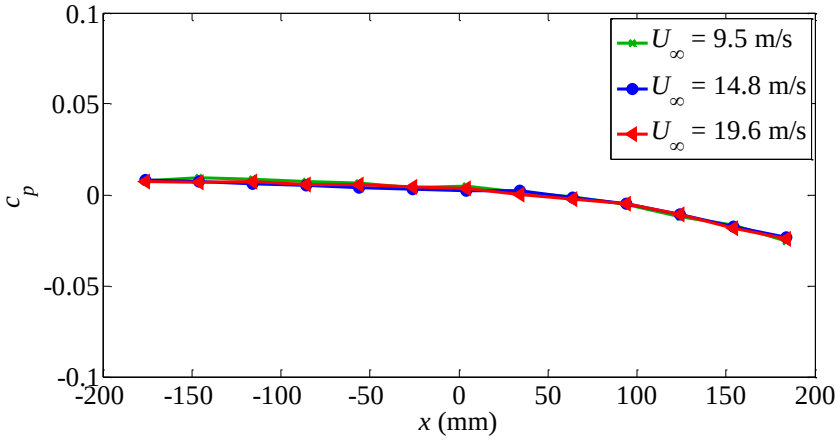

Figure 5.3: Evolution of the pressure coefficient in streamwise direction.

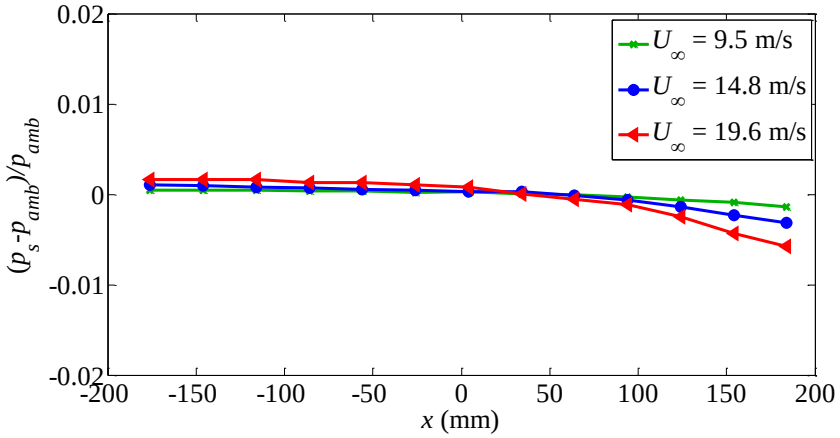

Figure 5.4: Evolution of the static pressure relative to the ambient pressure in streamwise direction.

The size of the smallest and largest turbulence scales in the near-wall region provide constraints for the design of the actuator and the measurement system. For statistical

measurements, the smallest coherent structures with a lifetime long enough to deliver a contribution, have a diameter of $20\delta_v$ (Stanislas et al. 2008) and a corresponding characteristic flow time scale of $20\tau_v$. For these experiments $20\delta_v$ and $20\tau_v$ are approximately 900 μm and 2.6 ms.

The largest coherent structures to be considered in the unaltered boundary layer are the low- and high speed streaks, which can extent 2000-3000δ_v in streamwise direction (Adrian 2007). Thus, the ratio of the largest to the smallest coherent structure W_{str} is about 150. Hence, the dynamic range of the measurement system has to satisfy this requirement (Herpin et al. 2008).

5.2 Plasma actuators

The plasma actuators were arranged in an array of streamwise pairs as shown in the schematic of Figure 5.5.

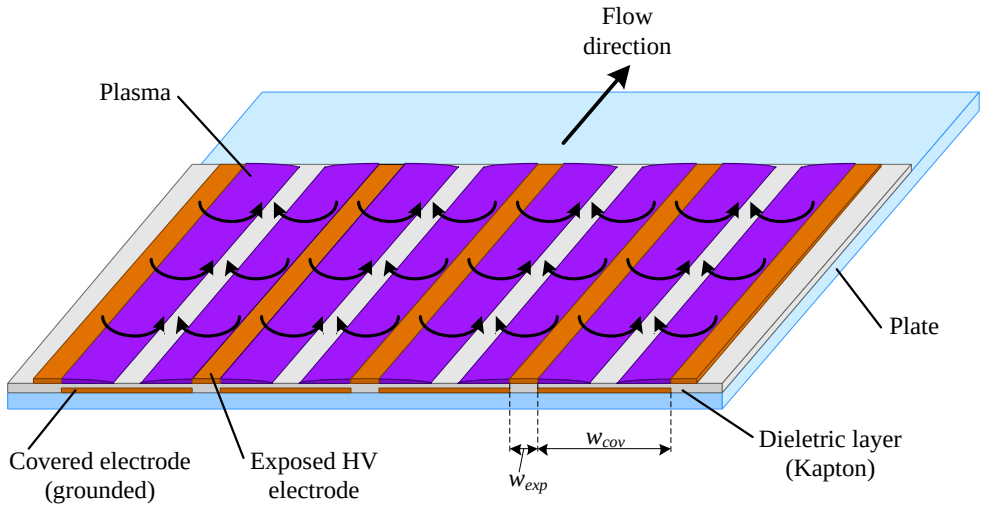

Figure 5.5: General schematic of actuator configurations.

The actuators were arranged in such a manner that they generate parallel wall-jets, which cause a spanwise-periodic array of streamwise vortices (Hanson et al. 2010). Each array consisted of five exposed electrodes and four covered electrodes. The center of the actuator arrays was located approximately 750 mm downstream of the leading edge. The actuators were manufactured from self-adhesive copper tape with a thickness of 60 μm (including the adhesive tape). The effective length of the electrodes, the length along which the plasma was created, was 150 mm. All other parts of the electrodes were covered with Kapton tape to prevent the creation of plasma. Three different actuators with embedded electrode width of 3, 5 and 7 mm were considered. The width of the exposed electrodes was 1 mm and the gap width was zero. From literature it is known the spanwise spacing of low-speed streaks is about 100 ± $20\delta_v$, which in the current boundary layer amounts to 4.6 ±0.9 mm. The low-speed streaks produced by the plasma actuator arrays should be of similar spacing distances. Furthermore, there were manufacturing limitations, since all the electrodes were cut to their appropriate size manually, hence the smallest producible width was limited to 1 mm. The exposed and covered electrodes were separated by a dielectric layer consisting of three layers of Kapton tape, each of them having a thickness of 2 mil (50.8 μm). The arrays were surface mounted on a 398×198 mm glass plate, which was then placed into the cutout of the flat plate model. Two aluminum connectors connect the electrodes with the TREK 20/20C HV amplifier (±20 kV, ±20mA, 1000W, gain 2kV/V), the exposed electrodes are connected to the HV output cable and the connector of the covered electrodes are grounded.

The operation of the actuator array is controlled via a computer, which sends the driving signals to the amplifier via a Digital/Analog (D/A) converter. Direct readings of the output voltage and current are provided by the internal measurement devices.

Based on several initial tests it was determined that operating values around 500 Hz and a peak-to-peak voltage of 8 to 12 kV were appropriate. An overview of the tested actuator geometries and driving signals is shown in Appendix A in the Tables A.1-A.3.

5.3 Arrangement for PIV

The PIV measurements were performed at the low-speed, open test-section facility (W-tunnel) at free-stream velocities ranging from 7 to 13 m/s. The purpose of the 2C-PIV experiments is to characterize the turbulent boundary layer, obtain statistical data and power spectra of the flow with and without plasma actuation and visualize the induced flow by the plasma actuators without free-stream flow. The desired power spectra require time-resolved measurements, hence the use of a high-repetition rate PIV system.

In order to provide an insight into the 3D behavior of the induced flow three different viewing planes were considered for the PIV measurements. These are the streamwise spanwise plane, streamwise wall-normal plane (at two different spanwise locations) and a spanwise wall-normal plane, which are denoted by configurations A, B, C and D, respectively. A schematic indicating the measurements planes of the PIV experiments is shown in Figure 5.6. Photographs and a schematic overview of the PIV setup, with the camera viewing the streamwise spanwise plane are presented in, respectively, the Figures 5.7 and 5.8.

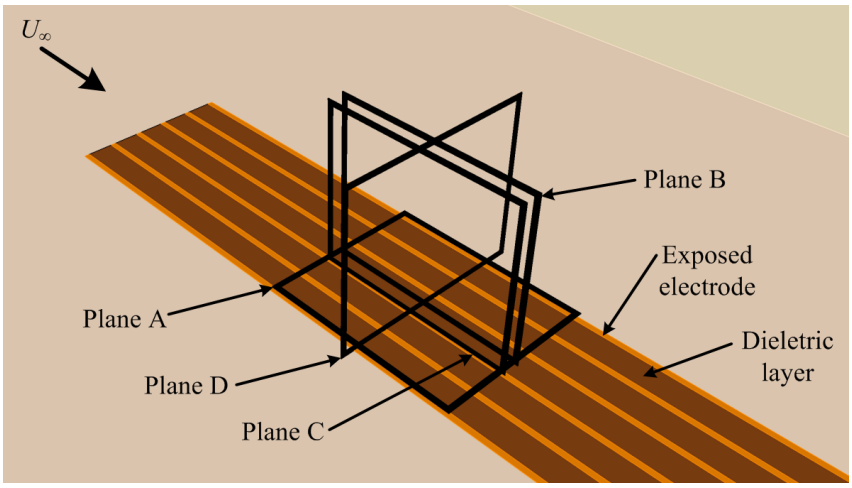

Figure 5.6: Schematic indicating the measurement planes of the PIV experiments.

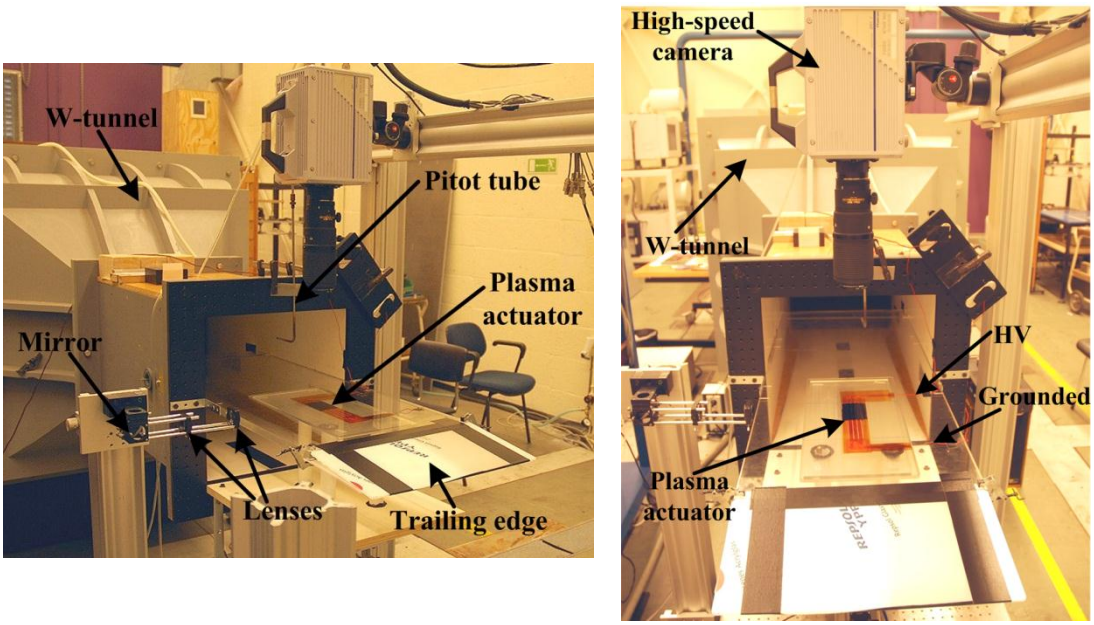

Figure 5.7: Photos of the PIV setup with the camera viewing the streamwise-spanwise plane.

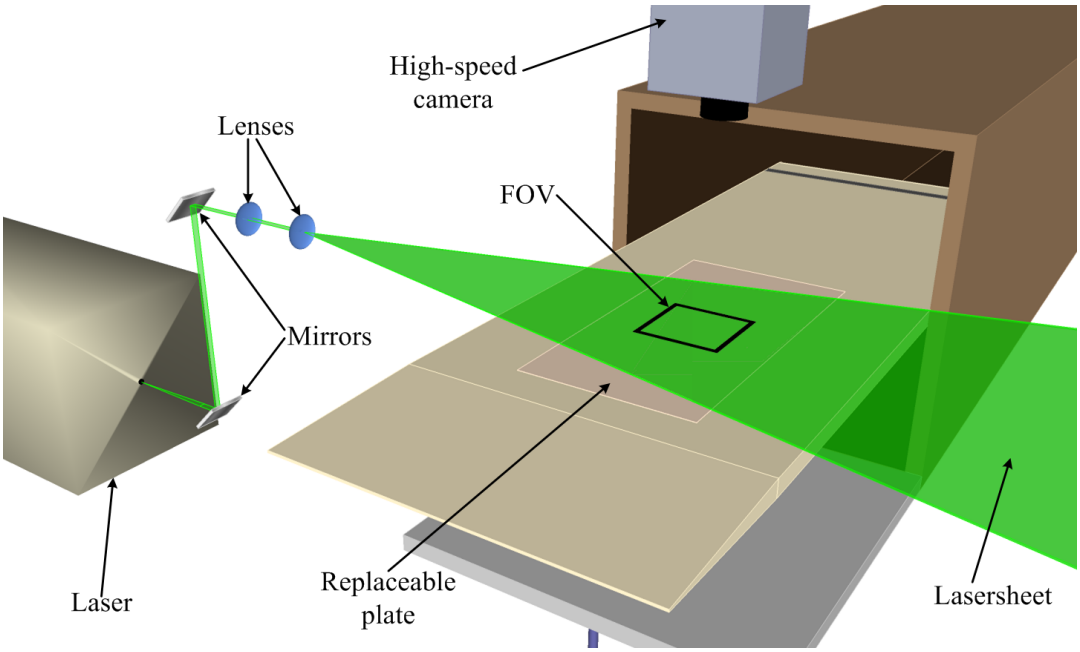

Figure 5.8: Schematic overview of the PIV setup with the camera viewing the streamwise-spanwise plane.

The flow seeding is achieved with a SAFEX smoke generator placed in the plenum of the windtunnel to obtain a uniform seeding at the exit nozzle. The non-toxic water-glycol based fog consists of 1 μm droplets and the density in liquid form is approximately 10^3 kg/m^3, hence the characteristic particle lag time defined in section (4.1.1) is $\tau_p = d_p^2 \frac{\rho_p}{18\mu} = 3\mu s$. The fidelity of the particles in following the flow expressed in the particle Stokes number is, $S_k = \frac{\tau_p}{\tau_f} = \frac{3 \cdot 10^{-6}}{131 \cdot 10^{-6}} = 0.02$, which satisfies the criterion of $S_k < 0.1$.

The illumination required for the PIV experiments is provided by a dual cavity, diode pumped, Neodymium-doped yttrium lithium fluoride (Nd:YLF) laser (Quantronix Darwin-

Duo 527-80-M), which emits visible green light of wavelength 527 nm at a maximum pulse frequency of 10 kHz. The average power output is 80W at 3 kHz, corresponding to an average pulse energy of 2·15 mJ. The beam diameter at the laser exit is 3 mm and pulse duration or pulse width is about 190 ns.

A laser sheet with a thickness of approximately 1 mm was created for all three setups by a combination of spherical and cylindrical lenses. In the case the spanwise wall-normal plane was being viewed, the laser sheet was illuminated in spanwise direction to reduce reflections.

The recording of the illuminated particles was accomplished with a high-speed camera, Photron Fastcam SA5, with a 12-bit CMOS sensor size of 1024×1024 px^2 and a pixel pitch of 20 μm. The camera was equipped with a Nikon objective of 200 mm focal length and the aperture setting was adapted to the conditions of each configuration.

The calibration of the PIV system consists of three parts. First the camera has to be focused on the illumination plane. In order to diminish bias-errors associated with pixel-locking (Westerweel 1997), the particles in the viewing plane had been slightly defocused to obtain a blur spot of approximately 2×2 pixels. Secondly, a dark image (without laser light) correction has been performed, to diminish camera noise. Finally, the image dimensions have to be determined.

The laser was operated via a high speed controller (LaVision), which was connected to the computer. From there both the laser and the camera were controlled via DaVis 8.0 (LaVision), which was used for both the image data acquisitioning and post-processing of the recordings. As a pre-processing step the minimum intensity of each pixel of an ensemble was subtracted, to reduce any bright spots due to surface reflections. Thereafter, the images were normalized by their time average.

The resulting images of the instantaneous velocity fields of the statistical recordings were processed with two different methods. The boundary layer velocity profiles and corresponding statistics were obtained by averaging the cross-correlation maps of an ensemble, to improve the convergence of the statistics (Meinhart et al. 2000). For the cross-correlation of these images a 6×6 pixel interrogation window (IA) and 75% overlap was used.

For the mean velocity fields and turbulent statistics multi-pass cross-correlation was applied. The first correlation was executed with a 64×64 pixel interrogation window and 50% overlap. For the second correlation a 16×16 pixel interrogation window with 75% overlap was used. The only exception is for the recorded images of the spanwise wall-normal viewing plane, where 12×12 windows with 75% overlap were applied.

The time-resolved recordings have been processed with the same settings as the mean velocity fields and turbulent statistics.

The recording parameters which are kept constant are displayed in Table 5.2. The specific parameters for each 2C-PIV configuration are shown in the Tables 5.3-5.6. The experimental matrices of the 2C-PIV measurements can be found in Appendix A.

Table 5.2: Constant recording parameters of the 2C-PIV setups

Recording medium	Photron Fastcam SA5
Recording lens	f = 200 mm
Illumination	Nd:YLF laser, 2·15 mJ per pulse at 3 kHz
Focal length of lasersheet lens 1, f_1	-40 mm (cylindrical)
Focal length of lasersheet lens 2, f_2	+200 mm (spherical)
Lasersheet thickness	1 mm
Seeding material	Non-toxic water-glycol based fog ($d_p \approx 1$ μm)

Configuration A: Setup for streamwise spanwise viewing plane

A lasersheet of 1 mm thickness was created approximately 0.3 mm above the surface of the plate, by using a -40 mm cylindrical and +200 mm spherical lens. The camera was positioned above the plate with the field of view (FOV) being at the middle of the actuator and its objective was set to an aperture of *f*/4. The magnification M was 0.91. Some additional recordings were made with the FOV being at the start and at the end of the actuator, where height of the lasersheet was 0.5 mm.

The 2C-PIV measurements were conducted with the double frame recording method at acquisition frequencies of 25 and 6000 Hz. The ensembles at 25 and 6000 Hz contain, respectively, 2000 and 5907 recordings. The pulse delay was 50 μs at 7 m/s and was decreased for increasing free-stream velocity to 30 μs at 13 m/s, to maintain an approximately constant free-stream pixel displacement. For the statistical measurements at 25 Hz the full CMOS sensor of 1024×1024 px^2 was used, which corresponded to a FOV of 22.6×22.6 mm^2. Hence, the digital resolution was 45.3 px/mm. The parameters for this setup are displayed in Table 5.3.

Assuming, the smallest spatial variation to be resolved is twice the size of the interrogation area, the SDR can be defined as $L_{FOV}/(2L_{IA})$, where L_{FOV} and L_{IA} are the sizes of the FOV and the interrogation window (Herpin et al. 2008). The spatial dynamic range (SDR) of the vector fields is 32 for the statistical measurements, and 22 and 28 for the time-resolved measurements. The large magnification gives a detailed view of the low- and high speed streaks in the near wall region of the turbulent boundary layer and hence covers the desired structures of interest. The SDR of this setup compared to the considered flow field equals the ratio SDR/W_{str}, which is 0.21 for the statistics and 0.15-0.19 for the TR-recordings.

Table 5.3: Parameters of the 2C-PIV setup for the streamwise spanwise plane

U_∞	7 m/s	9 m/s	11 m/s	13 m/s	7 m/s	
Aperture, $f_\#$	f/4				f/4	
Repetition rate	25 Hz				6000 Hz	
Recording method	double frame				double frame	
Pulse delay	50 μs	39 μs	32 μs	30 μs	50 μs	
FOV ($x \times y$)	1024×1024 px^2 22.6×22.6 mm^2				704×688 px^2 15.5×15.2 mm^2	896×512 px^2 19.8×11.3 mm^2
Digital resolution	45.3 px/mm				45.3 px/mm	
M	0.91				0.91	
IA	16×16 px^2 0.35×0.35 mm^2				16×16 px^2 0.35×0.35 mm^2	
IA overlap	75%				75%	
Vectors per field	256×256				176×147	224×128
SDR	32×32				22×22	28×16

Configuration B: Setup for streamwise wall-normal viewing plane at the middle of an covered electrode

For this configuration the lasersheet was created in the streamwise wall-normal plane with the spanwise location at the middle of a covered electrode (the theoretical location of the induced low-speed streak). During the measurements the velocity was kept at 7 m/s, the aperture was set to f/5.6 and the magnification was 0.90.

At acquisition frequencies of 25 and 6000 Hz, respectively, 2500 and 6000 recordings were acquired with 40 μs pulse delay. For the statistical measurements at 25 Hz the full CMOS sensor of 1024×1024 px^2 was used, which corresponded to a field of view (FOV) of 22.7×22.7 mm^2. Hence, the digital resolution was 45.1 px/mm. The parameters for this setup are shown in Table 5.4.

The spatial dynamic range of the vector field retrieved from the sum of the correlation maps is 85. The relatively high SDR and magnification of this configuration, means it will capture the smallest and largest structures of interest, unfortunately only statistics can be obtained with this processing algorithm. The turbulent fluctuations within the boundary layer are retrieved from individual cross-correlation maps, yielding a maximum SDR of 32. The data of the time-resolved recordings has also been obtained from individual cross-correlation maps, resulting in a SDR of 16. Comparison with previous PIV experiments show the first value is relatively high (Herpin et al. 2008).

Table 5.4: Parameters of the 2C-PIV setup for the streamwise wall-normal plane at the at the middle of an covered electrode

U_∞	7 m/s		7 m/s
$f_\#$	f/5.6		f/5.6
Repetition rate	25 Hz		6000 Hz
Recording method	double frame		double frame
Pulse delay	40 μs		40 μs
FOV ($x \times y$)	1024×1024 px^2 22.7×22.7 mm^2		512×752 px^2 11.3×16.7 mm^2
Digital resolution	45.1 px/mm		45.1 px/mm
M	0.90		0.90
IA	6×6 px^2 0.13×0.13 mm^2	16×16 px^2 0.35×0.35 mm^2	16×16 px^2 0.35×0.35 mm^2
IA overlap	75%	75%	75%
Vectors per field	682×682	256×256	128×188
SDR	85×85	32×32	16×24

Configuration C: Setup for streamwise wall-normal viewing plane at the middle of an exposed electrode

The configuration is similar to the previous setup, only the lasersheet is now located at the middle of an exposed electrode (the theoretical location of the induced high-speed streak).. During the measurements the velocity was kept at 7 m/s, the aperture was set to f/8 and the magnification was 0.91.

The acquisition frequencies and pulse separation time are equal to those of configuration B. For the statistical measurements at 25 Hz the full CMOS sensor of 1024×1024 px^2 was used, which corresponded to a field of view (FOV) of 22.5×22.5 mm^2. Hence, the digital resolution was 45.5 px/mm. The parameters for this setup are shown in Table 5.5.

Again, the spatial dynamic range of the vector field retrieved from the sum of the correlation maps is 85. The relatively high SDR and magnification of this configuration, means it will capture the smallest and largest structures of interest, unfortunately only statistics can be obtained with this processing algorithm. The turbulent fluctuations within the

boundary layer are retrieved from individual cross-correlation maps, yielding a maximum SDR of 32. The data of the time-resolved recordings has also been obtained from individual cross-correlation maps, resulting in a SDR of 16. Comparison with previous PIV experiments show the first value is relatively high (Herpin et al. 2008).

Table 5.5: Parameters of the 2C-PIV setup for the streamwise wall-normal plane at the middle of an exposed electrode

U_∞	7 m/s		7 m/s
$f_\#$	f/8		f/8
Repetition rate	25 Hz		6000 Hz
Recording method	double frame		double frame
Pulse delay	40 μs		40 μs
FOV ($x \times y$)	1024×1024 px^2 22.5×22.5 mm^2		512×752 px^2 11.3×16.6 mm^2
Digital resolution	45.5 px/mm		45.5 px/mm
M	0.91		0.91
IA	6×6 px^2 0.13×0.13 mm^2	16×16 px^2 0.35×0.35 mm^2	16×16 px^2 0.35×0.35 mm^2
IA overlap	75%	75%	75%
Vectors per field	682×682	256×256	128×188
SDR	85×85	32×32	16×24

Configuration D: Setup for spanwise wall-normal viewing plane

The setup has the camera looking upstream, hence the FOV on the spanwise wall-normal plane. The aperture of the objective was set to f/8.

The velocity during the statistical measurements was 7 m/s and the recordings acquired with the double frame method at 25 Hz and a pulse delay of 120 μs. The time-resolved measurements at this measurement plane were conducted at no flow with the single frame method at 4000/5400 Hz. The image magnification was 0.57. For the statistical measurements at 25 Hz 1024×1024 px^2 of the CMOS sensor was used, which corresponded to a field of view (FOV) of 35.8×24.6 mm^2. Hence, the digital resolution was 28.6 px/mm. The parameters for this setup are presented in Table 5.6.

The spatial dynamic range for the recordings is 43. Comparison with previous PIV experiments show the value is relatively high (Herpin et al. 2008).

Table 5.6: Parameters of the 2C-PIV setup for the spanwise wall-normal plane

U_∞	7 m/s	0 m/s	
$f_\#$	f/8	f/8	
Repetition rate	25 Hz	4000 Hz	5400 Hz
Recording method	double frame	single frame	
Pulse delay	120 μs	-	
FOV ($x \times y$)	1024×704 px^2 35.8×24.6 mm^2	1024×1024 px^2 35.8×35.8 mm^2	1024×704 px^2 35.8×24.6 mm^2
Digital resolution	28.6 px/mm	28.6 px/mm	
M	0.57	0.57	
IA	12×12 px^2 0.56×0.56 mm^2	12×12 px^2 0.56×0.56 mm^2	
IA overlap	75%	75%	
Vectors per field	341×234	341×341	341×234
SDR	43×29	43×43	43×29

6 Plasma actuator without free-stream flow

In the present chapter, the results of the actuator array experiments without a free-stream flow will be discussed. The first section introduces the actuator array as applied in the experiments and explains its working principle. Section two describes the effect of the actuation parameters, peak-to-peak voltage and actuation frequency, on the induced wall-normal and spanwise jet velocities of the array without free-stream flow.

6.1 Working principle of the actuator array

Before the experiments can be discussed, the working principle of the plasma jet actuator array will be explained in more detail. For the principle of a single vertical jet actuator see section 3.4.

The arrangement of the plasma actuators, as presented in Figure 5.5, represents an array of single jet actuators. The schematic of its working principle is displayed in Figure 6.1. When actuated, the plasma on a covered electrode creates a body force, thereby accelerates the air along the surface. The air on the left of an exposed electrode is accelerated towards the left and on the right side towards the right. Near the middle of a covered electrode the opposite flows will collide, resulting in a stagnation point. At this point the airflow can only move in upward direction, creating a vertical jet. Due to the arrangement of the actuators, the airflow induced by the plasma produces a suction effect above the exposed electrodes.

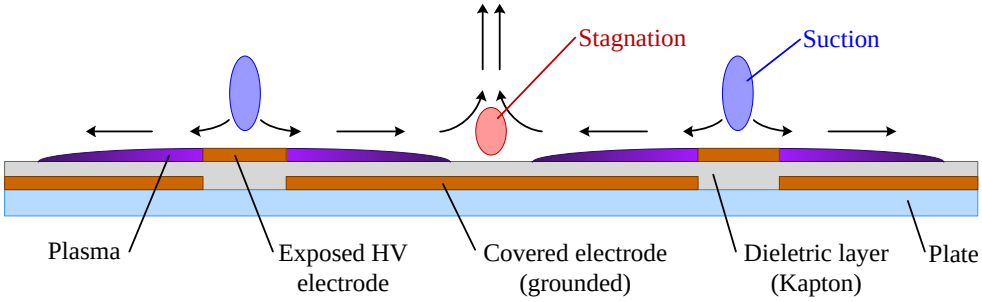

Figure 6.1: Schematic of the working principle for a plasma jet actuator array.

In Figure 6.2(a) an example of an instantaneous flow field during plasma actuation is displayed. It shows the opposing wall jets above the embedded electrodes and the wall-normal jets at the middle of covered electrodes. Furthermore, it can be seen the vertical jet on the left is tilted towards the right, due to the fact the flow in a room is never exactly zero. This tilting places the end of the wall-normal jet in a region where there is a flow of momentum towards the surface. The down flow completes the circulation and hence creates a counter rotating streamwise vortex. An example of the sliding average of 10 instantaneous images over time is presented in Figure 6.2(b), it shows the counter rotating streamwise vortices by streamlines.

Figure 6.3 represents an actuation cycle of one of the jet actuators, hence a description of the events in such a cycle can be described by looking at the instantaneous recordings. In each actuation period the actuators are actuated by applying voltage with a sine wave. During the first quarter of the cycle the voltage increases, introducing relatively large forces, which push the flow towards the middle of the images, as can be observed in Figure 6.3(a-c). Figure 6.3(b) shows the flow on the side is pushed with a greater force and slightly earlier than on

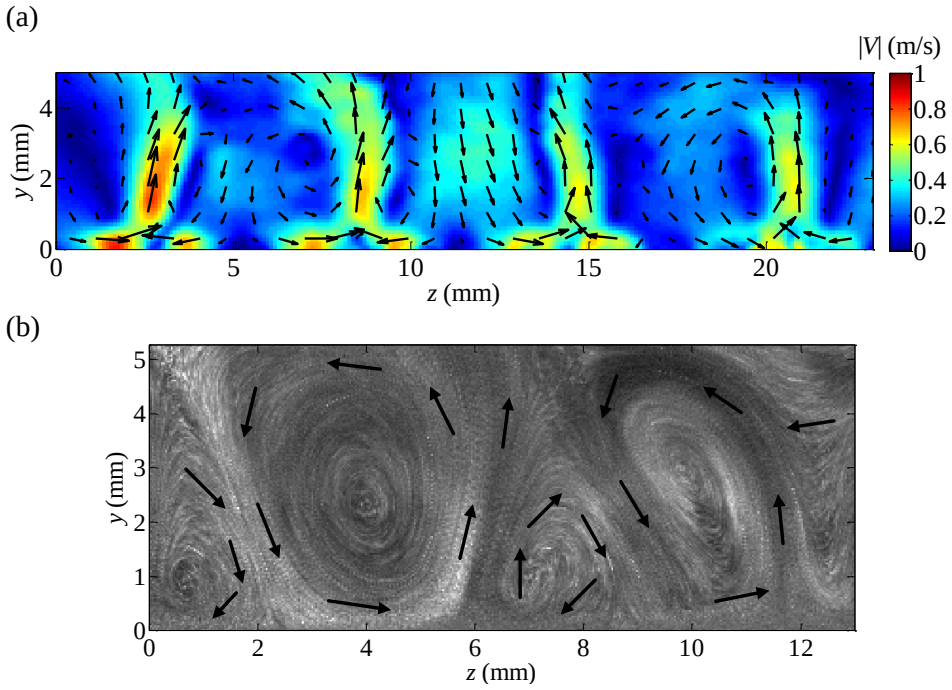

Figure 6.2: (a) Example of instantaneous flow field and **(b)** sliding average of 10 instantaneous images over time with plasma actuation at 10 kV and 500 Hz.

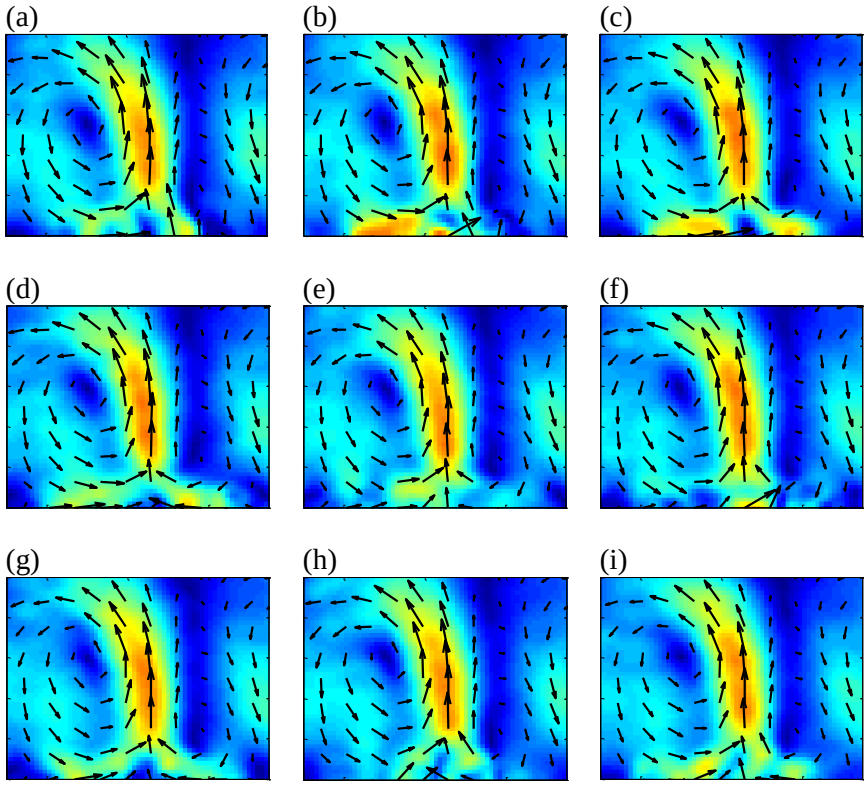

Figure 6.3: Single jet actuator of an array, while actuated with 10 kV at 500 Hz without free-stream flow. **(a-i)** One actuation period, with a step of Δt = 0.25 ms between each image.

the right. It also displays the vertical jet attaining a higher velocity, due to the movement in upward direction at the stagnation point. In the second part of the positive half-cycle the

spanwise jets reduce in strength Figure 6.3(d-e). At the beginning of the negative half cycle, a further reduction in strength is observed near the surface in Figure 6.3(f). In the middle of the negative cycle, Figure 6.3(g), a small pushing effect of the spanwise jets is visible, after which the flow reduces in strength again. Surprisingly the wall-normal jet maintains an almost constant strength throughout the entire actuation cycle.

6.2 Actuation parameters

This section discusses the velocities induced by the plasma actuator array for the different actuation parameters based on measurements of the mean velocity field.

The still air environment ensures the only momentum input is provided by the actuators. When the plasma actuators are actuated, the resulting flow accelerates from the initial still conditions to a quasi-steady state where it fluctuates around a mean value, due to the induced body forces and aerodynamic forces reaching an equilibrium. The quasi-steady state condition is reached rapidly, after which the recordings are started.

The experiments were conducted with a 5 mm covered and 1 mm exposed electrode width. For the steady plasma actuation a sine waveform with a 100% duty cycle was applied via the program Labview. The peak-to-peak voltage and driving frequency were varied. An overview of the applied voltages and frequencies is presented in Table 6.1.

Table 6.1: Plasma actuator configurations tested without free-stream flow

w_{cov}	w_{exp}	V_{pp}	f_{ac}
5 mm	1 mm	8 kV	500 Hz
5 mm	1 mm	10 kV	500 Hz
5 mm	1 mm	12 kV	500 Hz
5 mm	1 mm	14 kV	500 Hz
5 mm	1 mm	10 kV	1000 Hz

From the time-resolved recordings of the spanwise wall-normal plane, averages of the flow velocities in spanwise and wall-normal direction have been determined by subsampling with steps of 50 frames.

6.2.1 Peak-to-peak voltage

To see how the flow field changes for varying peak-to-peak voltages V_{pp}, experiments were executed and recorded at V_{pp} values ranging from 8 to 14 kV, while operating at a plasma actuation frequency f_{ac} of 500 Hz. The visualizations showing the mean flow of the recordings have been separated into the v and w velocity components along the y and z directions, which are presented in the Figures 6.4-6.5.

In Figure 6.4(a) the spanwise component at 8 kV is displayed, where the same contour levels are used as for the other cases. It shows considerably weak spanwise jets, reaching average velocities of approximately 0.1 m/s. The jets form at the surface in areas extending about 2 mm along the plate, based on the magnitude of the 0.02 m/s color lines. The plots of 10 and 12 kV show significantly stronger spanwise jets, attaining average velocities up to 0.4 m/s. The relative differences between these two are negligible. At 14 kV the attainable average spanwise velocities appear to drop to 0.3 m/s. Above 12 kV, either the power supply is unable to provide the required power quantity or the area above the covered electrodes have become saturated, which leads to discharges losing a part of their mechanical effect (see section 3.3). Consequently, the induced velocity of the spanwise jets reduce.

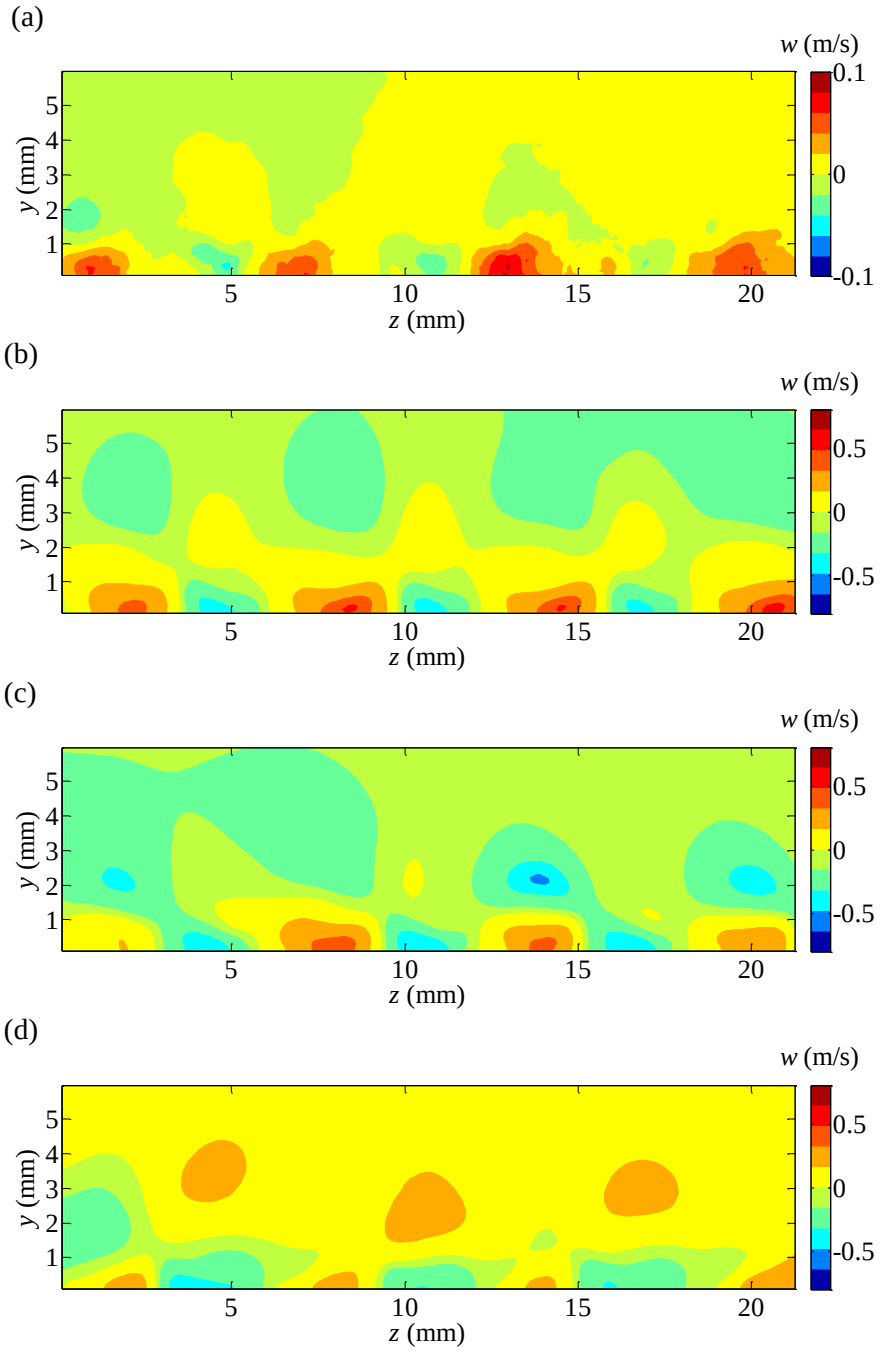

Figure 6.4: Average spanwise velocity without free-stream flow with plasma actuation at **(a)** 8 kV, **(b)** 10 kV, **(c)** 12 kV and **(d)** 14 kV and 500 Hz.

Similarly to the spanwise velocity fields, the mean velocity field of the vertical component at 8 kV also exhibits weak wall-normal jets, gaining velocities of less than 0.6 m/s. These jets stretch to a height of 4 mm and have a base width of 2 mm. At 10 and 12 kV the wall-normal jets extent 5 and 3 mm, respectively, in the upward and spanwise direction, when looking at the color lines of -0.2 and 0.2 m/s. Although of similar size, the attained velocities are almost 0.2 m/s for 10 kV and slightly more than that for 12 kV. Note that the regions with downward flow are narrower than the upward areas. To conserve momentum, the momentum flowing upward in the wider regions, have to be compensated by larger average downward velocities in the low-speed regions. When increasing the V_{pp} to 14 kV, a drop in the induced velocity is observed again. The height of the jet region has reduced to 4 mm and the width

remains 3 mm. As explained above, increasing the voltage beyond 14 kV leads to less powerful wall-normal jets.

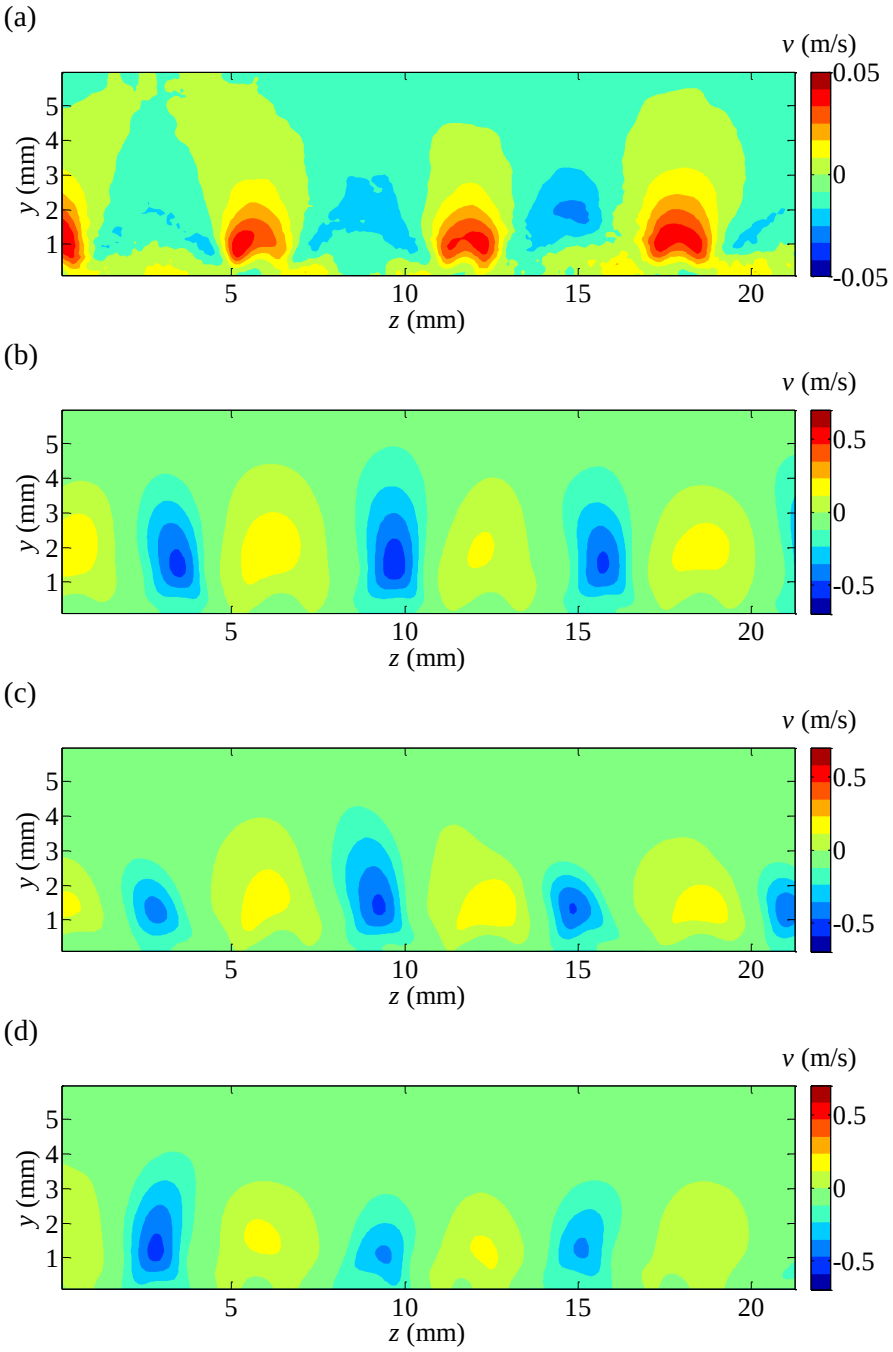

Figure 6.5: Average wall-normal velocity without free-stream flow with plasma actuation at **(a)** 8 kV, **(b)** 10 kV, **(c)** 12 kV and **(d)** 14 kV and 500 Hz.

6.2.2 Actuation frequency

In addition to the various peak-to-peak voltages, another recording was obtained with an increased frequency of 1000 Hz, while maintaining a V_{pp} of 10 kV. The mean flow fields of the spanwise and wall-normal velocity are shown in Figure 6.6.

The mean spanwise flow field, as presented in Figure 6.6(a), displays similar characteristics as the 10 and 12 kV plots at 500 Hz. The width of the jets is still about 2 mm and the visible structures have same shapes and sizes at roughly the same location. Only it

shows a significantly enhanced jet velocities. Where the actuators at 500 Hz were able to achieve velocities of 0.4 m/s, the current parameter settings allows average spanwise velocities of 0.7 m/s to be attained.

The increased velocities of the spanwise jets results in a similar effect for the wall-normal jets, as can be observed in Figure 6.6. Although flow features are still similar, enhanced flow velocities of the wall-normal jets, require even larger downward velocities in the low-speed regions to conserve the momentum. In the upward jets the average velocities exceed 0.3 m/s and the compensating downward flow reaches velocities surpassing 0.6 m/s.

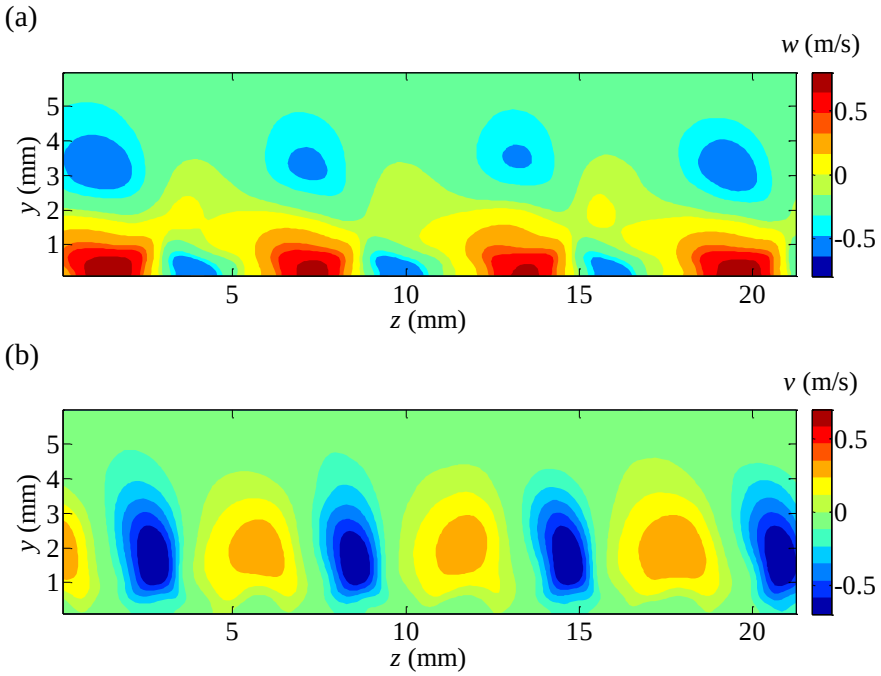

Figure 6.6: Average velocity fields of the velocity components with plasma actuation at 10 kV and 1000 Hz without free-stream flow. **(a)** Spanwise velocity field. **(b)** Wall-normal velocity field.

7 Plasma actuator in a turbulent boundary layer

This chapter discusses the results of the plasma jet actuator array experiments on a flat plate in a free-stream flow. In the first section the flat plate boundary layer is characterized. The following section provides the results and conclusions of the experiments at various measurement planes by discussing the mean velocity fields, mean velocity profiles, turbulent fluctuations, auto-correlations and power spectra during plasma actuation.

7.1 Characterization of the boundary layer

In this section the boundary layer is characterized by determining the statistical properties, from which the appropriate scaling parameters for the non-dimensional quantities are obtained. These statistical properties also serve as reference for future work.

The required statistical properties have been determined from two component PIV recordings. The recorded images were processed as described in section 5.3. The velocity profiles at the measurement location are presented in Figure 7.1. Due to reflections and weak illumination of the seeding particles near the plate surface, the velocities in the near-wall region were resolved poorly. However, in the viscous sublayer it is assumed the velocity profile is linear, hence the velocity profile in the near-wall region can be estimated by applying a linear least squares curve fit. The result is shown in the figure. In addition, the velocity in the log-law region can be compared to the logarithmic law of the wall (see section 2.2.1), as is shown in Figure 7.1(b). The measured velocity profile follows the law of the wall in the viscous sublayer and the log law, which confirms that the turbulent boundary layer is fully developed.

The boundary layer thickness δ_{99} is defined as the height at which $u = 0.99U_\infty$ and yielded 16.1 mm. The corresponding approximations of the displacement thickness δ^*, momentum thickness θ and shape factor H were 2.7 mm, 1.9 mm and 1.46. These parameters are defined by the equations (2.2), (2.3) and (2.4). For calculating the values a trapezoidal integration of the velocity profile, reconstructed with the viscous sublayer fit, was applied. The shape factor, which is typically around 1.3 for turbulent flows (Pope 2000), shows the flow is indeed turbulent. An overview of the boundary layer characteristic parameters is displayed in Table 7.1. For more details on the presented parameters see section 5.1.3.

Table 7.1: Boundary layer parameters

Parameter	units	
U_∞	m/s	7.0
δ_{99}	mm	16.1
δ^*	mm	2.7
θ	mm	1.9
H		1.46
u_τ	m/s	0.335
δ_v	µm	44
τ_v	µs	131
$Re_{\delta 99}$		76878
Re_θ		894
Re_τ		368

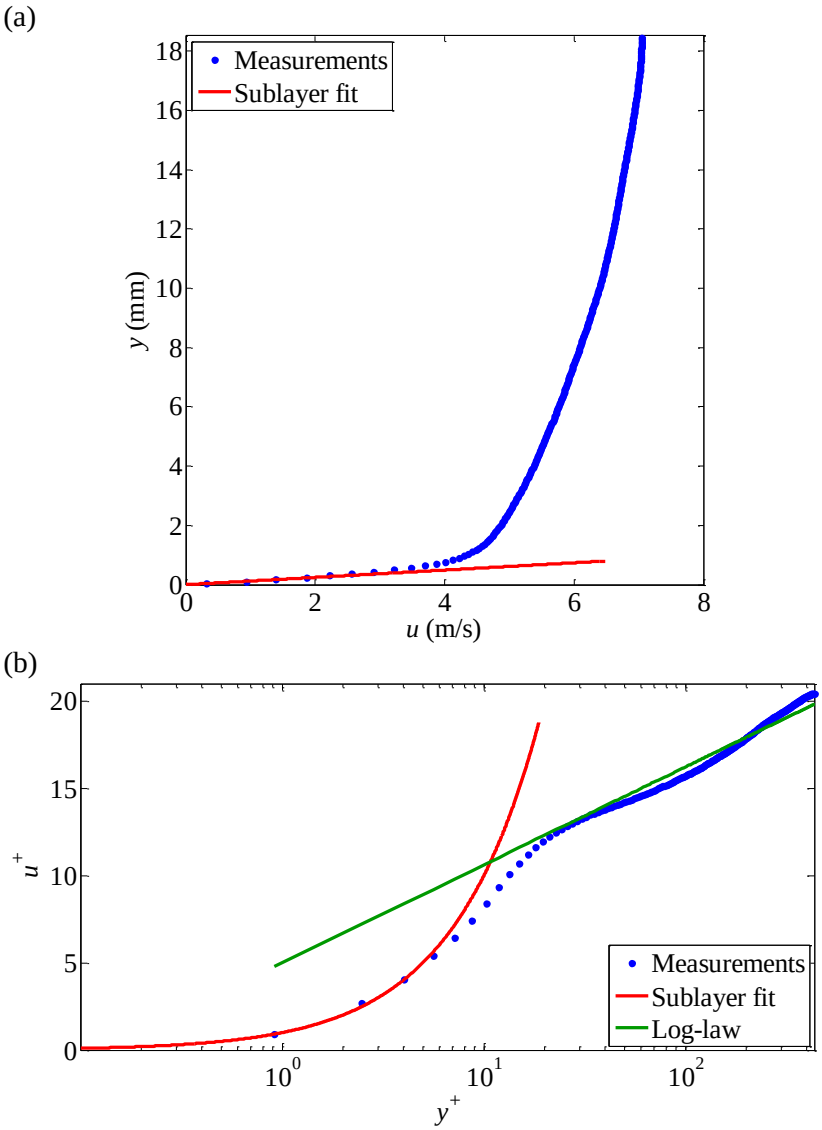

Figure 7.1: Boundary layer velocity profiles showing the measured values and the fittings on **(a)** a linear scale and **(b)** a semi-log scale.

7.2 Turbulent boundary layer with plasma actuation

The turbulent boundary layer has been characterized in the previous paragraph. Therefore the results of the experiments with plasma actuation can be discussed and compared. First the measurements at the streamwise wall-normal plane will be presented, followed by those of the streamwise-spanwise plane and finally the spanwise wall-normal plane.

7.2.1 Streamwise wall-normal plane

The measurements at the streamwise wall-normal viewing plane were located at two different locations. At first the laser sheet was positioned above middle of a covered electrode, where measurements were performed without and with plasma actuation. During the experiments with plasma actuation, the plasma was actuated with 8 or 10 kV and a 500 Hz actuation frequency. After the recordings at the covered electrode were stored, the laser sheet was repositioned above an exposed electrode, where recordings were obtained with the identical settings of the actuation parameters. For more details on the setup of the experiments and the applied settings see section 5.3 and Table A.2 in Appendix A.

The results of the recordings at the streamwise wall-normal plane are separated in three categories: the velocity profiles, the profiles of the turbulent fluctuations (second order terms) at the middle of a covered and exposed electrode.

Velocity profiles

The velocity profiles at the two electrode locations were retrieved with the sum of the correlation maps from the statistical recordings, to obtain the statistical profiles with a higher accuracy (Meinhart et al. 2000). The errors $\varepsilon_{\bar{u}}$ corresponding to profiles at the middle of the covered and exposed electrode are smaller than, respectively, 1.06×10^{-2} and 7.06×10^{-3} m/s. The resulting profiles above the middle of the covered electrode are presented in the Figure 7.3. Similar plots for above the exposed electrode are presented in the Figure 7.4.

As mentioned earlier the near-wall surfaces were resolved poorly, due to reflections and weak illumination of the seeding particles near the surface. Furthermore, the plasma actuation lead to the formation of regions with rather low particle density, as is illustrated in Figure 7.2. These regions were located just above the surface and had the largest extent just below the positions of vertical jets. Hence, the measurements at the exposed electrode were affected most by the plasma actuation.

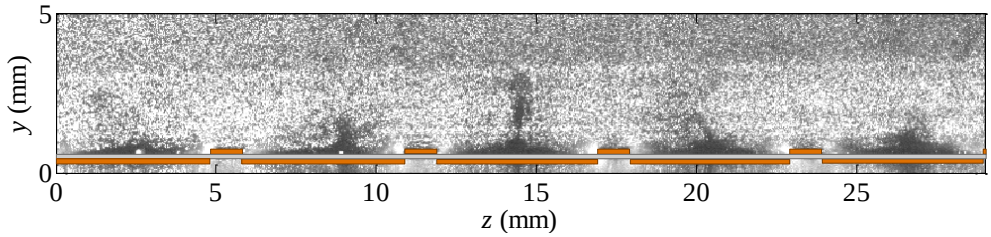

Figure 7.2: A recording displaying the illuminated particles during plasma actuation. Note the low particle seeding above the middle of the covered electrodes.

To retrieve the estimations of the actual velocity profiles near the wall, linear least square curve fitting procedures were performed in the viscous sublayer. The reconstructed velocity profiles at the exposed and covered electrode are visualized in, respectively, the Figures 7.3 and 7.4.

At the middle of the covered electrode the use of plasma actuation causes an increase in the velocity gradient near the surface. The increase can be appointed to the spanwise induced flows attaining there maximum velocities at a height of 0.5 mm, as can be observed in Figure 7.17. The spanwise flows carry with them a streamwise component of the free-stream flow, which has been pulled towards the plate surface. At the stagnation point the flow is pushed up again, causing initially an increase in the streamwise velocity between 0.5 and 1 mm. Above 1 mm, the faster streamwise flow is pushed upward resulting in a decrease of the streamwise velocity relative to the no plasma case. The plasma actuators effect in reducing the relative streamwise velocity extends from 1 to around 6 mm, after which the effect is negligible.

Thus, the velocities up to a height of 1 mm or $y^+ \approx 23$ are larger, due to plasma actuation and increase with voltage. The increase in the velocity gradient near the wall means a higher skin-friction at the plate surface. It should be noted the data points below a height of 0.2 mm have been left out of the dataset, since the instantaneous data displayed too many bad vectors within that region.

Note the 10 kV plasma actuation even shows a drop in velocity around a height of 2 mm. The drop is a consequence of the wall-normal jets reaching their maximum strength at a height of approximately 2 mm (see Figure 7.18).

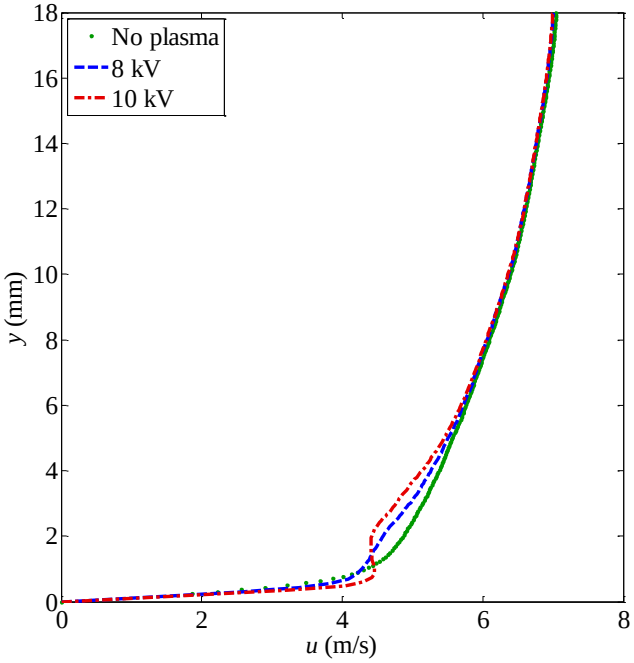

Figure 7.3: Boundary layer velocity profiles at the middle of the covered electrode for no plasma actuation and plasma actuation at 8 and 10 kV with 500 Hz.

In the Figure 7.4 the velocity profiles at the exposed electrode show a similar behavior as the profiles at the embedded electrode up to a height of 1 mm or $y^+ \approx 23$. Also here the velocity gradient is initially larger than the no plasma case and increases with voltage. Beyond the 1 mm height the profiles drop rapidly towards the normal velocity profile and reach slightly lower values between 2-6 mm.

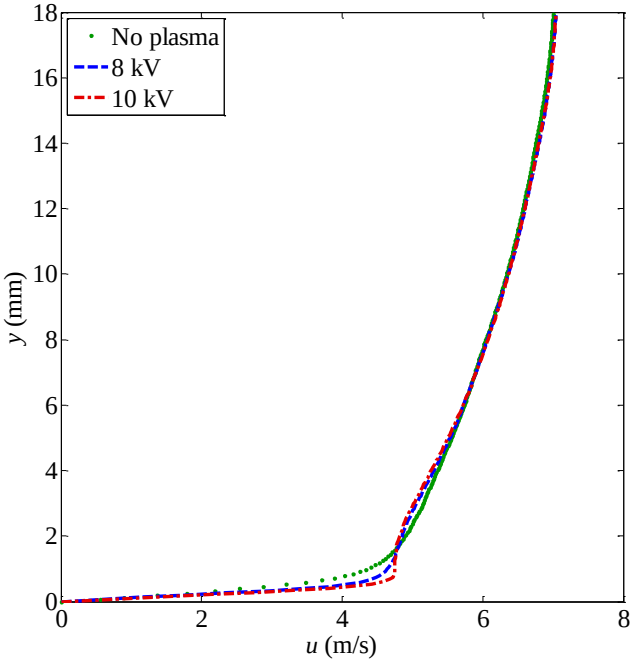

Figure 7.4: Boundary layer velocity profiles at the exposed electrode for no plasma actuation and plasma actuation at 8 and 10 kV with 500 Hz.

Turbulent fluctuations (or Reynolds stress profiles)

The turbulent fluctuations at the covered and exposed electrodes have been measured without and with plasma actuation. The graphs of these fluctuations at the covered and exposed electrode are displayed in Figures 7.5 and 7.6, respectively. The images in the figures denoted by (a), (b) and (c) are, respectively, without plasma actuation and with plasma actuation at 8 and 10 kV. The uncertainty associated with displayed profiles for $\langle u'^2 \rangle$, $\langle v'^2 \rangle$ and $\langle u'v' \rangle$ at the covered electrode normalized with U_∞ are 1.98×10^{-4}, 9.52×10^{-5} and 2.66×10^{-4} m/s and at the exposed 5.71×10^{-5}, 1.39×10^{-5} and 5.18×10^{-5} m/s.

The graphs of the turbulent fluctuations without plasma actuations show the typical behavior of $\langle u'^2 \rangle$, $\langle v'^2 \rangle$ and $\langle u'v' \rangle$ within a zero pressure gradient boundary layer (Klebanoff 1955 and Wu 2009). By applying the plasma actuation, the curves change significantly between 1 and 8 mm height.

The plasma induced spanwise jets create a stagnation point above the middle of the covered electrodes and a downward flow above the exposed electrodes. The rapid actuation then yields increased fluctuations in downward-streamwise direction at the exposed electrode, as can be observed in Figure 7.6. The peak of the $\langle u'v' \rangle$ fluctuations and the corresponding height go up with voltage. Furthermore, Figure 7.5 shows an increase in magnitude of the $\langle -u'v' \rangle$ fluctuations at the middle of the covered electrode with plasma actuation. Note, that the peak of the $\langle -u'v' \rangle$ fluctuations gets larger and its position moves further away from the wall from 2 mm to around 2.5 mm height, for increasing actuation voltage. This behavior is caused by the intensification of ejection events. Since the induced flow in downward-streamwise direction above the exposed electrode is mostly smooth, the increase in magnitude of the Reynolds stresses at the middle of the covered electrode is significantly larger. Moreover, an increase in the magnitude of the $\langle u'v' \rangle$ fluctuations will logically yield similar increases of both $\langle u'^2 \rangle$ and $\langle v'^2 \rangle$.

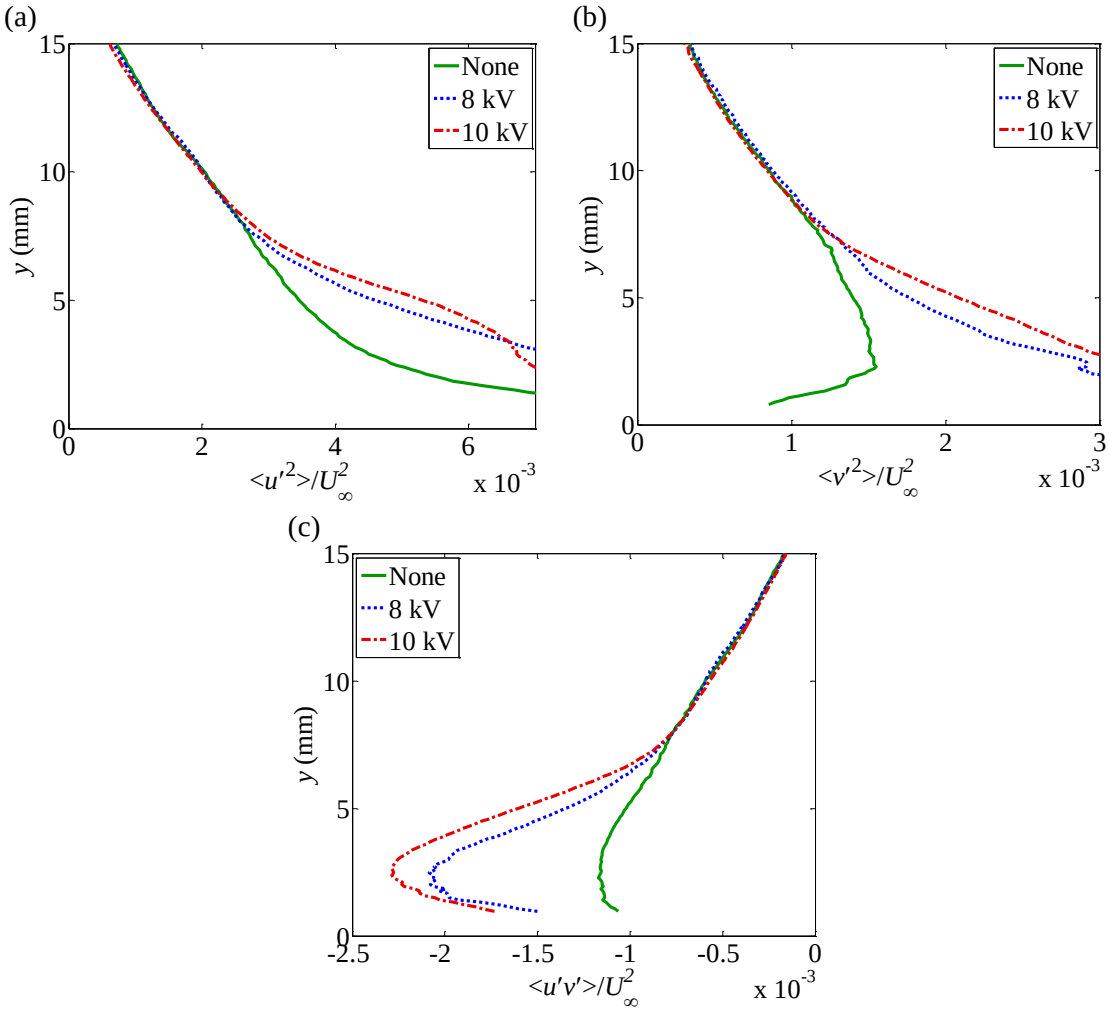

Figure 7.5: Profiles of the Reynolds stresses at the covered electrode for no plasma actuation, plasma actuation at 8 and 10 kV with 500 Hz. **(a)** $\langle u'^2 \rangle$ **(b)** $\langle v'^2 \rangle$ **(c)** $\langle u'v' \rangle$

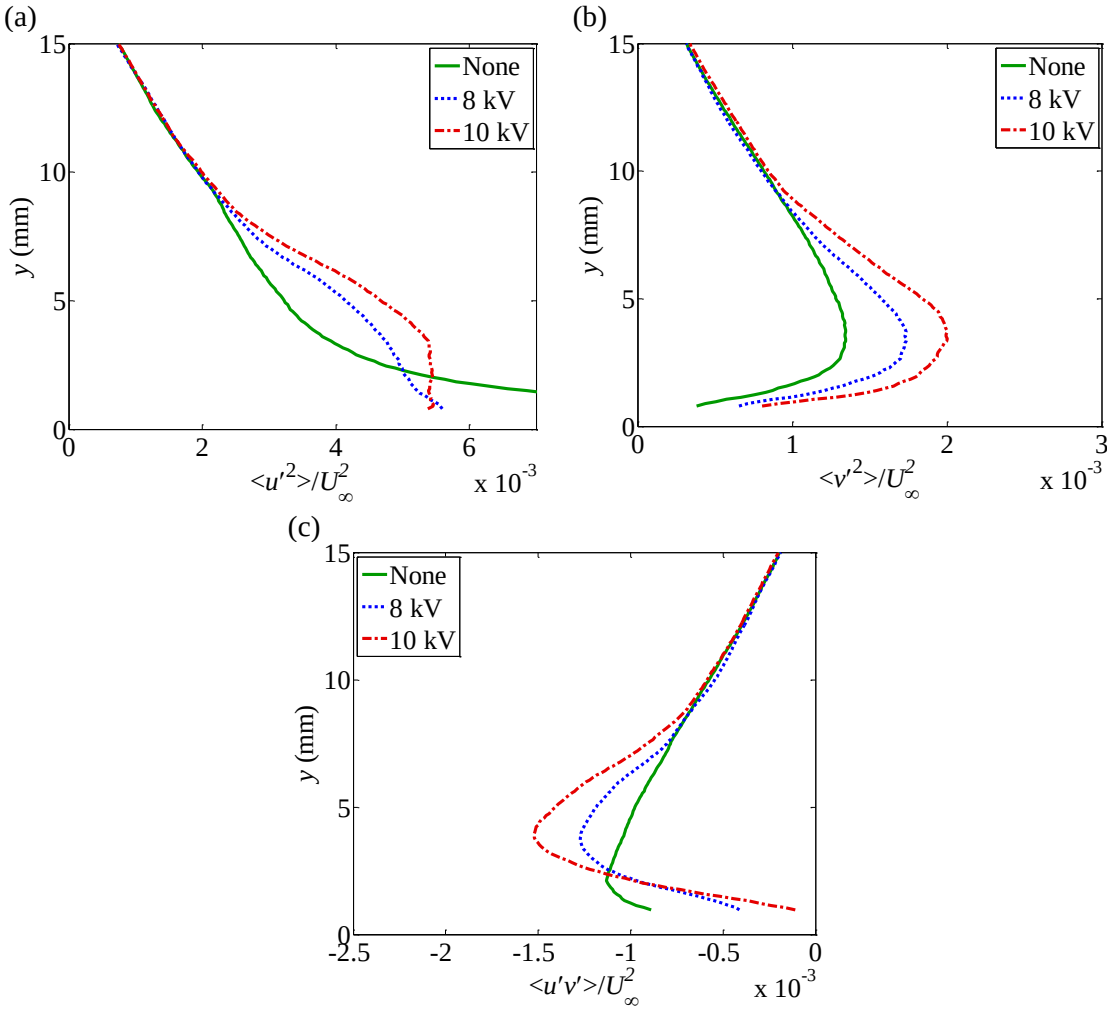

Figure 7.6: Profiles of the Reynolds stresses at the exposed electrode for no plasma actuation, plasma actuation at 8 and 10 kV with 500 Hz. **(a)** $\langle u'^2 \rangle$ **(b)** $\langle v'^2 \rangle$ **(c)** $\langle u'v' \rangle$

7.2.2 Streamwise-spanwise plane at $y^+ \approx 7$

In the previous section the effect of two different voltages was illustrated. In the current section the effects of actuation parameters (voltage and frequency), covered electrode width and free-stream velocity are determined for an extended range of these parameters.

For the experiments at the streamwise-spanwise plane the laser sheet was located just above the plate ($y^+ \approx 7$). For more details on the setup and the applied settings see section 5.3 and Table A.1 in Appendix A. An example of the recorded mean flow fields is presented in Figure 7.7, where the contour plot of the spanwise velocity is displayed on the left and the streamwise velocity on the right.

The results of the streamwise-spanwise 2C-PIV measurements are separated into the categories: meandering of streaks, start and end of the induced streaks, streamwise velocity, spanwise velocity, auto-correlation, and the power spectral density (PSD). The presented results for the streamwise and spanwise velocities have been averaged in streamwise direction to produce comparable plots.

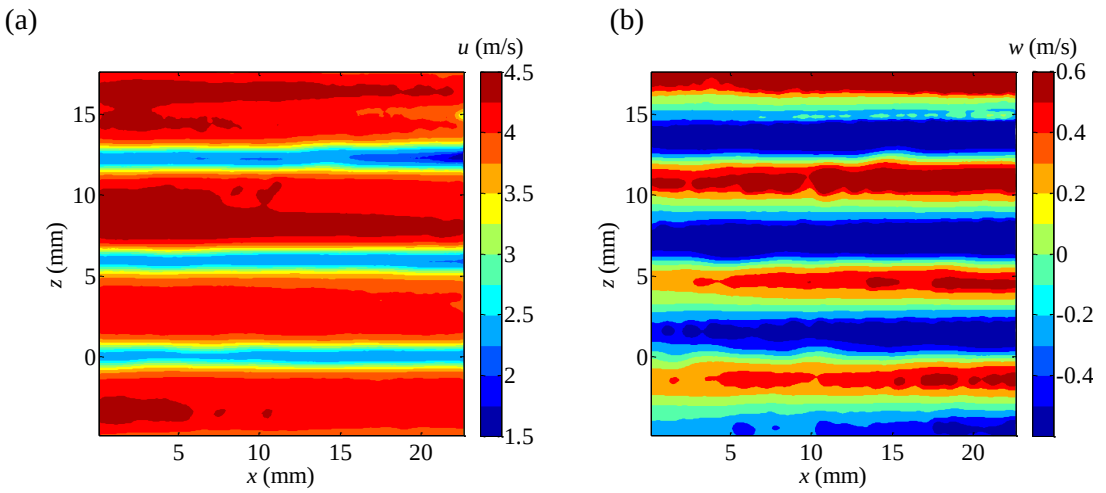

Figure 7.7: Contour plots of mean velocities at 12 kV and 500 Hz plasma actuation. **(a)** Streamwise velocity contour plot and **(b)** Spanwise velocity contour plot.

Meandering of induced streaks

The spatial meandering of the induced low-speed streaks can be illustrated by contour plots of instantaneous streamwise velocity fields shown in Figure 7.8. In the plots on the left the depicted streamwise velocity fields are without plasma actuation. These plots display a disorganized flow field of smaller and larger streaks. On the right hand side the plots represent the instantaneous flow fields with plasma actuation at 10 kV and 500 Hz. They show narrow spatially organized low-speed streaks with wider high-momentum regions in between them. Even though the streaks are not perfectly locked in spanwise direction, the flow field still remains highly organized. Furthermore, the induced streaks have approximately the same magnitude as the naturally occurring streaks.

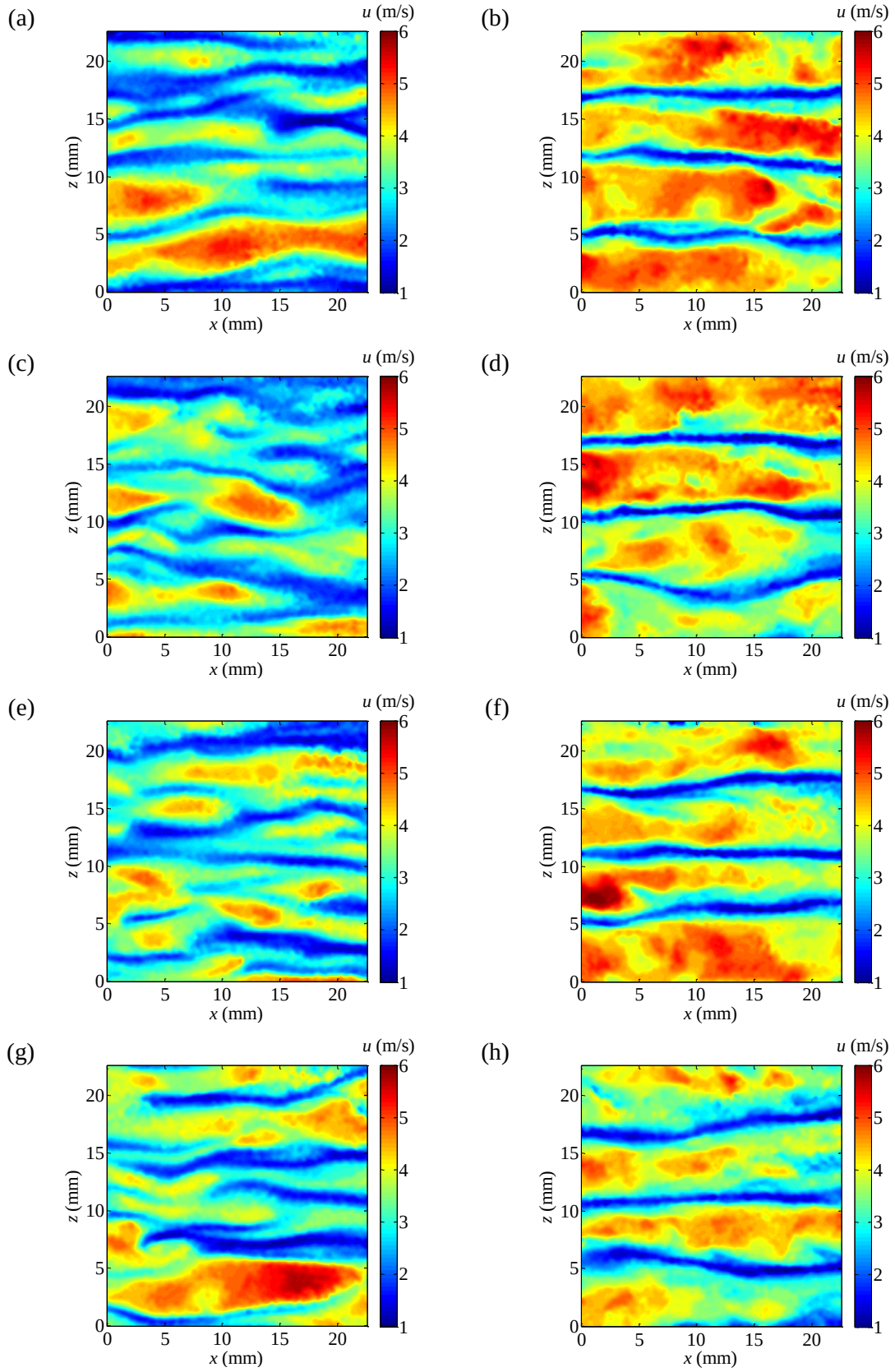

Figure 7.8: Contour plots of instantaneous streamwise velocity fields. The plots depicted on the left are without plasma actuation and the plots on the right with actuation at 10 kV and 500 Hz.

Start and end of induced streaks

The mean streamwise velocity fields obtained from the recordings taken at the start and downstream end of the actuator, an estimate could be determined for spatial length required to induce the streaks and the extend by which the artificially induced streaks persist behind the actuator. Figure 7.9 and Figure 7.10 display the streamwise velocity fields at, respectively, the start and end of the actuator, where the locations of the exposed electrodes are indicated. The Figure 7.9 show the streaks begin to develop after about 5 mm and are fully developed after approximately 20 mm. At the end of the actuator it is found that the extend of the persistence was approximately 20 mm.

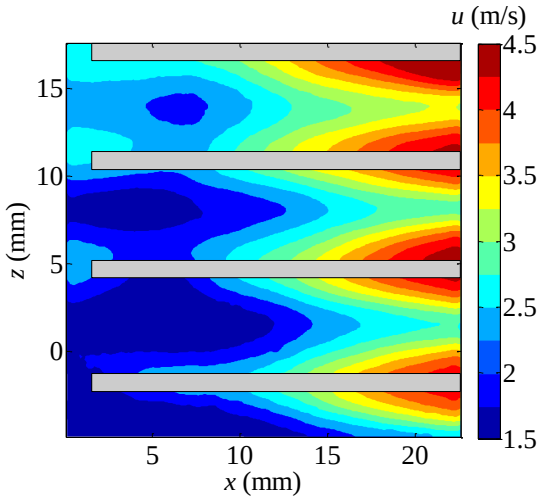

Figure 7.9: Contour plots of mean streamwise velocity at the start of the actuator, when actuated at 10 kV and 500 Hz. The locations of the exposed electrodes are indicated in the figure.

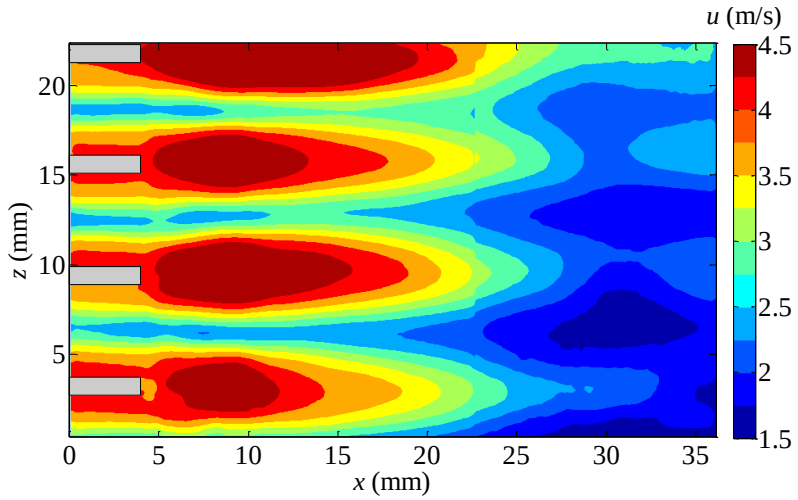

Figure 7.10: Contour plots of mean streamwise velocity at the downstream end of the actuator, when actuated at 10 kV and 500 Hz. The locations of the exposed electrodes are indicated in the figure.

Streamwise velocity

The plots showing the mean streamwise velocities of 2000 recordings against the spanwise distance for the various V_{pp}, f_{ac}, w_{cov} and U_{∞} are presented in Figure 7.11. During these measurements the free-stream velocity was set to 7 m/s and the plasma actuation was

performed at 10 kV with 500 Hz and a covered electrode width of 5 mm, unless indicated otherwise. The average uncertainty of the mean streamwise velocity $\varepsilon_{\bar{u}}$ normalized with free-stream velocity is 2.52×10^{-3}.

The response of the variation of the peak-to-peak voltage on the mean flow field is visualized in the Figure 7.11(a). By increasing the V_{pp} to 6 and 8 kV the mean streamwise velocity above the middle of the covered electrodes decrease. Further increase in voltage yields higher velocities, due to the insertion of momentum and thus energy into the boundary layer. The induced low- and high speed regions have widths of, respectively 1 and 5 mm.

At the exposed electrodes the attained streamwise velocities steadily increase with V_{pp} until a maximum is reached at 12 kV. Beyond 12 kV, the power supply is unable to provide the necessary amount of power or the space above the covered electrodes has become saturated, which leads to discharges losing a part of their mechanical effect (see section 3.3) and hence no further improvement at the location of the low- and high-speed streaks is observed, or it is a combination of both. Unfortunately there were no recordings made of the output voltages and power to determine the exact cause of the drop in velocity.

Note the behavior of the no plasma line in Figure 7.11(a). The streamwise velocity increases when moving towards the right, as a result of a slight inclination of the laser sheet. From the velocities at the left and right side of the no plasma line in Figure 7.11(a), the approximate heights of these locations was determined from velocity profile of Figure 7.1(a), from which it could be estimated that the inclination was approximately 0.37°. Furthermore, small drops in *u* can be observed, which are caused by small height differences at the surface, due to the exposed electrodes. Also the 10 kV line is displaying some abnormalities, since it's mostly smaller than the 8 kV line at the high-velocity region and looks shifted to the left compared to the other lines.

Figure 7.11(b) illustrates that the velocities at the exposed electrode increase with frequency, while at the middle of the covered electrode they remain approximately constant. For 250 Hz the influence of the plasma actuator is rather limited. Increasing the frequency to 500 Hz results in a large alteration, the peaks at the high velocity regions become significantly larger and minima at the covered electrode become visible. Further increase to 750 and a 1000 Hz leads to more extreme peaks and moreover it yields more constant velocities across the width of the embedded electrodes.

The effect of the covered electrode width can be examined in Figure 7.11(c). The wider the embedded electrode width the larger the maximum value above it. For every 2 mm increase in width the graph displays a 20% increase of the maximum. While the minimum values above the covered electrodes show almost no change. Further increase of the electrode width allows the plasma to extend farther, if the peak-to-peak voltage is high enough. However, the further the plasma extends the thinner the plasma region will become, hence yielding a reduction in the relative effectiveness of the actuator in producing jets.

In Figure 7.11(d) the result of raising the free-stream velocity from 7 to 9, 11 and 13 m/s is illustrated. The relative velocities at the exposed electrodes increase with free-stream velocity up to 11 m/s, after which a drop can be observed. Simultaneously the relative velocities at the middle of the covered electrode display a continuous increase. The increase up to 11 m/s at the exposed can be attributed to increased jet velocities, since a higher free-stream velocity provides a larger momentum inflow for the spanwise induced jets. Beyond 11 m/s the velocities at the high-speed regions relative to the free-stream velocity starts to decrease. The increase at the middle of the embedded electrode is due to the velocity profiles getting fuller as the free-stream velocity goes up, hence the relative velocity at the measurement height also increases.

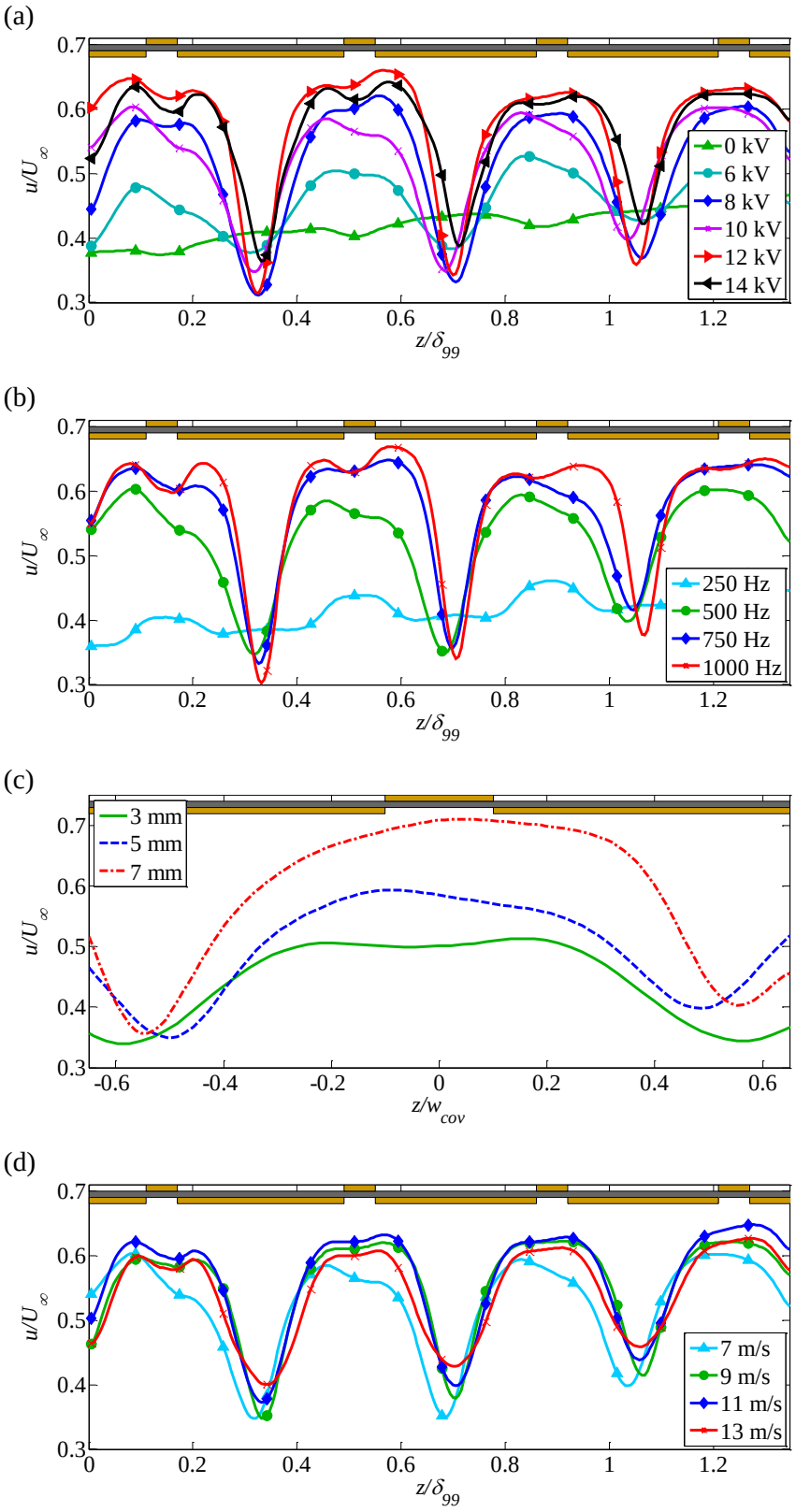

Figure 7.11: The mean streamwise velocity versus spanwise distance for **(a)** varying peak-to-peak voltage, **(b)** varying actuation frequency, **(c)** covered electrode width and **(d)** varying free-stream velocity.

The root-mean-squared (RMS) values for the various varying parameters are displayed in Figure 7.12. The RMS of the streamwise velocity has an error ε_{σ_u}, which when normalized with free-stream velocity is 1.26×10^{-3}.

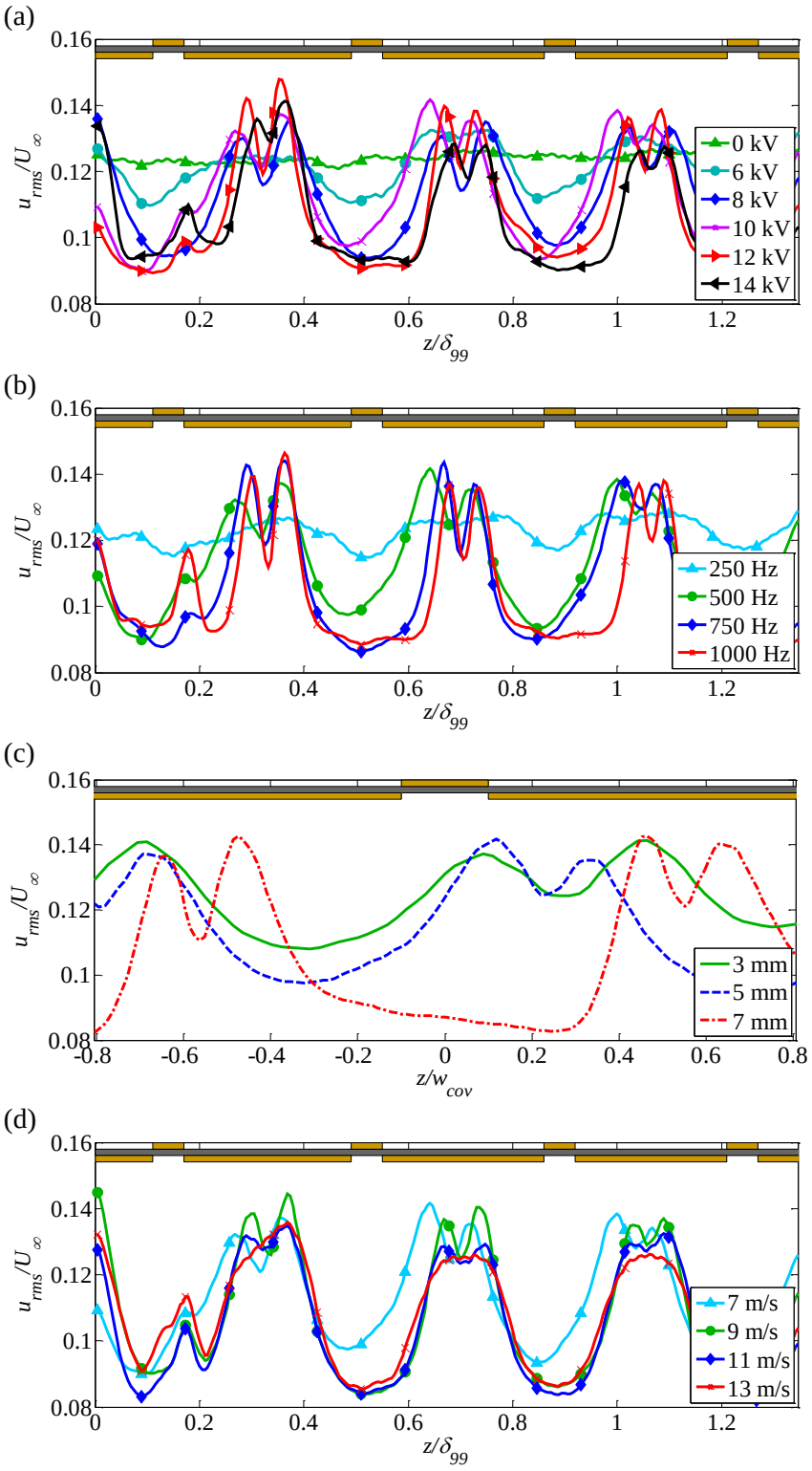

Figure 7.12: The RMS of the streamwise velocity versus spanwise distance for **(a)** varying peak-to-peak voltage, **(b)** varying actuation frequency, **(c)** covered electrode width and **(d)** varying free-stream velocity.

At the locations where the spanwise jets merge to form wall-normal jets, the RMS displays two distinct maxima. These maxima are up to 20% higher than the for the no plasma case. In the wider regions between the locations of the double peaks, the relative RMS values drop about 30%. These effects increase and become more pronounced by increasing the peak-to-peak voltage, frequency and embedded electrode width. On the other hand, the relative RMS shows almost no change when varying the free-stream velocity.

After close observation of the figures for the streamwise velocity and the corresponding RMS plots a general trend can be noticed. The better the actuator can induce the streaks, in terms of induced streamwise velocity, the lower the average RMS value. Hence, more extreme low- and high-speed streak velocities results in a reduced level of the turbulent streamwise fluctuations within the flow at a height of $y^+ \approx 7$.

Another method to decide on the effectiveness of certain values of actuation parameters in controlling low- and high-speed streaks is proper orthogonal decomposition (POD), which has been discussed in section 4.2.1. However, the results of the POD analysis on the streamwise velocity fields did not provide significant information about the induced streaks. For all completeness the analysis is presented in Appendix B.

Spanwise velocity

Similar plots as for the streamwise velocity have been generated for the spanwise velocity component and are displayed in Figure 7.13. Note that these results were obtained from the same experiments as mentioned above. The uncertainty of the mean spanwise velocity $\varepsilon_{\bar{w}}$, when normalized with U_∞ is 1.37×10^{-3}.

In Figure 7.13(a) the influence of the applied voltage on the spanwise induced velocities is presented. The induced spanwise jets evolve into stronger jets for higher voltages, although voltages higher than 12 kV lead to small reductions. As explained earlier, the power supply is unable to provide the required amount of power or the dielectric area above the covered electrodes has become saturated, resulting in a small reduction of the jet velocities. Note the reduced size of the peaks when moving to the right, as result of a slight inclination of the lasersheet.

The effect of the actuation frequency is illustrated in Figure 7.13(b). It displays the spanwise velocities of the induced jets becoming larger in magnitude for increasing frequency. The result is fluctuating too much to explicitly state that the threshold actuation frequency, at which a maximum induced velocity occurs, has been reached. However, it is clear that a frequency of a 1000 Hz is close to the threshold.

The Figure 7.13(c) shows the effect of the covered electrode width on the spanwise velocities of the jets. As anticipated, the magnitude of the spanwise jets increase with embedded electrode width. It can also be observed that velocities induced by the 7 mm width electrode are more than ten times larger in magnitude than those of the 3 mm width.

The higher free-stream velocity gives rise to more vortices within the boundary layer, hence leading to increased mixing of the flow, thereby causing a reduction of the spanwise induced jet velocities. Although this behavior can be observed in Figure 7.13(d), it also shows 9 m/s line has some peaks with a larger magnitude than the 7 m/s line. As described earlier, the larger free-stream velocity can result in more inflow of momentum at the exposed electrode for the spanwise jets, hence increasing their strength. However, at a certain point the increased mixing will take the overhand and reduce the strength of the jets.

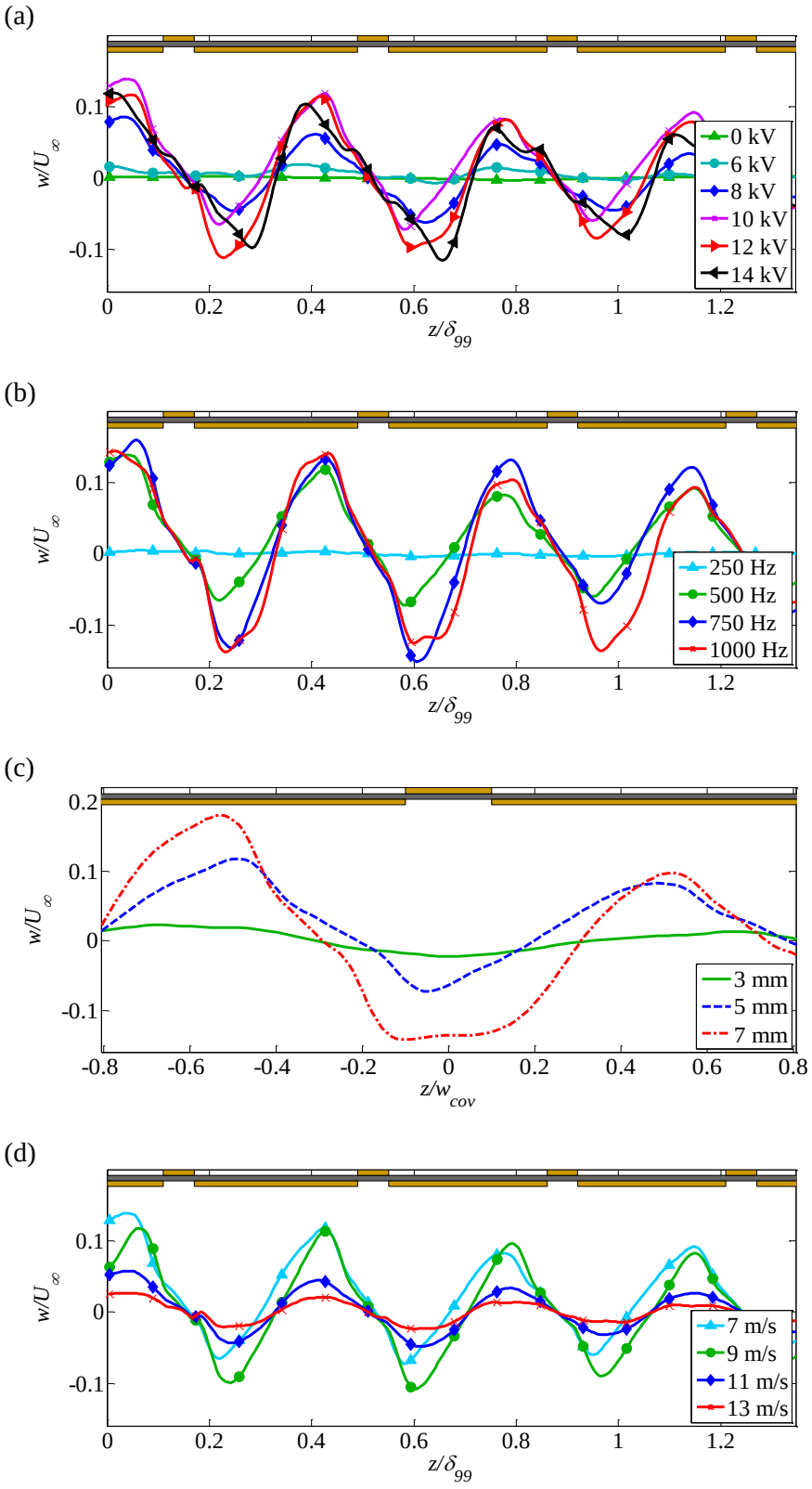

Figure 7.13: The mean spanwise velocity versus spanwise distance for **(a)** varying peak-to-peak voltage, **(b)** varying actuation frequency, **(c)** covered electrode width and **(d)** varying free-stream velocity.

Auto-correlation

The auto-correlation function is used to determine the spanwise spacing between the coherent structures (LSSs and HSSs). The auto-correlation function, as discussed in section 4.2.3, of the fluctuating streamwise velocity along the spanwise direction, can be expressed in terms of the auto-correlation coefficient ρ_{zz}.

The fluctuating streamwise velocity was acquired by subtracting the average value from the velocity field for each recording. Next the data on a spanwise line was taken, of which the auto-correlation coefficient was to be determined. The auto-correlation coefficients were calculated for 2000 images of every recording sequence, after which the mean was determined. The resulting auto-correlation coefficient-lines have been plotted in Figure 7.15 for varying voltage, frequency, covered electrode width and free-stream velocity. Note, only the right half of the graphs are plotted, since they are symmetric.

In Figure 7.14 a schematic of an array of plasma actuators is displayed with the locations of the low- and high speed regions on top of them. The spacing between the streaks is indicated by the arrows. The figure illustrates the spacing of the correlation peaks matching the spacing between the streaks. From Figure 7.15 it can be concluded, the voltage, frequency and free-stream velocity have no influence on the correlation of the streaks and thus also not on their spacing. Only the embedded electrode width affects the correlation, since it moves the centers of the streaks. Moreover, the average spacing between the streaks is remarkably constant.

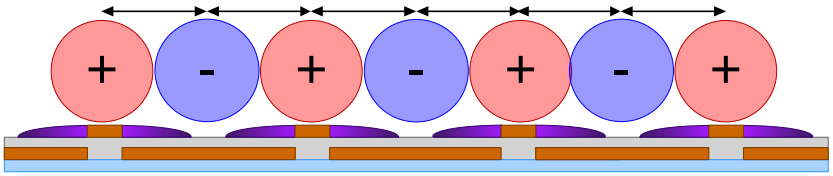

Figure 7.14: Schematic of the array of plasma actuators showing the low- and high speed streaks. The arrows indicate the spacing between the streaks.

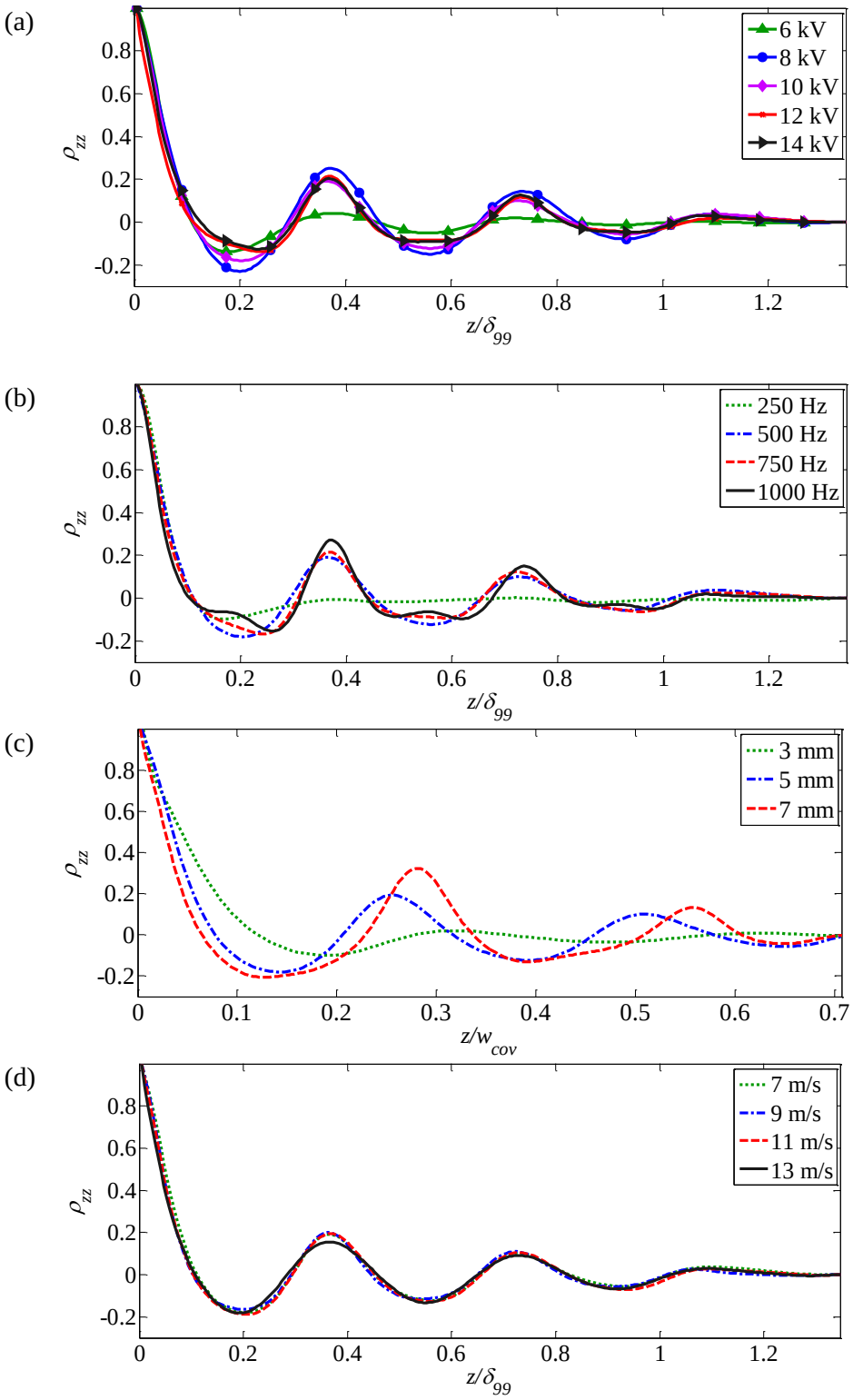

Figure 7.15: Auto-correlation coefficient of the streamwise velocity versus spanwise distance for **(a)** varying peak-to-peak voltage, **(b)** varying actuation frequency, **(c)** covered electrode width and **(d)** varying free-stream velocity.

Power spectral density of the spanwise velocity

The power spectral density (PSD) of the velocity fluctuations at an approximate height of y = 1 mm for no plasma actuation and plasma actuation with 8 and 10 kV at 500 Hz are presented in Figure 7.16. The PSD lines in the figures are denoted by z_1 to z_5, which denote, respectively,

streamwise lines ranging from the middle of a covered to the middle of an adjacent exposed electrode. The PSD is computed with a frequency resolution (frequency bin width) of f_{res} = 25 Hz, Hanning windowing with an effective noise bandwidth (ENBW) of 37.7 and a window overlap of 50%. The graphs show the PSD of the spanwise velocity fluctuations up to 2500 Hz, since the sampling frequency during the time-resolved measurements was 6000 Hz, the Nyquist criterion is satisfied.

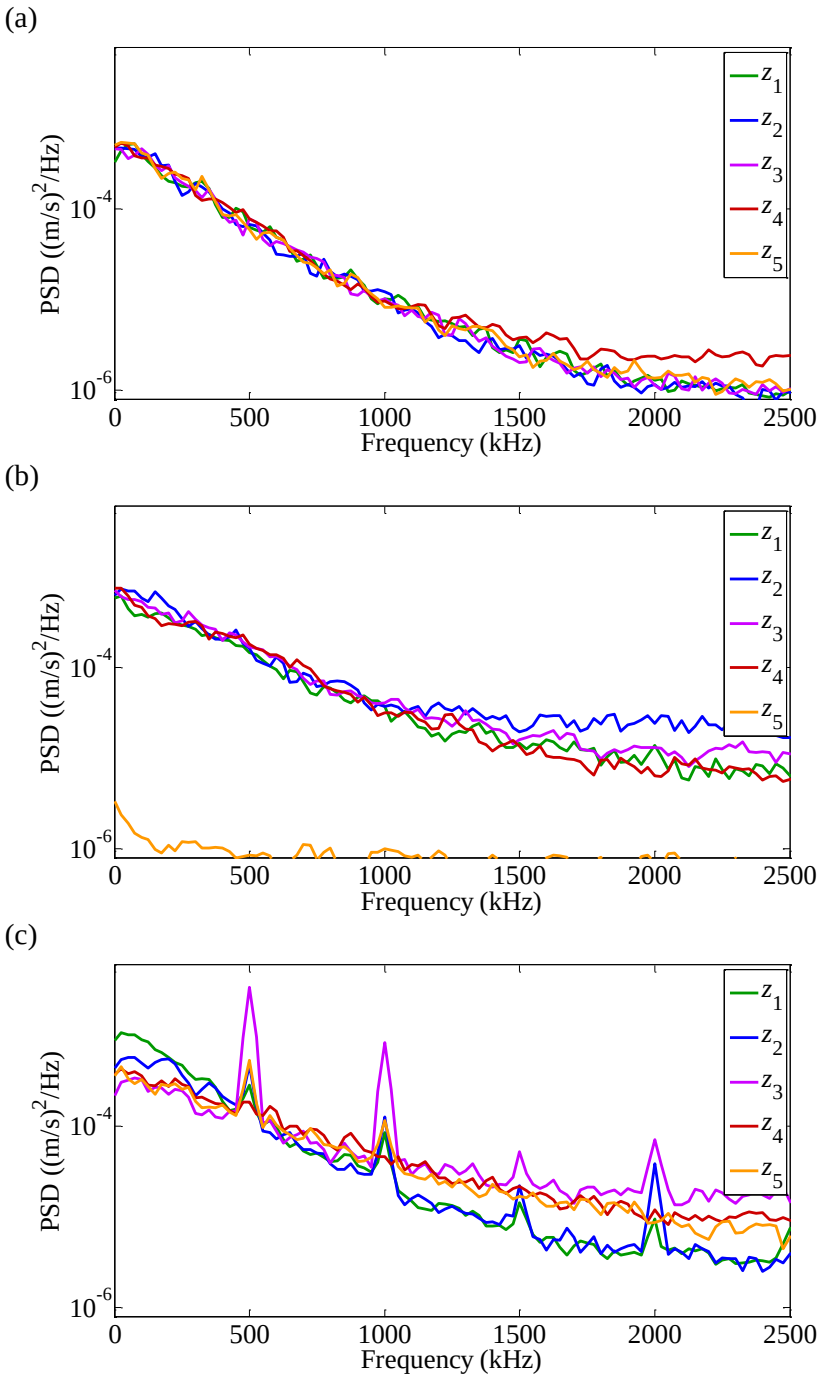

Figure 7.16: PSD function versus frequency at locations ranging from the middle of a covered to the middle of an adjacent exposed electrode, for **(a)** no plasma actuation, **(b)** plasma actuation at 8 kV and **(c)** at 10 kV with an actuation frequency of 500 Hz.

The applied plasma actuation frequency was 500 Hz, hence frequency peaks should be visible when the plasma was actuated. However, in the case of an 8 kV peak-to-peak voltage the peaks are unnoticeable, although the noise level at higher frequencies increases. This increase in noise is probably caused by the mixing effect due to the turbulence. Increasing the voltage to 10 kV, yields the presence of the peaks at 500, 1000, 1500 and 2000 Hz. Apparently the energy inserted by the plasma actuation is largest in the center between the middle of the low and high-speed regions.

7.2.3 Spanwise wall-normal plane

In this section the induced jet velocities of the plasma actuator array, as observed from the spanwise wall-normal plane, in a free-stream flow of 7 m/s for two different applied voltages will be discussed. The experiments were again conducted with the array having a 5 mm covered and 1 mm exposed electrode width. More information about the configuration and the applied plasma actuation settings can be found in section 5.3 and Table A.3 in Appendix A.

Under the described conditions, three recordings were obtained for, respectively, no plasma actuation, plasma actuation at 10 and 12 kV at 500 Hz. From these statistical recordings of the spanwise wall-normal plane, the averages of the flow velocities in spanwise and wall-normal direction were determined. The mean velocity fields of the velocity components *v* and *w*, are displayed in the Figures 7.17-7.18.

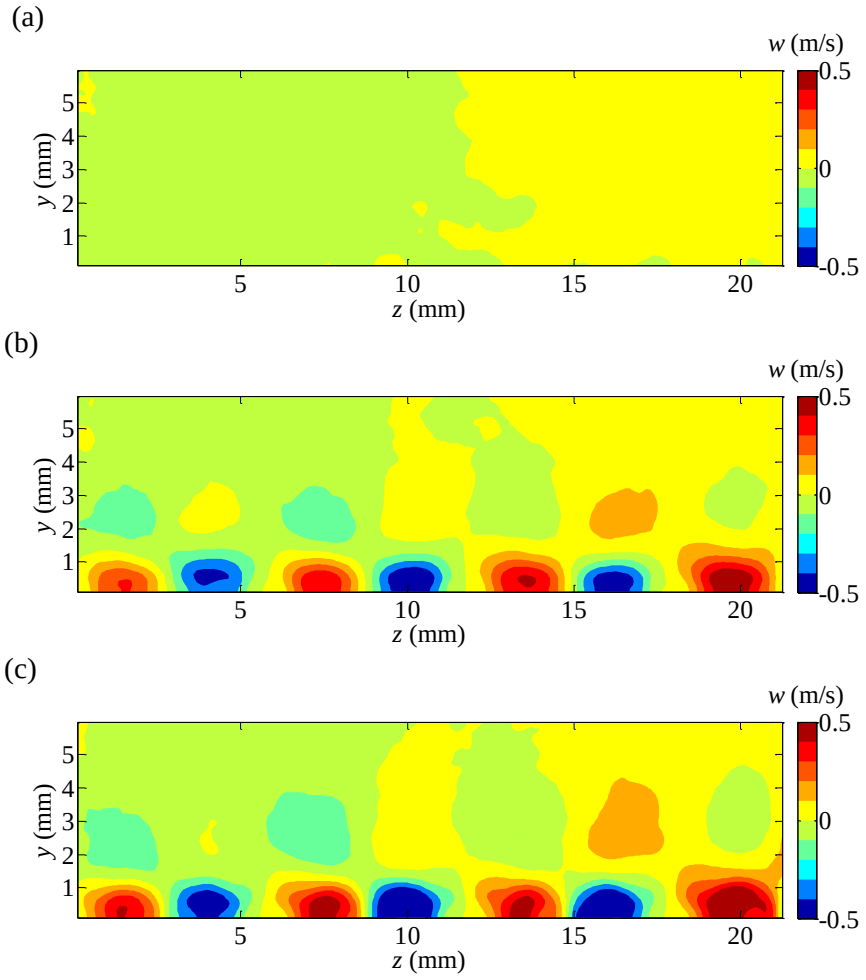

Figure 7.17: The mean spanwise velocity field in a flow of 7 m/s for **(a)** no plasma actuation, plasma actuation at **(b)** 10 kV and **(c)** 12 kV with 500 Hz.

In Figure 7.17(b) the spanwise velocity component is shown for plasma actuation at 10 kV. The induced spanwise jets flowing to the left and right are clearly present, reaching average velocities with a magnitude 0.4 m/s. Each spanwise jet extends approximately 2 mm in spanwise and 1 mm in wall-normal direction, which is similar to the results found without free-stream flow (see section 6.2). The spanwise flow field at 12 kV is visualized in Figure 7.17(c), which shows an almost negligible increase in magnitude of the jets. The maximum induced spanwise velocities occur at about 0.5 mm from the wall, which is in accordance with the results found by Moreau (2007).

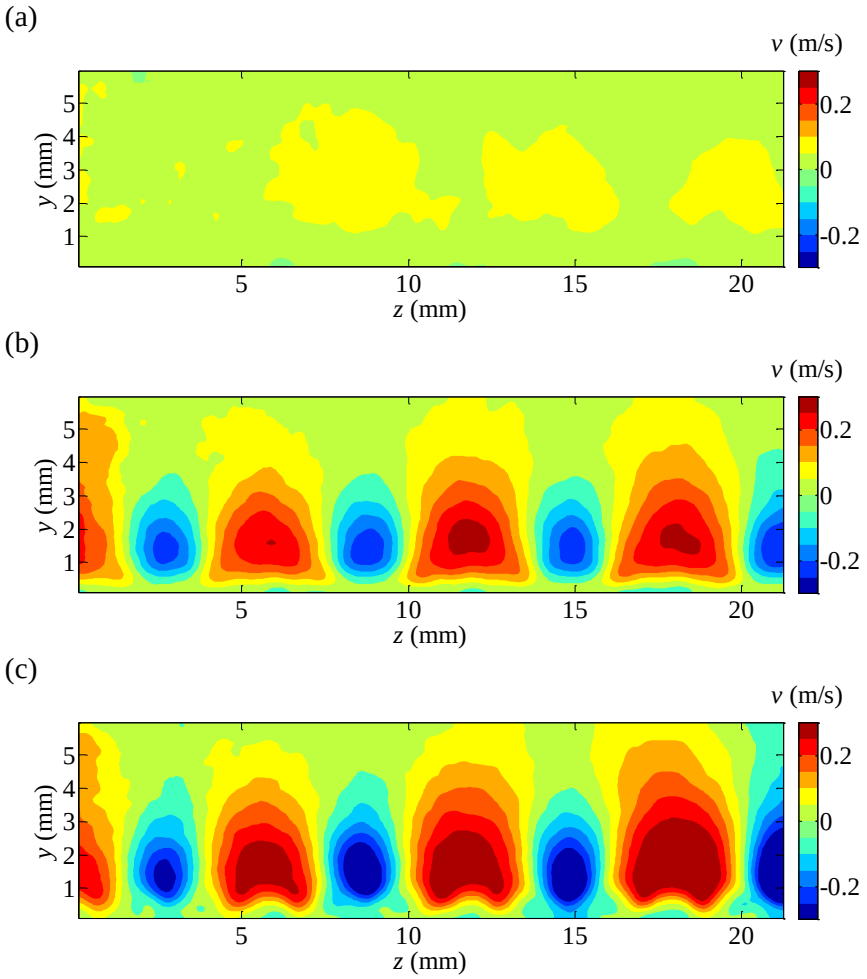

Figure 7.18: The mean wall-normal velocity field in a flow of 7 m/s for **(a)** no plasma actuation, plasma actuation at **(b)** 10 kV and **(c)** 12 kV with 500 Hz.

The opposing spanwise jets lead to the formation of the wall-normal jets above the middle of the grounded electrodes. The average wall-normal velocity of these jets can be retrieved from Figure 7.18. For the no plasma case blobs with an average wall-normal velocity of 0.5 m/s are present, which are due to the small height differences at the locations of the exposed electrodes. At plasma actuation of 10 kV the jets attain average velocities close to 0.3 m/s and at 12 kV just above 0.3 m/s. Based upon the 0.1 m/s contour lines, these jets stretch to a height of 5 mm and have a base width of approximately 3.5 mm. Due to the higher voltage at 12 kV, the velocities within the area of the jets is considerably higher than at 10 kV.

The flow pulled towards the surface, due to momentum conservation, is confined to small areas of 2 by 4 mm, when looking at the -0.1 m/s contour line. The average magnitudes of these downward jets are, respectively, 0.2 and 0.3 m/s.

By comparison with the contour plots without free-stream flow of section 6.2, it can be concluded that the obtained wall-normal jets with a free-stream velocity of 7 m/s are stronger and cover a larger area. At the same time the downward flow at the exposed electrode is reduced, when comparing to the no free-stream flow results.

Without free-stream flow, the conservation of momentum requires a flow towards the surface above the exposed electrodes. However, in the case with a free-stream flow, the air of the free-stream flow is sucked towards the plate surface, which results in a region with relatively high velocity and significantly larger inflow of momentum for the plasma induced spanwise jets. Hence the spanwise jets increase in strength and the resulting wall-normal jets will then also increase in strength. Since most of the momentum inflow is in streamwise direction, the inflow in wall-normal direction is reduced in comparison to cases without free-stream flow. Nevertheless it should be noted, the increase in strength of the spanwise jets due to the free-stream velocity relative to the case without free-stream flow is not clearly observed. This could be explained by cross-flows or recirculation due to vortices in the cases without free-stream flow influencing the measured induced velocities.

8 Concluding remarks

The aim of this thesis work was *to experimentally investigate and optimize streamwise-oriented plasma actuators that produce wall-normal jets in order to arrange the low- and high-speed streaks of a fully developed turbulent boundary layer in an organized alternating pattern without spatial meandering.* The obtained streak pattern is investigated for future application in control of turbulent boundary layers. Conclusions drawn from the work are presented in section 8.1 and the future recommendations in 8.2.

8.1 Conclusions

In this study the effectiveness of the plasma actuators in inducing wall-normal jets and their effects on the flow statistics as well as the coherent structures are presented. The ability of the actuators in controlling the low- and high-speed streaks is investigated using PIV at free-stream velocities of 7 to 13 m/s. The obtained PIV recordings of the induced flow fields were furthermore used to determine the PSD and auto-correlation functions.

Working principle of plasma array

The working principle of an array of streamwise oriented plasma actuators was analyzed without free-stream flow and also at several free-stream velocities. The resulting flow fields indicated two opposing spanwise induced wall-jets collide in the middle above the covered electrode, creating a stagnation point. From there the flow is forced in the wall-normal direction, resulting in the formation of a wall-normal jet. Due to momentum conservation the flow is sucked towards the surface on the two sides of the actuator array above the exposed electrodes. In the case without free-stream velocity, the induced upward and downward flow yields recirculation by means of streamwise vortices. However, if the plasma is actuated within a turbulent boundary layer the formation of distinct streamwise vortices rarely occurs due to the turbulent mixing within the boundary layer.

Effects of actuation parameters without a free-stream flow

A parametric study on the effect of the actuation parameters without free-stream flow indicates the induced spanwise and wall-normal jet velocities depend on the peak-to-peak voltage and actuation frequency. An increase in the wall-normal jet centerline velocity is observed by increasing the voltage till 10 kV. No significant intensification of the jet is observed at 12 kV which can be due to limitations of the power supply or saturation of the plasma above the covered electrode. The results at actuation frequencies of 500 and 1000 Hz display significant increase in the centerline velocity of the jet at higher frequencies.

Streak control

At a free-stream velocity of 7 m/s the streaks were fixed in an alternating pattern along the spanwise direction by applying plasma actuation with a peak-to-peak voltage of 10 kV at an actuation frequency of 500 Hz and a covered electrode width of 5 mm. A streamwise length of about 5 mm was required to induce the streaks and they persisted for approximately 20 mm downstream of the actuator. The rearranged low- and high speed streaks had widths of 1 and 5 mm, and at a height of $y^+ \approx 7$ the streamwise velocity attained values of, respectively, 2.5 and 4 m/s.

Effects of actuation and geometric parameters with a free-stream flow

The effects of voltage, frequency and embedded electrode width at 7 m/s indicate similar trends as for the cases without a free-stream flow. The induced jets evolve into stronger jets for higher voltages, frequencies and wider embedded electrodes, although voltages higher than 12 kV lead to small reductions.

The higher velocity of the jets for increased voltage was also observed in the mean streamwise velocity profiles, as the gradient was increased up to a height of 1 mm (or $y^+ \approx 23$) from the surface. At the middle of the covered electrode a relatively lower mean velocity was found between 1 and 6 mm (or $23 < y^+ < 136$). The increase in the gradient can be appointed to the suction of high streamwise velocity towards the surface at the exposed electrode. Consequently the spanwise jets carry with them a strong streamwise component, hence also causing an increased gradient at the middle of the covered electrode.

At a height of $y^+ \approx 7$ the average streamwise velocity distribution in spanwise direction displayed valleys above the middle of the exposed electrodes and considerably wider high-speed regions in between them. The streamwise velocity at these high speed regions increased with peak-to-peak voltage, frequency and covered electrode width. The observed valleys are only enhanced by increase in voltage, as that allows the plasma to extend farther. They remain at approximately constant velocity when the frequency and covered electrode width are varied. In addition, the correlation of the streamwise velocity showed the variations of the actuation parameters have no influence on the spacing of the low- and high-speed streaks. Moreover, the average spacing between the streaks was observed to be remarkably constant. In the power spectra, the actuation at 10 kV with 500 Hz displayed frequency peaks at 500 Hz and every multiple of 500. These were not present for 8 kV, however the noise level at higher frequencies was increased, which is probably caused by mixing effects due to turbulence.

Effects of free-stream velocities

Another parameter that was varied, was the free-stream velocity. By increasing it to 9 m/s the velocity of the spanwise induced jets was enhanced. However, beyond 9 m/s the induced velocities started to decrease, indicating that the mixing effects of the flow were becoming too strong. Nevertheless, the wall-normal jets continued to display an increase in the wall-normal jet velocity, suggesting a more efficient merging process of the two spanwise jets. At the locations of the low- and high-speed streaks the streamwise velocity relative to the free-stream velocity was found to increase up to 11 m/s. For the high-speed regions this can be largely attributed to increased spanwise jet velocities, since a higher free-stream velocity provides a larger momentum inflow to the spanwise induced jets. Although it should be noted that at all spanwise locations the velocity profiles are getting fuller as the free-stream velocity increases.

Effects on turbulent fluctuations

Along the wall-normal direction, the rapid plasma actuation leads to higher fluctuations, due to intensification of the sweep events at the exposed electrode, but more importantly it significantly intensifies the ejection events at the covered electrode. These increased fluctuation levels are clearly present in the profiles of the turbulent fluctuations, although the change in the fluctuation level is considerably smaller above the exposed electrode, since there the fluctuations are due to indirect effects of the actuation and hence more smooth. Moreover, the results depict that at the exposed, the location of the fluctuation peak moves up as a result of the plasma actuation.

Along the spanwise direction the fluctuations of the streamwise velocity depict a specific trend. At the locations where the spanwise jets merge to form wall-normal jets, the fluctuations displays two distinct maxima. These maxima are up to 20% higher than for the no plasma case. In the wider regions between the locations of the double peaks, the relative RMS values drop about 30%. These effects increase and become more pronounced with

increase of peak-to-peak voltage, frequency and embedded electrode width. On the other hand, the relative RMS shows almost no change when varying the free-stream velocity. From the streamwise velocity and corresponding RMS results, it can be concluded that higher velocities of the induced wall-normal jets leads to lower average fluctuation values. Hence, more extreme velocities at the locations of the low- and high-speed regions results in a reduced level of the turbulent streamwise fluctuations within the flow at a height of $y^+ \approx 7$.

Summary

The applied array of wall-normal jet inducing plasma actuators have been found to effectively arrange the low- and high speed streaks into an organized alternating pattern up to free-stream velocities of 13 m/s. Although some small spatial meandering of the low-speed streaks was observed from the instantaneous velocity fields, the statistical data exhibited correlation of the streaks for peak-to-peak voltages above 6 kV. Since operating the actuator increases the gradient of the mean streamwise velocity close to the wall and because it enhances mixing in the boundary layer, it could be applied as a mechanism for separation control.

8.2 Recommendations

The recommendations given in this section are provided for future research on wall-normal jet producing streamwise oriented plasma actuators in controlling the low- and high speed streaks for future applications on control of turbulent boundary layers, such as suppression of vortex shedding, separation control, drag reduction and laminar-to-turbulent transition control.

With a possible application for postponing of separation, the test cases should be extended stepwise from this current flat plate configuration to more complex configurations. For example a boundary layer with an adverse or positive pressure gradient could be considered, such that the ability of the actuator in postponing separation can be tested.

Furthermore, understanding of the wall-normal jet creation is a fundamental part in optimizing the plasma actuator. Hence the merging of the opposing spanwise jets to form wall-normal jets near the stagnation point should be investigated into more detail, as at a certain voltage the spanwise induced jets decrease in strength while the wall-normal jets keep increasing. This research is also to be performed for the resulting ejection events, as they are responsible for the low-speed streaks.

Further research should be towards the development of actuators with smaller electrode widths that produce stronger wall-normal jets. The application of higher voltages and frequencies could improve the control of the streaks at higher free-stream velocities. As the turbulent energy will be higher, requiring stronger plasma induced jets. Moreover, the flow scales in the near-wall region will become smaller. Hence the electrode spacing should be reduced, in order to have the electrode spacing comparable to the small scale structures of the turbulent boundary layers.

Regarding the manufacturing of the actuators, spraying the copper or even the use of printed circuits boards could be considered. Since the manual manufacture of these electrodes from copper tape is highly inaccurate. Especially if electrodes smaller than one millimeter have to be produced.

At the middle of the covered electrode, the current configuration decreases the gradient very close to wall. However, above a considerably larger surface area the gradient is significantly increased, which leads to a higher wall skin-friction. This is caused by higher streamwise fluid that is pulled towards the surface. Hence, if the flow of high streamwise momentum fluid towards the wall could be reduced significantly, a reduction of wall skin friction may be obtained.

Bibliography

Adrian, R. J. (2007). Hairpin vortex organization in wall turbulence. *Phys. Fluids*, 19:041301.

Adrian, R. J., Meinhart, C. D. and Tomkins, C. D. (2000). Vortex Organization in the Outer Region of the Turbulent Boundary Layer. *J. Fluid Mech.*, 422:1-54.

Artana, G., Sosa, R., Moreau, E. and Touchard, G. (2003). Control of the nearwake flow around a circular cylinder with electrohydrodynamic actuators. *Exp. Fluids*, 35:580.

Benard, N., Jolibois, J., Moreau, E., Sosa, R., Artana, G. and Touchard, G. (2008). Aerodynamic plasma actuators: a directional micro jet device. *Thin Solid Films*, 516:6660–6667.

Benard, N. and Moreau, E. (2011). On the vortex dynamic of airflow reattachment forced by a single non-thermal plasma discharge actuator. *Flow Turbul. Combust.*, 87:1.

Blackwelder, R. F. (1978). The bursting process in turbulent boundary layers. *Lehigh Workshop on Coherent Structure in Turbulent Boundary Layers*. ed. C. R. Smith, D. E. Abbott, pp. 211-27.

Blackwelder, R. F., Eckelmann, H. 1979. Streamwise vortices associated with the bursting phenomenon. *J. Fluid Mech.*, 94:577-94.

Blackwelder, R. F., Kovasznay, L. S. G. (1972). Time scales and correlations in a turbulent boundary layer. *Phys. Fluids*, 15:1545-54.

Bogard, D. G., Tiederman, W. G. (1986). Burst detection with single-point velocity measurements. *J. Fluid Mech.*, 162:389-413.

Boucinha, V., Joussot, R. Magier, P. Weber, R. and Leroy-Chesnau, A. (2008). Characterization of the ionic wind produced by a DBD actuator designed to control the laminar-to-turbulent transition. *14th Symp on Apllications of Laser Techniques to Fluid Mechanics (Lisbon, Portugal, 07-10 July, 2008)*, Paper No. 1352.

Breuer K.S., Haritonidis J.H. and Landahl M.T. (1989). The control of transient disturbances in a flat plate boundary layer through active wall motion, *Phys. Fluids A*, 1:574.

Cantwell, B. J. (1981). Organised motion in turbulent flow. *Annu. Rev. Fluid Mech.*, 13:457.

Choi, H., Moin, P., Kim, J. (1993). Direct numerical simulation of turbulent flow over riblets. *J. Fluid Mech.*, 255:503–539.

Choi K.-S., Jukes T. and Whalley R. (2011). Turbulent boundary-layer control with plasma actuators, *Phil. Trans. R. Soc. A*, 369:1443-1458.

Clauser, F.H. (1956). The turbulent boundary layer. *Advances in Applied Mechanics*, 4:1–51.

Cordier L. and Bergmann M. (2011). *Proper Orthogonal Decomposition: an overview*, Laboratoire d'energétique et de mécanique théorique et appliquée, Vandoeuvre Cedex, France.

Corino, E.R., Brodkey, R.S. (1969). A visual investigation of the wall region in turbulent flow. *J. Fluid Mech.*, 37:1-30.

Corke, T. C., Enloe, C. L. and Wilkinson, S.P. (2010). Dielectric Barrier Discharge Plasma Actuators for Flow Control. *Annu. Rev. Fluid Mech.*, 42:505-29.

Corke, T. C., He, C. and Patel, M. P. (2004). Plasma flaps and slats: An application of weakly ionized plasma actuators. Second AIAA Flow Control Conference, *AIAA J.*, Paper No. 2004-2127.

Corke, T. C., Mertz, B. and Patel, M. P. (2006). Plasma flow control optimized airfoil. 44th AIAA Aerospace Sciences Meeting and Exhibit, *AAIA J.*, Paper No. 2006-1208.

Corke, T., Post, M. and Orlov, D. (2009). Single dielectric barrier discharge plasma enhanced aerodynamics: physics, modeling and applications. *Exp. Fluids*, 46:1-26.

Corrsin, S. (1943). Investigations of flow in an axially symmetric heated jet of air. *NACA Adv. Conf. Rep. 3123*.

Corrsin, S., Kistler, A. (1954). The free stream boundaries of turbulent flows. *NACA Tech. Note No. 3133*; also *NACA Tech. Rep. No. 1244 (1955)*.

DeGraaff, D.B. & Eaton, J.K. (2000). Reynolds-number scaling of the flat-plate turbulent boundary layer. *Journal of Fluid Mechanics*, 422:319–346.

Elsinga G.E., Scarano F., Wieneke B., and van Oudheusden B.W. (2006). Tomographic particle image velocimetry. *Experiments in Fluids*, 41:933-947.

Enloe, C. L., Font, G., McLaughlin, T. E., Orlov, D. (2008). Surface potential and longitudinal electric field measurements in the aerodynamic plasma actuator. *AIAA J.*, 46:2730-40.

Enloe, C. L., McHarg, M., Font, G., McLaughlin, T. E. (2009). Plasma-induced force and self-induced drag in the dielectric barrier discharge aerodynamic plasma actuator. Presented at AIAA Aerosp. Sci. Meet., 47th, Orlando, *AIAA J.*, Paper No. 2009-1622.

Enloe, C. L., McLaughlin, T. E., VanDyken, R. D., Kachner, K. D., Jumper, E. J., Corke, T. C., Post, M. and Haddad, O. (2004a). Mechanisms and responses of a single dielectric barrier plasma actuator: geometric effect. *AIAA J.*, 42: 595-604.

Enloe, C. L., McLaughlin, T. E., VanDyken, R. D., Kachner, K. D., Jumper, E. J. and Corke, T. C. (2004b). Mechanisms and responses of a single dielectric barrier plasma actuator: plasma morphology. *AIAA J.*, 42: 589-94.

Erm, L.P. & Joubert, P.N. (1991) Low Reynolds number turbulent boundary layers. *Journal of Fluid Mechanics*, 230:1-44.

Falco, R. E. (1977). Coherent motions in the outer region of turbulent boundary layers. *Phys. Fluids*, 20:5124-32.

Falkenstein, Z., Coogan, J. (1997). Microdischarge behaviour in the silent discharge of nitrogen-oxygen and water-air mixtures. *J. Phys. D*, 30:817–25.

Forte, M., Jolibois, J., Pons, J., Moreau, E., Touchard, G. and Cazalens, M. (2007). Optimization of a dielectric barrier discharge actuator by stationary and non-stationary measurements of the induced flow velocity: application to airflow control. *Exp. Fluids*, 43:917–928.

Goksel, B., Greenblatt, D., Rechenberg, I., Nayeri, C. N. and Paschereit, C. O. (2006). Steady and unsteady plasma wall jets for separation and circulation control. Third AIAA Flow Control Conference, *AIAA J.*, Paper No. 2006-3686.

Grundmann, S., Tropea, C. (2007). Experimental transition delay using glow-discharge plasma actuators. *Exp. Fluids*, 42(4):653–657.

Hanson R., Lavoie P., Naguib A., Morrison J. (2010). Transient growth instability cancelation by a plasma actuator array, *Exp. Fluids*., 49:1339.

Head, M. R. and Bandyopadhyay, P. R. (1981). New aspects of turbulent boundary-layer structure. *J. Fluid Mech.*, 107: 297.

Head, M. R. and Bandyopadhyay, P. (1978). Combined flow visualization and hot wire measurements in turbulent boundary layers. *Lehigh Workshop on Coherent Structure in Turbulent Boundary Layers*, ed. C. R. Smith, D. E. Abbott, pp. 98-129

Heinzel G., Rüdiger A., Schilling R. (2002). *Spectrum and spectral density estimation by the Discrete Fourier transform (DFT), including a comprehensive list of window functions and some new flat-top windows*, Internal Report, Max-Planck-Institut für Gravitationsphysik, Hannover.

Herpin S.C.S., Wong C.Y., Stanislas M., Soria, J. (2008). Stereoscopic PIV measurements of a turbulent boundary layer with a large spatial dynamic range, *Experiments in Fluids*, 45(4):745-763.

Hinze, J. O. 1959. Turbulence, 2nd edn. McGraw-Hill, New York.

Honkan, A. and Andreopoulos, Y. (1997) Vorticity, strain-rate and dissipation characteristics in the near-wall region of turbulent boundary layers. *Journal of Fluid Mechanics*, 350:29–96.

Huang, J., Corke, T. C. and Thomas, F. O. (2006). Plasma actuators for separation control of low-pressure turbine blades. *AIAA J.*, 44:51.

Huang, X. and Zhang, X.(2008). Streamwise and spanwise plasma actuators for flow-induced cavity noise control. *Phys. Fluids*, 20:037101.

Hultgren, L. and Ashpis, D. (2003). Demonstration of separation delay with glow discharge plasma actuators. 41st AIAA Aerospace Sciences Meeting and Exhibit, *AIAA J.*, Paper No. 2003-1025.

Jacobson, S. A. and Reynolds, W. C. (1998). Active control of streamwise vortices and streaks in boundary layers, *J. Fluid Mech.*, 360:179-211.

Jayaraman, B. and Shyy, W. (2008). Modeling of dielectric barrier discharge-induced fluid dynamics and heat transfer. *Progress in Aerospace Sciences*, 44(3):139.

Jiménez, J., Moin, P. (1991). The minimal flow unit in near-wall turbulence. *J. Fluid Mech.*, 225: 213–240.

Jukes T. N., Choi K. S., Jonhson G. A. and Scott S. J. (2006). Turbulent drag reduction by surface plasma through spanwise flow oscillation. AIAA Meeting (San Francisco, USA, June 2006), *AIAA J.*, Paper No. 2006-3693.

Kerho, M., Heid, J., Kramer, B. and Ng, T. (2000). Active drag reduction using selective low rate suction, 18th AIAA Applied Aerodynamics Conference (14-17 August 2000, Denver, CO), *AIAA J.*, Paper 2000-4018.

Kim, H. T., Kline S. J., Reynolds, W. (1971). The production of the wall region in turbulent flow. *J. Fluid Mech.*, 50:133-60.

Kim, J., Moin, P. & Moser, R. D. (1987). Turbulence statistics in fully developed channel flow at low Reynolds number. *J. Fluid Mech.*, 177:133-166.

Kim, K. C. and Adrian, R. J. (1999). Very large-scale motion in the outer layer. *Phys. Fluids*, 11:417.

Klebanoff, P.S. (1954). Characteristics of turbulence in a boundary layer with zero pressure gradient. *NACA-TN-3178*; also *NACA-R-1247 (1955).*

Kline, S.J., Reynolds, W.C., Schraub, F.A. and Runstadler, P.W. (1967). The structure of turbulent boundary layers. *J. Fluid Mech.*, 30:741–773.

Komminaho, J. & Skote, M. (2002). Reynolds stress budgets in Couette and boundary layer flows.
Flow Turbul. Combust., 68:167–192.

Kostas J., Soria J., and Chong M.S. (2005). A comparison between snapshot POD analysis of PIV velocity and vorticity data, *Experiments in Fluids*, 38:146-160.

Kovasznay, L. S. G., Kibens, V., Blackwelder, R. (1970). Large scale motion in the intermittent region of a turbulent boundary layer. *J. Fluid Mech.*, 41:283-325.

List, J., Byerley, A., McLaughlin, T. and Van Dyken, R. (2003). Using a plasma actuator to control laminar separation on a linear cascade turbine blade. 41st AIAA Aerospace Sciences Meeting and Exhibit, *AIAA J.*, Paper No. 2003-1026.

Liu, Z.C., Adrian, R. J. and Hanratty, T. J. (1991). High resolution measurement of turbulent structure in a channel with particle image velocimetry. *Exp. Fluids*, 10:301.

Lundell, F. (2007). Reactive control of transition induced by free-stream turbulence: an experimental demonstration, *J. Fluid Mech.*, 585:41–71.

Lundell, F. & Alfredsson, P. H. (2003). Experiments on control of streamwise streaks. *Eur. J. Mech. B/Fluids*, 22:279-290.

Marusic, I. (2001). On the role of large-scale structures in wall turbulence. *Phys. Fluids*, 13:735.

Marusic, I., McKeon, B. J., Monkewitz, P. A., Nagib, H. M., Smits, A. J. and Sreenivasan, K. R. (2010). Wall-bounded turbulent flows: recent advances and key issues. *Phys. Fluids*., 22:065103.

McLaughlin, T. E., Munska, M. D., Vaeth, J. P., Dauwalter, T. E., Goode, J. R. and Siegal, S. G. (2004). Plasma-based actuators for cylinder wake vortex control. Second AIAA Flow Control Conference, *AIAA J.*, Paper No. 2004-2129.

Meinhart, C. D. and Adrian, R. J. (1995). On the existence of uniform momentum zones in a turbulent boundary layer. *Phys. Fluids*, 7:694.

Meinhart C. D., Wereley S. T., Santiago J. G. (2000). A PIV Algorithm for Estimating Time-Averaged Velocity Fields, *J. Fluids Eng.*, Vol. 122, 285-289.

Melling A. (1997). Tracer particles and seeding for particle image velocimetry. Meas. Sci. Technol., 8:1406-1416.

Moreau, E. (2007). Airflow control by non-thermal plasma actuators. *J. Phys. D: Appl. Phys.*, 40:605–636.

Murlis, J., Tsai, H.M. and Bradshaw, P. (1982). The structure of turbulent boundary layers at low Reynolds numbers. *Journal of Fluid Mechanics*, 122:13–56.

Myose R.Y. and Blackwelder R.F. (1995). Control of streamwise vortices using selective suction, *AIAA J.*, 33:1076.

Offen, G. R., Kline, S. J. (1975). A proposed model of the bursting process in turbulent boundary layers. *J. Fluid Mech.*, 70:209-28.

Opaits, D., Zaidi, S., Schneider, M., Miles, R., Likhanskii, A., Macheret, S. (2009). Improving thrust by suppressing charge build-up in pulsed DBD plasma actuators. 47th AIAA Aerosp. Sci. Meet. (Orlando, USA, 2009), *AIAA J.*, Paper No. 2009-487.

Orlov, D. M. (2006). *Modelling and simulation of single dielectric barrier discharge plasma actuators*. PhD thesis, Univ. Notre Dame.

Orlov, D., Corke, T., Patel, M. (2006). Electric circuit model for aerodynamic plasma actuator. AIAA 44th Aerospace Sciences Meeting (Reno, Nevada, January 2006), *AIAA J.*, Paper No. 2006-1206.

Panton, R. L. (2001). Overview of the Self-Sustaining Mechanisms of Wall Turbulence. *Progress in Aerospace Sciences*, 37:341-383.

Pons, J., Moreau, E., Touchard, G. (2005). Asymmetric surface dielectric barrier discharge in air at atmospheric pressure: electrical properties and induced airflow characteristics. *J. Phys. D: Appl. Phys.*, 38:3635-3642.

Pope, S.B. (2009). *Turbulent flows*. Cambridge university press.

Porter, C., McLaughlin, T., Enloe, L., Font, G. (2007). Boundary layer control using DBD plasma actuator. Presented at AIAA Aerosp. Sci. Meet. Exhibit, 45th, Reno, *AIAA J.*, Pap. No. 2007-0786.

Post, M. L. & Corke, T. C. (2003). Separation control on high angle of attack aerofoil using plasma actuator. *AIAA J.*, paper 2003-1024.

Post, M. L. & Corke, T. C. (2004a). Separation control on high angle of attack aerofoil using plasma actuators. *AIAA J.*, 42:2177–2184.

Post, M. L. & Corke, T. C. (2004b). Separation control using plasma actuators-stationary and oscillatory aerofoils. *AIAA J.*, Paper No. 2004-0841.

Post, M. L. & Corke, T. C. (2004c). Separation control using plasma actuators – dynamic stall control on an oscillating airfoil. *AIAA J.*, Paper No. 2004-2517.

Prandtl, L. (1904). Über Flüssigkeitsbewegung bei sehr kleiner Reibung. *Verhandlungen des dritten internationalen MathematikerKongresses, Heidelberg, August 1904*:484-491.

Purtell, L.P., Klebanoff, P.S. & Buckley, F.T. (1981). Turbulent boundary layer at low Reynolds number. *Physics of Fluids*, 24:802–811.

Raffel, M., Willert, C. E.,Werely, S. T. & Kompenhans, J. (2007). *Particle Image Velocimetry: A Practical Guide*, second ed., Springer-Verlag Heidelberg Berlin.

Ramakumar, K. (2006). *Active flow control of low pressure turbine blade separation using plasma actuators*. MSc thesis, University of Kentucky.

Rathnasingham, R. & Breuer, K. S. (2003). Active control of turbulent boundary layers. *J. Fluid Mech.*, 495:209:233.

Rivir, R. (2007). Effects of pulsed dc discharge plasma actuators in a separated LPT boundary layer. *AIAA J.*, paper 2007-0942.

Rizzetta, D. & Visbal, M. (2007). Numerical investigation of plasma-based flow control for a transitional highly-loaded low-pressure turbine. *AIAA J.*, paper 2007-0938.

Robinson, M. (1961). Movement of air in the electric wind of corona discharge. *AIAA Trans*, 80:143.

Robinson, S. K. (1991a). Coherent motions in the turbulent boundary layer. *Annu. Rev. Fluid Mech.*, 23:601.

Robinson, S. K., (1991b). Kinematics of Turbulent Boundary Layer Structure. *NASA TM 103859*.

Roth, J. R. and Dai, X. (2006). Optimization of the aerodynamic plasma actuator as an EHD electrical device. AIAA Meeting (Reno, USA, January 2006), Paper No. 2006-1203.

Roth, J. R., Sherman, D. M., and Wilkinson, S. P. (1998). Boundary layer flow control with a one atmosphere uniform glow discharge surface plasma. *AIAA J.*, Paper No. 1998-0328.

Roth J. R., Sherman D. M., Wilkinson S.P. (2000). Electrohydrodynamic flow control with a glow-discharge surface plasma. *AIAA J.*, 38:1166-1172.

Santhanakrishnan, A. and Jacob, J. D. (2007). Flow control with plasma synthetic jet. *Journal of Physics D: Applied physics*, 40:637-651.

Santhanakrishnan, A. and Jacob, J. D. (2007). Formation and scaling of plasma synthetic jet actuators. *45th AIAA Aerospace Sciences Meeting and Exhibit*, Paper No. 2007-0940.

Santhanakrishnan, A., Reasor, D. A. and LeBeau, R. P. (2009). Characterization of linear plasma synthetic jet actuators in an initially quiescent medium. *Phys. Fluids*, 21:043602.

Scarano F. (2007). *Experimental Aerodynamics*, Delft University of Technology.

Schlatter & Örlü, (2010). Assessment of direct numerical simulation data of turbulent boundary layers, *J. Fluid Mech.*, 659:116-126.

Schlichting, H. (1979). Boundary-Layer Theory. McGraw-Hill, New York, 7th ed. edition.

Schoppa, W., Hussain, F. (2000). Coherent structure dynamics in near-wall turbulence. *Fluid Dyn. Res.*, 26:119–139.

Sherman, D. M. (1998). *Manipulating aerodynamic boundary layers using an electrohydrodynamic effect generated by one atmosphere uniform glow discharge plasma*. Master of Science Thesis, University of Tennessee.

Simens, M. P., Jiménez, J., Hoyas, S. and Mizuno, Y. (2009). A high-resolution code for turbulent boundary layers. *J. Comput. Phys.*, 228:4218-4231.

Sirovich L. (1987). Turbulence and the dynamics of coherent structures, Part I: coherent structures. *Q. Appl. Math*., 45(3):561-571.

Smith, C. R., Metzler, S. P. (1983). The characteristics of low-speed streaks in the near-wall region of a turbulent boundary layer. *J. Fluid Mech.* 129:27-54.

Smith, C. R., Patterson, G. K. and Zakin, J. L. (1984). A synthesized model of the near-wall behavior in turbulent boundary layers. *The 8th Symposium on Turbulence, Rolla*.

Smits, A.J. and McKeon, B.J. and Marusic, I. (2011). High-Reynolds number wall turbulence. *Annual Review of Fluid Mechanics*, 43:353-375.

Sosa, R. and Artana, G. (2006). Steady control of laminar separation over airfoils with plasma sheet actuators. J. Electrost., 64: 604-10.

Spalart, P.R. (1988). Direct simulation of a turbulent boundary layer up to Reθ = 1410. *Journal of Fluid Mechanics*, 187:61–98.

Stanislas, M., Perret, L. and Foucaut, J.M. (2008). Vortical Structures in the Turbulent Boundary Layer: A Possible Route to a Universal Representation. *Journal of Fluid Mechanics*, 602:327-382.

Stephen E., Campbell A., Nygard J., Selby J., Hennig C. and McLaughlin T. (2011). Assessment of a Corner Plasma Actuator for Flow Control Using Periodic Jets, *29th AIAA Applied Aerodynamics Conference (27-30 June 2011, Honolulu, Hawaii)*, AIAA Paper No. 2011-3513.

Suzen Y. B. and Huang P. G. (2006). Simulations of flow separation control using plasma actuators, *44th AIAA Aerospace Sciences Meeting and Exhibit (9-12 January 2006, Reno, Nevada)*, AIAA Paper No. 2006-877.

Suzen, Y. B., Huang, P. G. & Ashpis, J. D. (2007). Numerical simulations of flow separation control in low-pressure turbines using plasma actuators. *AIAA paper 2007-0937*.

Theodorsen, T. (1952). Mechanism of turbulence. *Proceedings of the Second Mid-western Conference on Fluid Mechanics (Ohio State University, Columbus, OH, 1952)* ,1–18.

Theodorsen, T. (1955). The structure of turbulence. *50 Jahre Grenzschichtforsung*, ed. H. Görtier, W. Tollmein, pp. 55.

Thomas, F. O., Kozlov, A. and Corke, T. C. (2005). Plasma actuators for landing gear noise reduction. *11th AIAA/CEAS Aeroacoustics Conference*, Paper No. 2005-3010.

Townsend, A.A. (1956). *The Structure of Turbulent Shear Flow*. Cambridge University Press.

Von Kármán, T. (1930). Mechanische Ähnlichkeit und Turbulenz. *Nachrichten Ges. Wiss. Goettingen, Math. Phys. Klasse*, 58-76.

Wallace, J. M., Eckelmann, H. and Brodkey, R. S. (1972). The Wall Region in Turbulent Shear Flow, *J. Fluid Mech.*, 54, No. 1, pp. 39-48.

Westerweel J. (1997). Fundamentals of digital particle image velocimetry, *Measurement Science and Technology*, 8:1379-1392.

White, F. M. (2006). *Viscous fluid flow*. McGraw-Hill, New York, third edition.

Willert C. and Gharib M. (1991). Digital particle image velocimetry. *Exp. Fluids*, 10:181-193.

Willmarth, W. W., Lu, S. S. (1972). Structure of the Reynolds stress near the wall. *J. Fluid Mech.*, 55:65-69.

Wu, X. and Moin, P. (2009). Direct numerical simulation of turbulence in a nominally zero-pressure-gradient flat-plate boundary layer. *Journal of Fluid Mechanics*, 630:5-41.

Appendix A: Experimental matrices

Table A.1: Experimental matrix of the 2C-PIV setup for the streamwise spanwise plane

w_{cov}	w_{exp}	V_{pp}	f_{ac}	Waveform	U_∞	f_{acq}	Number of recordings	Recording method	h	Δt	Comments
5 mm	1 mm	-	-	-	7 m/s	25 Hz	2000	double frame	0.3 mm	50 µs	
5 mm	1 mm	6, 8, 10, 12, 14 kV	500 Hz	sine	7 m/s	25 Hz	2000	double frame	0.3 mm	50 µs	
5 mm	1 mm	10 kV	250, 750, 1000 Hz	sine	7 m/s	25 Hz	2000	double frame	0.3 mm	50 µs	
5 mm	1 mm	10 kV	500 Hz	sine	9 m/s	25 Hz	2000	double frame	0.3 mm	39 µs	
5 mm	1 mm	10 kV	500 Hz	sine	11 m/s	25 Hz	2000	double frame	0.3 mm	32 µs	
5 mm	1 mm	10 kV	500 Hz	sine	13 m/s	25 Hz	2000	double frame	0.3 mm	30 µs	
5 mm	1 mm	-	-	-	7 m/s	6000 Hz	5907	double frame	0.3 mm	50 µs	
5 mm	1 mm	8, 10 kV	500 Hz	sine	7 m/s	6000 Hz	5907	double frame	0.3 mm	50 µs	
3 mm	1 mm	8, 10 kV	500 Hz	sine	7 m/s	25 Hz	2000	double frame	0.3 mm	50 µs	
7 mm	1 mm	8, 10 kV	500 Hz	sine	7 m/s	25 Hz	2000	double frame	0.3 mm	50 µs	
-	-	-	-	-	7 m/s	25 Hz	2000	double frame	0.3 mm	50 µs	without act.
-	-	-	-	-	7 m/s	6000 Hz	5907	double frame	0.3 mm	50 µs	without act.
5 mm	1 mm	10 kV	500 Hz	sine	7 m/s	25 Hz	2000	double frame	0.5 mm	50 µs	start of act.
5 mm	1 mm	10 kV	500 Hz	sine	7 m/s	6000 Hz	5907	double frame	0.5 mm	50 µs	start of act.
5 mm	1 mm	10 kV	500 Hz	sine	7 m/s	25 Hz	2000	double frame	0.5 mm	50 µs	end of act.
5 mm	1 mm	10 kV	500 Hz	sine	7 m/s	25 Hz	2000	double frame	0.5 mm	50 µs	downstream of act.

Table A.2: Experimental matrix of the 2C-PIV setup for the streamwise wall-normal plane at the middle of the covered and exposed electrode

w_{cov}	w_{exp}	V_{pp}	f_{ac}	Waveform	U_∞	f_{acq}	Number of recordings	Recording method	Δt	Comments
5 mm	1 mm	-	-	-	7 m/s	25 Hz	2500	double frame	40 µs	at covered electrode
5 mm	1 mm	8, 10 kV	500 Hz	sine	7 m/s	25 Hz	2500	double frame	40 µs	at covered electrode
5 mm	1 mm	-	-	-	7 m/s	6000 Hz	6000	double frame	40 µs	at covered electrode
5 mm	1 mm	8, 10 kV	500 Hz	sine	7 m/s	6000 Hz	6000	double frame	40 µs	at covered electrode
5 mm	1 mm	-	-	-	7 m/s	25 Hz	2500	double frame	40 µs	at exposed electrode
5 mm	1 mm	8, 10 kV	500 Hz	sine	7 m/s	25 Hz	2500	double frame	40 µs	at exposed electrode
5 mm	1 mm	-	-	-	7 m/s	6000 Hz	6000	double frame	40 µs	at exposed electrode
5 mm	1 mm	8, 10 kV	500 Hz	sine	7 m/s	6000 Hz	6000	double frame	40 µs	at exposed electrode

Table A.3: Experimental matrix of the 2C-PIV setup for the spanwise wall-normal plane

w_{cov}	w_{exp}	V_{pp}	f_{ac}	Waveform	U_∞	f_{acq}	Number of recordings	Recording method	Δt	Comments
5 mm	1 mm	8, 10, 12 kV	500 Hz	sine	-	4000 Hz	4000	single frame	-	
5 mm	1 mm	14 kV	500 Hz	sine	-	4000 Hz	3504	single frame	-	
5 mm	1 mm	10 kV	1000 Hz	sine	-	5400 Hz	3505	single frame	-	
5 mm	1 mm	10, 12 kV	500 Hz	sine	7 m/s	25 Hz	1000	double frame	120 µs	
5 mm	1 mm	-	-	-	7 m/s	25 Hz	1000	double frame	120 µs	

Appendix B: Results of the POD analysis

Another method to decide on the effectiveness of certain values of actuation parameters in controlling low- and high-speed streaks is proper orthogonal decomposition (POD), which has been discussed in section 4.2.1. The results of the POD analysis for the streamwise velocity component for varying peak-to-peak voltage, actuation frequency, free-stream velocity and exposed electrode width with 1000 snapshots are presented in, respectively, the Tables B.1-B.4.

Note only the energy contributions of the first four modes are displayed, since these modes are the most converged. The energy contribution of the first, second, third and fourth mode increases with the voltage, until a maximum is attained at 8 kV. Further increase in voltage yields a decrease for these modes. However, the 14 kV run jumps out, it shows the largest energy contributions, suggesting not all the relative high energy modes have been captured in that run.

Table B.1: Results of POD analysis for streamwise velocity component with plasma actuation at varying peak-to-peak voltage and 500 Hz.

Actuation voltage	Energy contribution				Contribution of modes 1 to 4
	1st mode	2nd mode	3rd mode	4th mode	
-	5,60%	4,77%	4,69%	4,39%	19,45%
6 kV	6,70%	5,94%	4,92%	3,41%	20,97%
8 kV	7,91%	7,04%	6,74%	4,59%	26,29%
10 kV	7,66%	6,53%	5,55%	3,06%	22,80%
12 kV	6,78%	6,05%	3,76%	3,10%	19,69%
14 kV	8,99%	7,46%	5,64%	4,78%	26,88%

For an increase in frequency from 250 to 500, 750 and 1000 Hz, the energy contribution of the first two modes display a continuous increase. Similar behavior can also be observed for the combined contribution of the first four modes. Although it should be noted the differences between 750 and 1000 Hz are relatively small, indicating the frequency is close to the maximum attainable induced streamwise velocity, which corresponds with the observations of the streamwise velocity plot in Figure 7.11(b).

Table B.2: Results of POD analysis for streamwise velocity component with plasma actuation at varying actuation frequency and 10 kV.

Actuation frequency	Energy contribution				Contribution of modes 1 to 4
	1st mode	2nd mode	3rd mode	4th mode	
250 Hz	6,07%	5,24%	4,80%	4,54%	20,65%
500 Hz	7,66%	6,53%	5,55%	3,06%	22,80%
750 Hz	8,77%	7,52%	5,82%	4,01%	26,13%
1000 Hz	8,78%	8,47%	5,47%	4,23%	26,95%

From Figure 7.11(d) it was noticed the control of the streaks improved, when increasing the free-stream velocity to 9 and 11 m/s. In addition, the Table B.3 shows the overall relative energy contribution of the first four modes reduces for larger free-stream velocities, despite the more extreme velocities at the streaks. Although the decreases from 7 to 9 and 9 to 11 m/s are relatively small, especially when compared to the 5% reduction from 11 to 13 m/s. The relative increases in the energy levels of the boundary layer, due to the increase in free-stream velocity, are apparently larger than the more extreme velocity peaks at the streaks.

Table B.3: Results of POD analysis for streamwise velocity component with plasma actuation at 10 kV peak-to-peak voltage and 500 Hz for at varying free-stream velocity.

Free-stream velocity	Energy contribution				Contribution of modes 1 to 4
	1st mode	2nd mode	3rd mode	4th mode	
7 m/s	7,66%	6,53%	5,55%	3,06%	22,80%
9 m/s	7,27%	6,04%	4,72%	3,03%	21,06%
11 m/s	6,64%	5,77%	3,87%	2,54%	18,82%
13 m/s	4,19%	4,06%	3,15%	2,19%	13,59%

As observed in Figure 7.11(c), the induced streamwise velocities become larger for wider embedded electrodes. Table B.4 shows the improvement is only apparent in the first two modes, these modes display significantly higher energy levels for wider covered electrodes.

Table B.4: Results of POD analysis for streamwise velocity component with plasma actuation at 10 kV peak-to-peak voltage and 500 Hz for varying exposed electrode width.

Covered electrode width	Energy contribution				Contribution of modes 1 to 4
	1st mode	2nd mode	3rd mode	4th mode	
3 mm	4,40%	4,38%	3,21%	2,61%	14,60%
5 mm	7,66%	6,53%	5,55%	3,06%	22,80%
7 mm	9,29%	7,60%	3,62%	3,08%	23,59%

The overall energy contributions of the modes 1 to 4 for all runs reveal the same behavior as is already clear from the first and second mode.